

BACHELOR'S DEGREE IN AEROSPACE TECHNOLOGY ENGINEERING
THE SCHOOL OF INDUSTRIAL, AEROSPACE AND AUDIOVISUAL ENGINEERING OF TERRASSA



UNIVERSITAT POLITÈCNICA DE CATALUNYA
BARCELONATECH

Escola Superior d'Enginyeries Industrial,
Aeroespacial i Audiovisual de Terrassa

Space Engineering project

Preliminary design of a satellite: EXOHALO L2

Authors:

Juan Garrido Moreno
Yi Qiang Ji Zhang
Alexis Leon Delgado
Iván Sermanoukian Molina
Santiago Villarroya Calavia

Professor:

Dr. Adrià Rovira Garcia

Contents

1 Mission Design	1
1.1 State of the art	1
1.1.1 Kepler/K2	1
1.1.2 Gaia	1
1.1.3 Tess	2
1.1.4 Cheops	3
1.1.5 James Webb Space Telescope	3
1.1.6 Plato	4
1.1.7 Ariel	5
1.1.8 Methodology	6
1.2 EXOHALO L2 mission comparison	7
1.3 Objectives: Mission Statement	8
1.4 Funding, Cost, Schedule	8
1.4.1 Launch scenario	10
1.5 Political/International constraints, collaborations	10
1.6 System Requirements	10
1.7 Ground and User agreements	11
1.7.1 International cooperation	11
1.8 Mission architectures	11
1.9 System Requirement Document	13
2 Space environment	14
2.1 Plasma environment	14
2.1.1 Magnetotail considerations	14
2.1.2 Plasma energetic analysis and consequences	15
2.1.3 Protection mechanisms	16
2.2 High-energy radiation environment	17
2.2.1 Origins and consequences	17
2.2.2 Radiation description	17
2.2.3 Protection mechanisms	18
2.3 Meteoroid environment	19
3 Orbital Mechanics	20
3.1 Lagrange points destination analysis	20
3.2 Orbital Transfers	26
3.2.1 LEO parking orbit	26
3.2.2 Sun-Earth System L2 Hohmann transfer	27
3.3 Justification of the chosen orbit in relation to the mission objective(s)	32
3.3.1 Lagrange L2 point	32
3.3.2 L2 Halo orbit	32
4 Launch Considerations	37
4.1 Launcher selection	37
4.1.1 Performance	37

4.1.2 Availability	38
4.1.3 Payload adapter compatibility	38
4.1.4 Costs	38
4.1.5 Reliability	38
4.1.6 Final selection	38
4.2 Launch dynamics: Ascent profile	40
4.2.1 Environment	44
4.2.2 Payload protection	46
4.2.3 Payload emplacement	47
4.3 Propulsion justification	49
4.3.1 Launcher's propulsion system	49
4.3.2 Justification	49
5 Spacecraft definition	51
5.1 Payload selection and adequacy to the mission objective	51
5.1.1 Optical telescope assembly (OTA)	51
5.1.2 Focal plane module (FPM)	53
5.1.3 Data processing subsystem (DPS)	54
5.2 Thermal subsystem	54
5.2.1 Telescope optical unit	54
5.2.2 Solar shield	56
5.2.3 V-grooves	56
5.3 Power subsystem	57
5.3.1 Power consumption budget	57
5.3.2 Power modes	57
5.3.3 Solar cell technology	57
5.3.4 Solar array sizing	59
5.3.5 Batteries	60
5.4 Attitude Determination and Control subsystem	61
5.4.1 Transfer phase propulsion system control	63
5.4.2 Observation phase propulsion system control	63
5.4.3 Star sensors	64
5.4.4 Reaction wheels	66
5.4.5 Cold gas thrusters	67
5.4.6 Sun sensors	68
5.5 Communication subsystem	69
5.5.1 Antennas	70
5.5.2 Amplifiers	70
5.5.3 Transponders	71
5.5.4 Ground segment	72
5.6 General layout	72
6 Conclusions	75
Appendices	81
Appendix 1: Soyuz ascent code	81

Phase 1	81
Phase 2	89
Auxiliary codes	93
Appendix 2: Orbital Mechanics code	97
Main program	97
Hohmann Transfer performance function	99
Fuel mass computation function	99
Appendix 3: Lagrange points	101

List of Figures

1	Kepler satellite. Source: NASA [4]	1
2	Gaia satellite. Source: NASA [9]	2
3	Tess satellite. Source: NASA [12]	2
4	Cheops satellite. Source: ESA [13]	3
5	James Webb satellite. Source: ESA [15]	4
6	Plato satellite diagram. Source: ESA [18]	4
7	Ariel satellite diagram. Source: ESA [20]	5
8	Exoplanet Mission Timeline. Source: ESA [2]	5
9	Mission phases. Procedure from [26]	9
10	Objectives and requirements of the spacecraft mission (architecture option 1)	13
11	Magnetotail and halo orbit interference.	14
12	Magnetotail and bow shock orientations. Source: [32]	15
13	Fluence for a 125000 km amplitude halo orbit assuming solar weather from 1992. Source: [32]	15
14	Electron/proton mean penetration energy ranges in aluminum. Source: [34]	16
15	Ion spectra for 10 years at L2 for solar and galactic sources. Source: [32]	18
16	Dose vs. depth in aluminum for solar protons and galactic cosmic rays. Source: [32]	18
17	Magnetotail and halo orbit interference.	19
18	Visual representation of Lagrange points (not drawn in scale). Source: [39].	20
19	Three body problem rotating reference frame. Source: Own.	22
20	Three body problem reference frame (adimensional). Source: Own.	23
21	Representation of gravitational equipotential surfaces of Sun-Earth system and Lagrange points in a rotating system coordinates. Source: Own.	24
22	3D Representation of gravitational equipotential energy of Sun-Earth system. Source: Own.	25
23	LEO parking orbit scheme. Source: Own.	27
24	Earth-L2 Hohmann transfer scheme. Source: Own.	27
25	HT impulse variation with the height of the parking orbit	28
26	Transfer time variation with the height of the parking orbit	29
27	Mass ratio variation with the height of the parking orbit	29
28	Spacecraft arrival at L2 region. Source: Own.	30
29	Transfer budget variation with the fuel loaded	31
30	Geometry of L2 halo orbit. Source: [45]	33
31	3 plane motion referred to a Lissajous orbit. Source: [47]	34
32	3D representation of a Lissajous orbit. Source: [48]	34
33	ISEE 3 halo orbit motion round Sun-Earth L1. Source: [47]	35
34	3D representation of the Herschel mission halo orbit. Source: [50]	36
35	2D plot of the in-plane motion for the expected Plato's halo orbit. Source: [17]	36
36	Soyuz launch vehicle. Source:[51]	39
37	Altitude evolution vs time.	41
38	Velocity evolution vs time.	41
39	Dynamic pressure evolution during first stage launch phase.	42
40	Forces evolution during first stage launch phase.	42
41	Altitude evolution during the all burning stages process. Source: [51]	43
42	Velocity evolution during the all burning stages process. Source: [51]	43

43	Longitudinal static acceleration evolution. Source: [51]	44
44	Random Vibrations acceptable levels during first stage of flight. Source: [57]	45
45	Acoustic noise spectrum under the Fairing. Source: [57]	46
46	Soyuz total usable volume under the fairing.	47
47	All possible payload configurations inside the Soyuz Spacecraft. Source: [57]	48
48	Soyuz ASAP-S vehicle adapter total configuration	48
49	Fregat upper stage scheme.	49
50	Illustration of the four TESS cameras, lens hoods, and mounting platform. Source: [38]	51
51	Cross-section showing the optical paths for light at a range of incident angles.	52
52	Cross-section of the cameras including the hood. Source: [59]	52
53	Measured quantum efficiency at -70°C for CCD270. Source: [63]	53
54	FPM, DPS and SVM block diagram.	54
55	Illustrations of the copper straps connection and layout.	55
56	The predicted thermal profile of a TESS camera under flight conditions. Source: [59]	55
57	The Planck optical system, including the telescope baffle and V-grooves. Source: [70]	56
58	Illustrations of the copper straps connection and layout.	58
59	Illustrations of the copper straps connection and layout.	59
60	Battery illustrations.	61
61	Architecture of the Attitude Determination and Control Subsystem (ACDS) and the Reaction Control Subsystem (RCS). Source: [58].	62
62	Results of the pointing stability analysis. Source: [58].	64
63	The Galileo Avionica star tracker used on Herschel and many other ESA missions and its principal characteristics). Source: [71].	64
64	The Startracker and telescope. The Startrackers are shown as simple square black boxes with conical baffles in this schematic representation (from Herschel). Source: [71].	65
65	A schematic diagram of EXOHALO L2 avionics. Source: [71].	65
66	Cutaway diagram of the Hubble Space Telescope. Source: [84]	66
67	RDR 68 Reaction wheels from Collins Aerospace. Source: [85]	67
68	Cold Gas thruster representations	67
69	CESS Sun Sensor from Spacetech. Source: [89]	68
70	CESS working principle and specifications. Source: [89]	69
71	Satellite frequency nomenclature. Source: [91].	69
72	Voyager High Gain Antenna. Source: [93].	70
73	Deep Space Network Antenna. Source: [93].	71
74	Ground station mission operation segment.	72
75	Herschel's general layout illustrations. Source: [71]	73
76	Planck's general layout illustration. Source: [70]	73
77	ARIEL's general layout illustrations. Source: [19]	73

List of Tables

1	Architecture alternatives	12
2	Meteor streams known to produce enhanced or storm level activity. Source: [32]	19
3	Lagrange point locations	25
4	Orbital transfers alternatives.	26
5	Hohmann transfer performance.	30
6	Hohmann transfer orbit geometric data.	30
7	Selection criteria for each launch vehicle. Source: data retrieved from [17][51][30][52][53][54][55]	37
8	Sinusoidal limit vibrations for Soyuz auxiliary passengers. Source: [57]	45
9	Pre-flight required safety factors	47
10	Soyuz 2-1b Fregat propulsion performance. Source: data retrieved from [51]	49
11	Specifications for the e2v CCD270. Source: [63] and [64]	53
12	Payload power budget.	57
13	Subsystems power budget.	57
14	Average efficiencies for different possible conditions along its operational life. Source: [75]	58
15	Battery reference data. Source: [79] and [80]	60

Abstract

EXOHALO L2 is the S3 (small-size) mission within the Cosmic Vision 2015-2025 ESA programme with a TBD (to be decided) launch date starting at 2026. EXOHALO L2 will carry out exoplanet exploration so as to increase the data with which it will be possible to recreate the visible Universe in conjunction with past and future missions by enhancing previous observations and acquiring raw data which will need to be processed. The satellite will follow a halo orbit around the Sun-Earth Lagrangian point L2 in order to get the best visual capabilities for exoplanets exploration. The EXOHALO L2 payload consists of 4 ($25^\circ \times 25^\circ$) field of view cameras that will allow us to perform the remote sensing process at different wavelengths, mainly in the IR spectrum. The nominal duration of the science operations is 3 years.

1 Mission Design

1.1 State of the art

The primary field of study of the mission are exoplanets, i.e. the planets which are outside the Solar System. The first confirmation of detection occurred in 1992, and more than 4000 exoplanets have been discovered up to date [1]. However, thousands of other candidates have been detected and require further observations to confirm their identity.

According to both NASA and ESA mission timelines [2], the functioning satellites during the last decade which were aimed partially or completely to the discovery of exoplanets have been:

1.1.1 Kepler/K2

NASA's Kepler Space Telescope [3] made history with its discovery of thousands of exoplanets through the use of Transit techniques which will be analysed in the methodology subsection 1.1.8. In its first mission, from 2009 to 2013, Kepler monitored more than 150.000 stars until technical problems caused the spacecraft to lose its pointing ability almost completely. However, in 2014, the second mission began with a new name, K2, and continued the exoplanet discovery in spite of the diminished directional capability.

It was finally decommissioned in 2018 after having discovered more than 2600 exoplanets, more than any mission so far. The data obtained is still being analysed by researchers who have found new exoplanets in recent years such as an Earth-Size, habitable zone planet which is located 300 light-years from Earth.

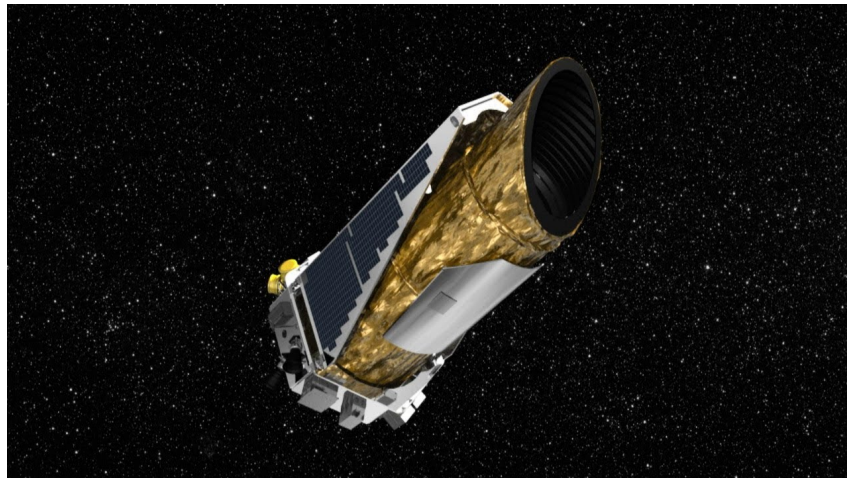


Figure 1: Kepler satellite. Source: NASA [4]

1.1.2 Gaia

Gaia (mother Earth in Greek mythology) is an ESA primordial astrometric mission [5], part of the Horizon 2000 scientific program, with the goal to accomplish a 3D space catalog compilation of more than a thousand million stars, which account to roughly 1% of the stars in our home galaxy, the Milky Way.

Gaia is orbiting the Sun-Earth system from the second Lagrange point L2 [6]. Although the mission was firstly designed to last for a nominal five-year period after its launch on December 2013, it was afterwards extended to the end of 2022 with an indicative subsequent extension until the end of 2025 if the mission subsystems are not excessively damaged and the cost of the mission is deemed appropriate to continue.

According to ESA's last reports [7] from the data already obtained, it is expected that Gaia will have detected tens of thousands of exoplanets out to 500 parsec from the Sun by measuring the wobbling motion that perturbs the star orbit, which is reflected in the position, which does not correctly match a pure stellar motion. An approximation was already carried out in 2014 [8] which considered a plausible assumption where we would find 21.000 ± 6.000 high-mass long-period planets in the 500 parsecs for the

nominal 5-year duration, where between 1000 and 1500 would be dwarf planets out to 100 parsecs. It was also carried out an approximation for a mission duration of 10 years rising to 70.000 ± 20.000 planets.



Figure 2: Gaia satellite. Source: NASA [9]

1.1.3 Tess

TESS, the Transit Exoplanet Survey Satellite, is an MIT-led NASA mission [10] with an initial duration of two years discovering transiting exoplanets by an all-sky survey. It is based on monitoring the brightness of dwarf stars for periodic drops caused by planet transits [11]. It has been functioning after the elapsed two initial years providing a torrent of high-quality observations of 66 new exoplanets as well as 2100 candidates which require further analysis.

The cameras are optimised for the detection of hundreds of Super Earths around nearby, bright stars. They use a red-optical bandpass [10] covering the wavelength range from about 600 to 1000 nm and are able to operate at a temperature around -75°C .

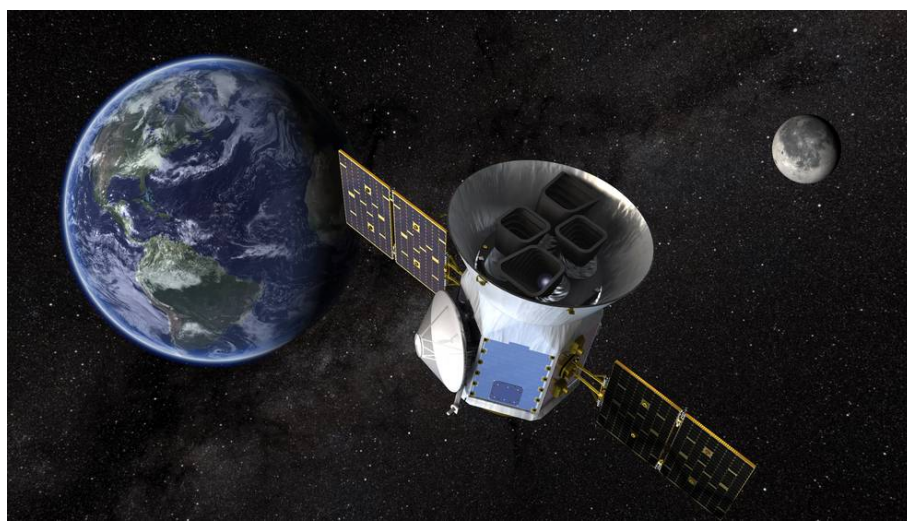


Figure 3: Tess satellite. Source: NASA [12]

1.1.4 Cheops

Cheops is the acronym of ESA's **CH**aracterising **E**x**O****P**lanet **S**atellite [13]. This mission has a completely different goal from the previous cases because it is the first mission dedicated to studying bright, nearby stars which already host known exoplanets, so as to obtain high-precision observations of the planets main characteristics such as the planet's size, being focused on planets in the super-Earth to Neptune size range, as well as the mass, the density and atmosphere composition.

Since its launch on December 2019 to a Sun-synchronous orbit of about 700 km altitude, it has a nominal mission duration of three and a half years which can be expanded depending on the results obtained and the remaining capabilities of the satellite at that time.



Figure 4: Cheops satellite. Source: ESA [13]

By the time EXOHALO L2 is designed and built, both Gaia and Tess will have been decommissioned while Cheops might be on the verge of decommission procedures if a time extension is approved by 2022. Thus, it is crucial to known the projects that are being carried, to obtain the maximum capabilities of the satellite conjunction. As a result, exoplanet survey mission up to 2030 have been taken into consideration:

1.1.5 James Webb Space Telescope

After its 2021 launch, NASA's James Webb Space Telescope will observe planets that are in the habitable zone with a near-infrared study of the atmosphere [14]. It will be based on transit procedures using transmission spectroscopy and has been designed to accomplish 5 years of continuous usage with a goal of 10 years with some minor technical issues.

Webb will also continue the development of direct imaging procedures, a method that is growing over the last few years. This telescope will have the required capabilities to observe planets in the mid-infrared with a sensitivity never reached by previous satellites.

A new technique known as a phase curve will be tested involving the observation of the planets over the course of an entire orbit, which can only wiled practical results for the hottest worlds with the shortest orbital periods.

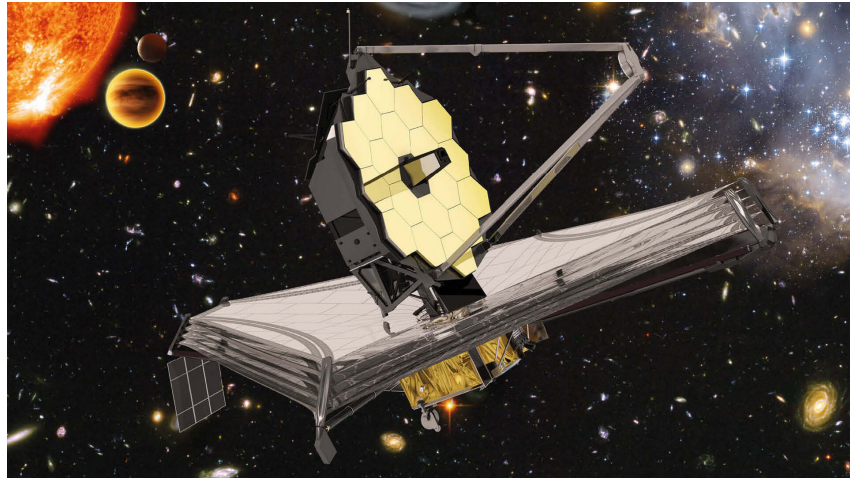


Figure 5: James Webb satellite. Source: ESA [15]

1.1.6 Plato

Plato, the **PLA**netary **T**ransits and **O**scillations of stars mission, will be launched in 2026 to the Lagrange Sun-Earth point L2 to expand on the work of Cheops with a special emphasis on rocky planets around Sun-like stars and their habitable zone, where liquid water could be found [16].

The cameras are based on the visible spectrum and will be using the transit method within long uninterrupted periods with high precision photometric monitoring [17]. This method will be verified by complementary radial velocity data to confirm the detection of each candidate.

What is more, a new method similar to gravitational microlensing will be tested. Asteroseismology, as it has been named, will study the intrinsic oscillations of stars and the variations which cause to the light curves analysed in Fourier spaces.

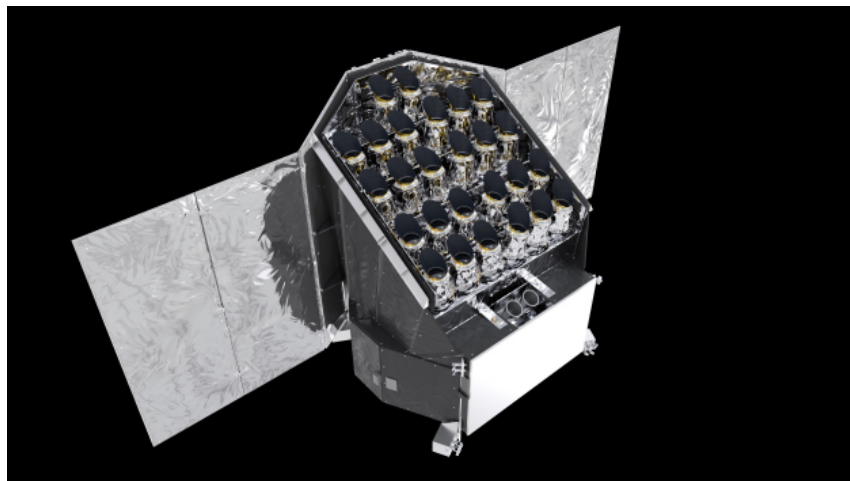


Figure 6: Plato satellite diagram. Source: ESA [18]

1.1.7 Ariel

Ariel, the Atmospheric Remote-sensing Infrared Exoplanet Large-survey mission [19], is the logical next step to both Cheops and Plato. The mission will be focused on relatively warm and hot planets, ranging from super-Earths to gas giants which are orbiting close to their parent stars, taking advantage of their well-mixed atmospheres to decipher their composition by measuring the chemical fingerprints as the planet crosses in front of its host star.

ARIEL's telescope will operate at visible and infrared wavelengths so as to enlarge the capabilities of the system.

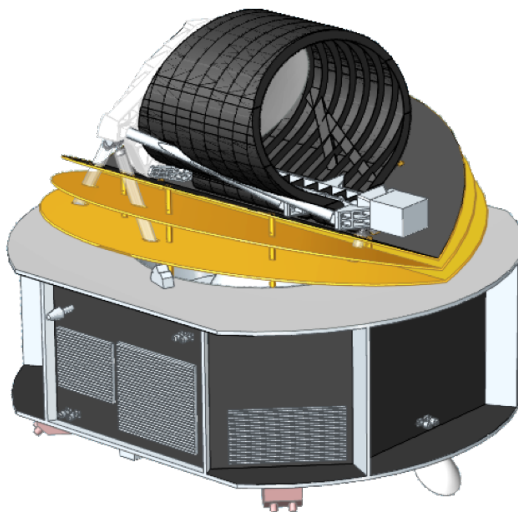


Figure 7: Ariel satellite diagram. Source: ESA [20]

The image below displays the exoplanet mission timeline of past, present and future missions.

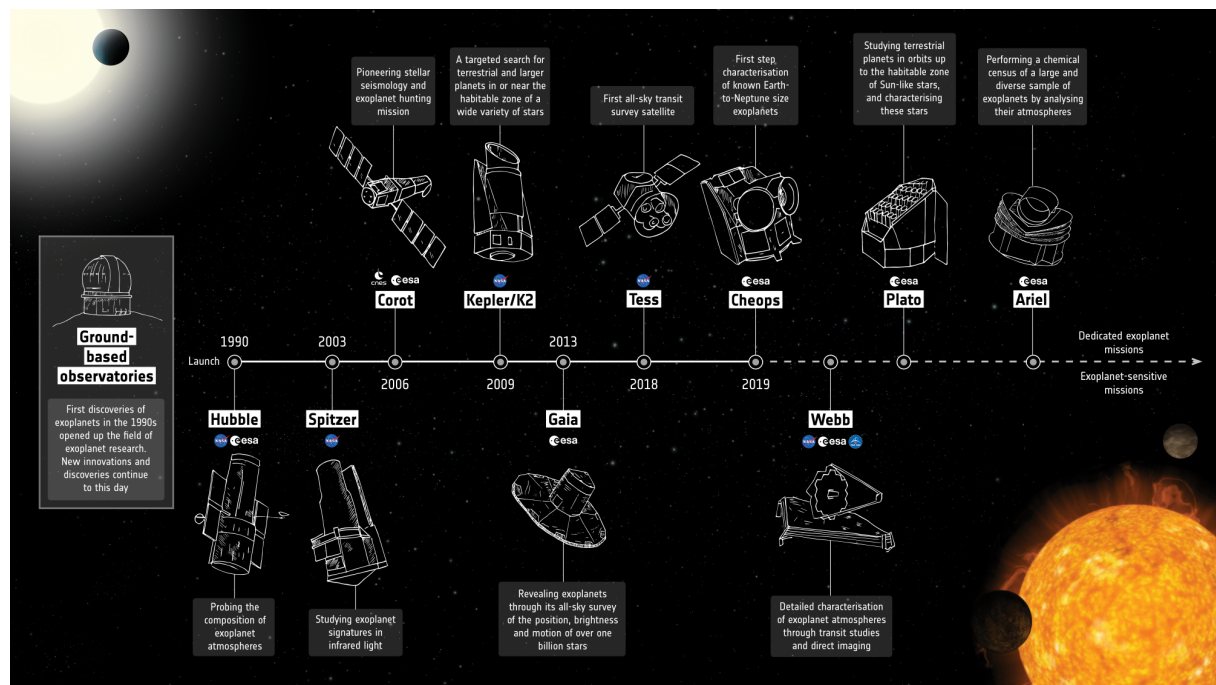


Figure 8: Exoplanet Mission Timeline. Source: ESA [2]

1.1.8 Methodology

In order to detect them, there are 5 ways which have been used in the last three decades [21]:

1. Radial velocity

The effect that planets have on the star they are orbiting due to the gravitational force can be noticed by the resulting wobbling motion of the host star, changing the colour of the light astronomers observe. The method used is called Doppler shift and is based on the changes of wavelength perceived. What is more, this method was one of the first successful ways to find exoplanets and is often relied on to confirm planets found with other methods.

2. Transit

When a planet passes directly between its host star and a distant observer, it dims the star's emitted light by a measurable amount. It usually is a slight variation, but it is enough to clue astronomers into the presence of an exoplanet around the analysed star. Depending on the duration and the amount of light which is blocked, information can be obtained from the transit regarding the exoplanet. Giant planets block more light and, thus, create deeper light curves while the farther a celestial body is, the longer it takes to orbit and pass in front of the star.

When the analysed system has multiple planets, the light curves get complicated. However, it only takes more time from specialists to isolate each planet from the data.

Furthermore, this method can be used to give us information about the composition of a planet's atmosphere, by analysing the colours of the starlight which passes through the atmosphere while the exoplanet passes in front of its star, obtaining evidence about its composition as well as its temperature.

3. Direct imaging

As exoplanets are millions of times dimmer than the stars they orbit, any light reflected off of the celestial body or heat radiation from the planet itself is drowned out by the overwhelming glare coming from its star. The method uses various techniques to block out the light of stars that might have planets orbiting them in order to get a better look at possible exoplanets orbiting the host star.

There are two main methods used to block the light of a star: coronagraphy uses a device inside a telescope to block light from a star before it reaches the telescope detector while using a starshade, a device which blocks light from a star before it even enters a telescope, requires a different spacecraft.

4. Gravitational microlensing

Gravity can bend and focus light like a lens in a magnifying glass. As a result, gravitational microlensing happens when a celestial body gravity focuses the light of another star so that it makes it temporarily seem brighter.

The light levels decrease after the exoplanet is lensed, but then they continue to increase due to the continued lensing action of the star. Then, as the lensing star moves out of the optimum position, the brightness of the more distant star fades away.

As viewed from Earth, a lensing event looks like a distant star that gets gradually brighter over approximately a month and then fades away.

5. Astrometry

The orbit of a planet can cause a star to wobble around in space concerning nearby stars in the sky. This approach is an originally laborious method based on taking a series of images of a star and some of the other stars that are near it in the sky. Then the relative distances between these reference stars are compared in search of exoplanets.

Astrometry requires extremely precise optics because the Earth's atmosphere distorts and bends light.

From all the mentioned techniques, transit photometry and doppler shift methods are the most reliable techniques, having discovered a 96.39 % of the total.

After analysing the effectively vs. cost of each method, direct imaging has been discarded, due to the need of extra equipment, as well as gravitational microlensing due to the post-process complexity.

1.2 EXOHALO L2 mission comparison

EXOHALO L2 design phase would be fast as the Technology Readiness Level (TRL) of most parts is intended to be TRL 6 or superior. Then, it is viable to consider reduced periods of time in relation to the State of the art missions.

According to the launch considerations, EXOHALO L2 satellite would be launched in conjunction with Plato. The expected year is 2026 but it is yet to be decided. Regarding the last ESA budget for 2021 new missions, there has been a top-line reduction of 2.7% from 2020 total values [22], reflecting a sharp drop in contributions from ESA member states. Due to the covid pandemic, the European Commission slashed its space budget for the next seven years, an action that will surely cause delays on current missions and harder entry barriers for new projects.

Considering a 2026 to 2028 launch window, James Webb will have surpassed its nominal stage and will continue with reduced capabilities until 2031. Plato would start some months before EXOHALO L2 in search of rocky planets while Ariel would still require several years until its launch. This is the best opportunity for the mission to start.

As a result, EXOHALO L2 infrared cameras could be used to continue Webb's exploration so as to confirm previous data which might require extra steps. It would perform tasks similar to TESS but with newer equipment capable of reaching higher precision including some planet categories that weren't surveyed.

While Plato would be in search of rocky planets, EXOHALO L2 would be using infrared techniques applied to transit methods to obtain data. The benefit in relation to previous visible light observation is that it is at infrared wavelengths that molecules in the atmospheres of exoplanets have the largest number of spectral features. While visual wavelengths are based on the characterization of planet properties and atmospheres by looking at primary transits when the light passes behind the planet, IF techniques look for the light that passes through the planet atmosphere and imprints absorption features [23].

Finally, it would complement Ariel by obtaining data from the atmospheres outside Ariel observation window.

1.3 Objectives: Mission Statement

The main **objectives** of the mission are listed below:

1. Determine with high precision the bulk properties (mass, radius, mean density) of exoplanets in a wide range of systems and inferring the presence or absence of a significant atmospheric envelope.
2. Analyse exoplanets in the size range of super-Earths and mini-Neptunes located in the habitable zone of solar-like stars.
3. Study the atmospheric composition, i. e. to study the physical and chemical properties of a large and diverse sample of uncovered exoplanets and, through those, understand how planets form and evolve in this galaxy and whether they can harbour carbon based life or not.

Regarding the first objective, current satellites are only capable of reaching radius precision of 10 % with ESA's CHEOPS [24], and will be able to reach 1 – 2 % after PLATO's future launch. Being able to provide planetary data with higher precision would allow us to understand in a better way the composition of the extrasolar universe and catalogue the visible segment.

In terms of the planetary size range, related to the second objective, NASA's TESS only observes exoplanets contained in the Earth and super-Earth categories. Due to this fact, being able to analyse other planets such as mini-Neptunes would be a significant improvement to NASA's current exoplanet survey satellite. This feature would enable to validate 2020 papers [25] which claim that mini-Neptunes would be super-Earth planets orbiting extremely close to their parent stars, so close that the radiation from the stars could be affecting these planets and masquerading them as mini-Neptunes with a low density. This scenario could be explained by a thick layer of water in a supercritical state which experiences an intense greenhouse effect, covering the rocky core.

The third objective aims to analyse the current state of exoplanet atmospheres of deep-space stellar systems and catalogue the different possible stages they might be immersed in, depending on the gases found on the upper atmosphere, while examining their suitability to make life prosper on their surfaces.

1.4 Funding, Cost, Schedule

The major part of the funding will come from ESA's Budget. As a part of Cosmic Vision, the third campaign of space science and space exploration missions, EXOHALO L2 would take part as a small class mission which is intended not to exceed 50 milion euros. A first call for mission proposals was issued in March 2012, when most missions were selected but there is still room for some minor missions.

The following page develops the schedule of the mission:

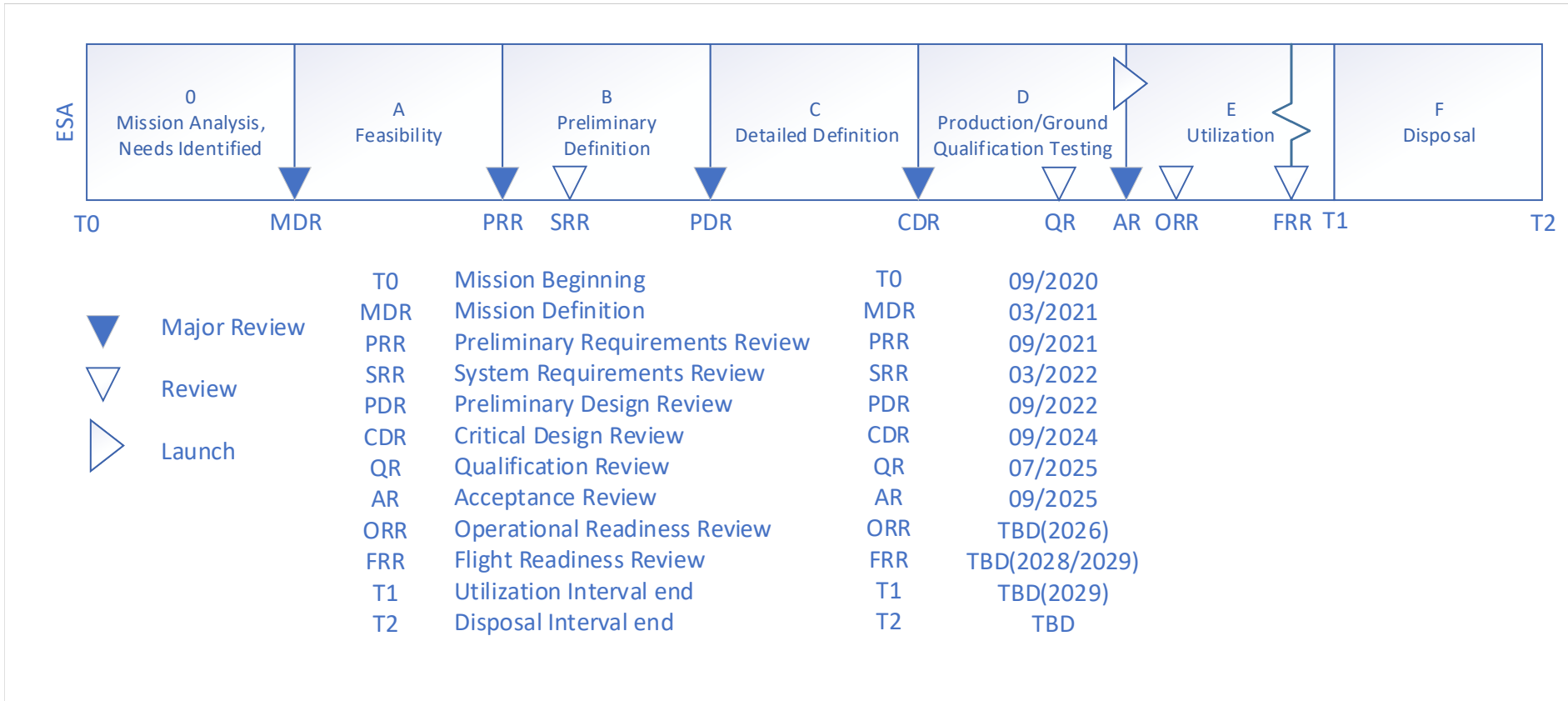


Figure 9: Mission phases. Procedure from [26]

1.4.1 Launch scenario

The first launch window is foreseen with ESA's PLATO, which will be launched in 2026 from Kourou by a Soyuz 2-1b rocket with Fregat upper stage (further explained in §4) and injected onto a transfer trajectory to L2. It would be used the auxiliary passenger position.

1.5 Political/International constraints, collaborations

As the mission would be mainly funded by ESA budget, its development and evolution would be totally subjected to the political and economic situation of the European Union (EU). Hence, the analysis and studies regarding the economic progress of the EU will have a great impact on the economic feasibility of the Exohalo L2 mission.

Different political and economic scenarios can be considered. The optimistic one is considering a great Europe progress, especially for the states that represent the largest part of ESA's budget. This would suppose an increase of the technological ambition perspective leading the space sector, and consequently Exohalo L2 mission, to a faster and more feasible progression. Nevertheless, the realistic scenario, expects much slower progress owing to the difficult situation that the most of the European Union countries are going through. The plans for fighting against COVID-19 pandemic and the exit from the UE of the United Kingdom (Brexit) have monopolized most of all the resources of the European Union states. Therefore, as mentioned in [22], the budget deficits and political problems makes that ESA face with permanent struggles for better budgets and a limited political consensus.

Additionally, as a consequence of being made up of a large number of european countries with different legislations regarding the treatment and study of data obtained by space exploration, the process of converting the reasearch into applications, then into a real service and finally into a globally competitive service is full of bureaucratic obstacles that only delay progress and results.

Regarding the Exohalo L2 international cooperation, in the Ground and User agreements, the possibility of sharing all the information obtained with other space agencies is strongly considered. The objective of international cooperation is not only based on a exchange of relevant data, it is also a very useful tool for the acquisition of new knowledge through a space program with similar requirements and objectives in which Exohalo L2 mission and consequently the European Space Agency will collaborate with the different partners

1.6 System Requirements

The main system requirements are defined in order to set the technical achievements that must be fulfilled by all the mission subsystems in order to achieve the mission main objective. Hence, regarding the different subsystems that are part of the spacecraft, the following requirements are stated.

- The satellite mass shall not be higher than 400 kg.
- The launch system shall deliver an approximated 400 kg satellite to a 1000 km altitude LEO orbit.
- The power subsystem shall provide 220 W in a expected nominal range configurations.
- The interplanetary propulsion system will be able to carry a 400 kg satellite from a 1000 km altitude LEO orbit to a halo orbit around the Lagrange point L2.
- The communication subsystem will provide two-way communications using S-band for command uplink and low-rate telemetry downlink, and Ka-band for high rate telemetry downlink.
- The Attitude Determination and Control Subsystem will maintain the satellite in a stable orbit around L2, and shall provide the coarse pointing of the Observatory to interest Line of Sight of the mission.

1.7 Ground and User agreements

According to Chapter 15 of SMAD [27], the type and number of ground stations must be chosen. In this case, the existing ESA's tracking station network (ESTRACK) [28] will be selected and used as shared ground stations.

In regards to mission, spacecraft and data management, the corresponding control centers must be defined. In order to operate the space mission and interact with ground stations, a mission control centre must be defined, so ESA's Mission Operation Center (MOC) will be used for this purpose. In addition, ESA's Science Operations Centre (SOC) will serve as data housekeeper and science actions commander. Specifically, both Gaia [29] and ARIEL [30] missions used the mentioned centers.

These stations facilitate the communication between ground engineers and scientific probes.

The ESA-owned stations [31] are:

- Cebreros Station (Spain)
- Kiruna Station (Sweden)
- Kourou Station (French Guiana)
- Malargüe Station (Argentina)
- Malinda antenna (Malindi Space Centre (Kenya))
- New Norcia Station (Australia)
- Redu Station (Belgium)
- Santa Maria Island Station (Azores, Portugal)

1.7.1 International cooperation

ESA shares ESTRACK network with other agencies and states who in return provide tracking services under several resource-sharing agreements. These agreements allow access to:

- Agenzia Spaziale Italiana (Italy)
- Centre National d'Etudes Spatiales (France)
- Deutsches Zentrum für Luft- und Raumfahrt (Germany)
- NASA's Deep Space Network (USA)
- NASA's Goddard Space Centre (USA)
- JAXA (Japan)

This cooperation allows more efficiency in terms of geographically advantageous locations for each mission enhancing the results obtained. This is possible through the adoption of internationally recognised technical standards used for sharing tracking data and its post-process methods.

The Ground segment will establish control with the spacecraft at a nominal speed of more than 400 GB per day, 7 days per week during at least 3.5 hours each day.

Regarding the user segment, as the data obtained will be of purely scientific domain, it will already come structured so as to ease the post-process techniques, and will be distributed to ESA's investigation facilities as well as sponsor enterprises which might have partially funded the mission.

1.8 Mission architectures

As stated in Chapter 2 of [27], the mission architecture is defined by a mission concept plus the eight elements specified in Table 1. The first step is to identify the elements that are not subject to trade, that is to say, the aspects in which there is a unique option possible. For the sake of simplicity, in this case the spacecraft bus, comms architecture, ground system and mission operations will be common features for both architectures alternatives.

ARCHITECTURE		OPTION 1	OPTION 2
Mission concept		Exoplanets observation and study	
Elements	Option area		
1. Subject of the mission	Object to measure	IR light	Visible light
2. Payload	Frequency	IR (observation), visible (guidance system)	Visible (observation and guidance system)
	Aperture	4 cameras ($25^\circ \times 25^\circ$ each)	Telescope 0.95 m
3. Spacecraft bus	Propulsion	Cold gas thruster	
	Orbit control	Ground	
	Navigation	Ground-based	
	Attitude determ. and control	3-axis, spacecraft pointing	
	Power	Two solar pointed arrays	
4. Launch system	Launch vehicle	Soyuz (as auxiliary passenger)	Ariane 6-62 (as auxiliary passenger)
	Upper stage	Fregat with ASAP-S config.	UPLM with Single Launch config.
	Launch site	Kourou, French Guiana	
5. Orbit	Special orbits	Lagrange point L2	Sun-synchronous
6. Comms architecture	Timeliness	Real-time	
	Control and data dissemination	Multiple, commercial link (ESA's MOC and SOC)	
7. Ground system	Existing or dedicated	Shared ground tracking system (ESA's ESTRACK)	
8. Mission operations	Automation level	Fully automated	
	Autonomy level	Full ground command and control	

Table 1: Architecture alternatives

1.9 System Requirement Document

The SRD shown in Figure 10 illustrates the first architecture detailing the aspects that will lead to the fulfillment of the stated objectives.

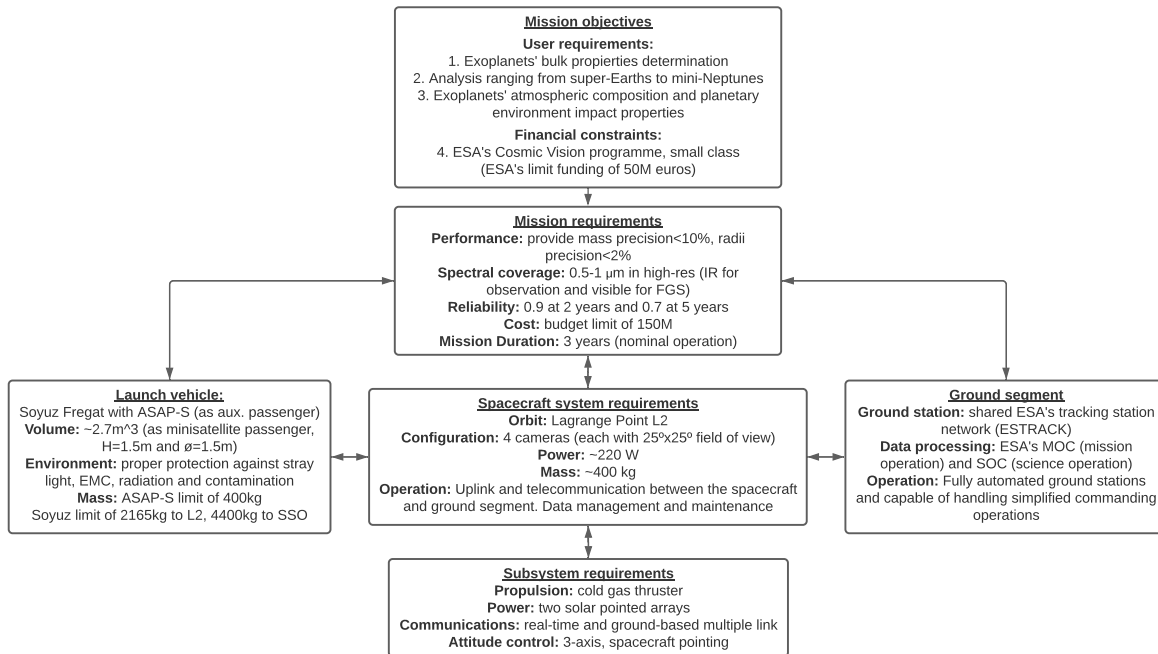


Figure 10: Objectives and requirements of the spacecraft mission (architecture option 1)

2 Space environment

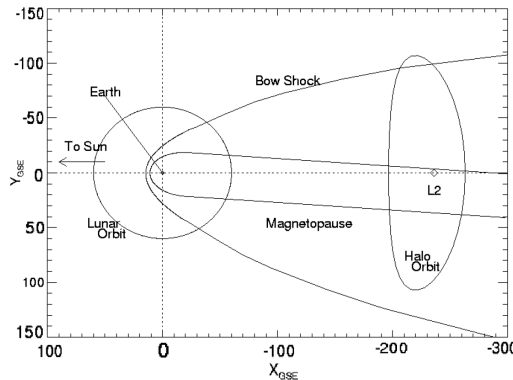
A space vehicle located in an orbit at L_2 will move along its Solar orbit with the same angular rate than the Earth, at the same time, the Earth's electromagnetic radiation influence can be assumed as negligible. Nevertheless, the spacecraft be subject to the ambient plasma and ionizing radiation environments due to both the solar wind and the geomagnetic tail. Another important source of radiation will be the galactic cosmic rays (GCR). Eventually, it is also possible that the vehicle has to face some meteoroid storms, which must also be considered. This section will cover all the stated phenomena.

2.1 Plasma environment

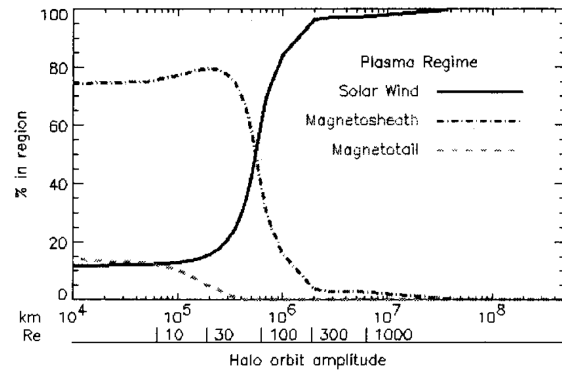
2.1.1 Magnetotail considerations

It has been already mentioned in §3.3.2 that the space telescope is not going to be statically placed in the L_2 , but orbiting around it in a halo orbit which rotation axis is almost co-linear to the Sun-Earth axis. A graphical representation can be seen in Figure 11a. Thus, this type of trajectories are prone to immerse the satellite in the magnetotail and the magnetosheath, but also to occasionally expose it to the free solar wind.

Indeed, mission designs with large amplitude (i.e. mean radius) halo orbits ($\sim 100 R_E$) will place the satellite in the magnetosheath, characterised by its high-density and low-energy plasma, and also to the solar wind for long periods of time. In contrast, halo orbits with sufficiently small amplitudes ($\lesssim 20 R_E$) will subject the space vehicle to the low-density, high-energy plasma of the magnetotail for appreciable times. Furthermore, if the amplitude of the halo orbit is on the order of the average diameter of the magnetotail ($\sim 40 R_E$), the spacecraft will surely encounter all of these plasma regions during a single orbit. Figure 11b shows the influence of each regime with respect to the orbit amplitude.



(a) Magnetotail and halo orbit around L_2 . Source: [32]



(b) Summary of the location influence. Source: [33]

Figure 11: Magnetotail and halo orbit interference.

Another aspect that shall be taken into consideration is the orientation of the magnetotail, mainly determined by the direction of the solar wind flow velocity. Assuming a reference frame fixed to the rotating Sun, the solar wind flows radially outward into space. Nevertheless, for a reference frame fixed to the Earth, the solar wind arrives on average from approximately 4° east of the Sun-Earth line.

This deflection angle of the magnetotail with respect to the Sun-Earth line is called "aberration" and is caused by the orbital motion of the Earth through the solar wind. In addition, while the mean aberration angle may be around 4° , the motion of the tail can reach limits from 15° to -5° . A graphical representation of all the stated phenomena is given in Figure 12. To conclude, the second Lagrangian point may be located anywhere within the magnetotail or even in the magnetosheath simply due to the solar wind motion [32].

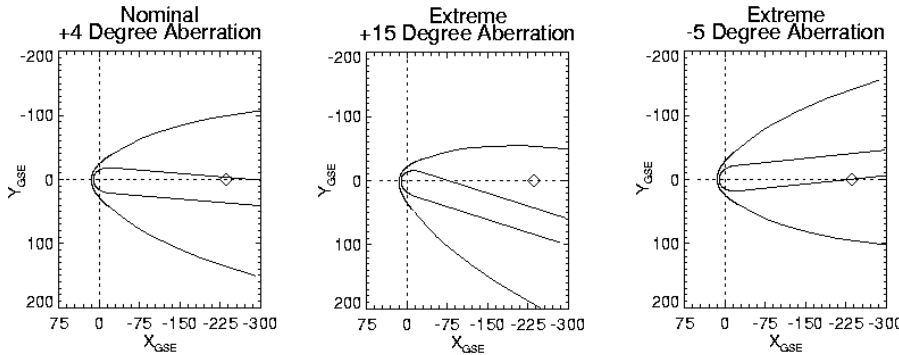


Figure 12: Magnetotail and bow shock orientations. Source: [32]

2.1.2 Plasma energetic analysis and consequences

According to [34], plasma is a partially ionized gas in which some of the atoms and molecules have their electrons stripped off. The resultant mixture of ions and electrons can penetrate matter and the depth may depend of the penetrating particle, its atomic mass and the composition of the material.

Departing from the previous definition, and considering the analysis developed in [35], both species can be further described. As regards the solar wind electrons, these are composed of two populations: a core population of high density, low energy electrons dominates with a minor density contribution due to a halo population of high temperature electrons. More specifically, density of the core population is typically ten times that of the halo population but only one tenth the temperature.

Studying the ion population, only hydrogen and helium ions should be considered due to the relatively low abundance of heavy ions in the solar wind and distant magnetotail. Indeed, hydrogen ions dominate in all cases, with helium being the most common minor species. Ions heavier than helium are present in the solar wind but represent a negligible contribution to the total solar wind mass. This same composition is applicable to both magnetosheath and magnetotail at L_2 distances because the plasma source for the latter beyond approximately $100 R_E$ from the Earth is primarily the solar wind.

Figure 13 shows the cumulative particle fluence for the above-described species for a halo orbit of 125000 km ($\approx 20 R_E$) of amplitude. This statistical study has been performed using the solar space weather data from 1992, year close to the solar activity peak of the 22nd Solar Cycle.

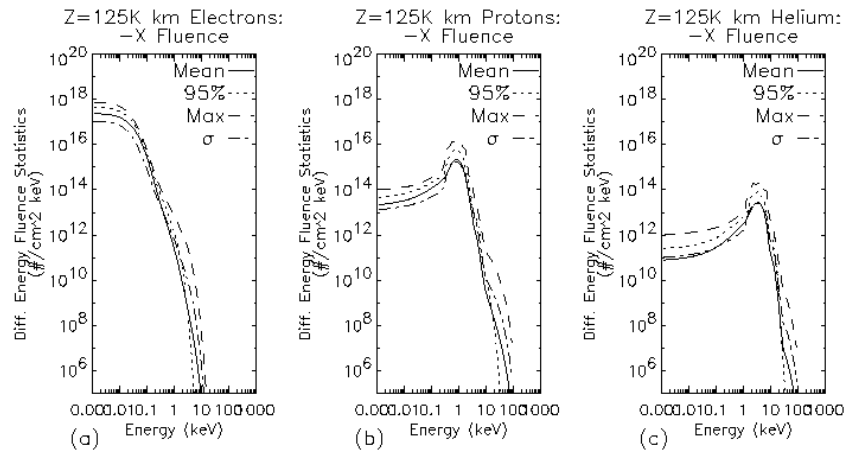


Figure 13: Fluence for a 125000 km amplitude halo orbit assuming solar weather from 1992. Source: [32]

As regards the electrons, their bulk energies are between 0.001 to 0.1 keV, reaching maximum energies of around 10 keV, whereas the protons (hydrogen ions) and the helium ions show a peak of incidence close to 10 keV and are able to reach until 100 keV. Despite being these values the correspondent to a year of high solar activity, the penetration energy ranges detailed in Figure 14 point out that the plasma is incapable of penetrating until the inner cavity of the space vehicle, but only to energize the outer

surface¹. [32] confirms this fact: while states that the energy of this particle is insufficient to penetrate shielding materials, also remarks that the primarily affected components are the external surfaces and structures of the spacecraft.

According to [33], spacecraft charging and surface degradation due to ion sputtering are the two main plasma effects on the outer covering of the spacecraft. Spacecraft charging has its origin on the differential collection of currents from the ambient plasma environment which balances the outgoing photoelectrons, the secondary electron, and the secondary ion currents produced when charged particles collide with the spacecraft surface. At the same time, sputtering can be defined as the loss of atoms from the outer surface of the spacecraft primarily due to ion bombardment.

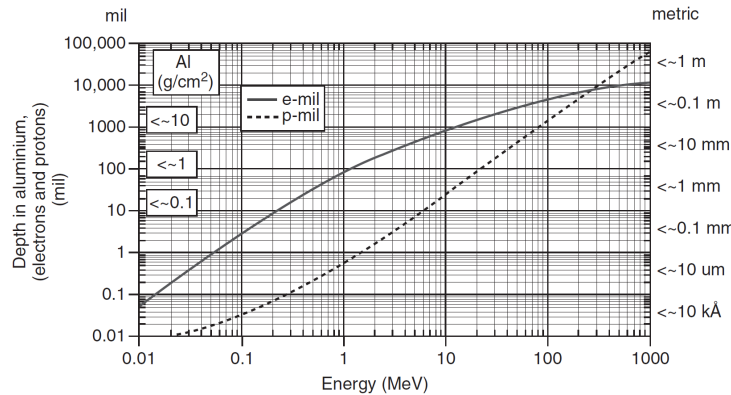


Figure 14: Electron/proton mean penetration energy ranges in aluminum. Source: [34]

[33] details that a spacecraft structure in darkness will charge to a negative potential that is a few times the electron load since there is not outgoing photoelectron current to balance the incident one caused by the plasma environment. Concurrently, the photoelectron currents leaving the sunlit surface of a spacecraft are typically much greater than the conducted current from the shaded surface. Thus, illuminated spacecraft surfaces will typically charge to positive potentials. A NASCAP GEO simulation performed in the same reference predicts potentials from -20 to -30 V for the structure in darkness and from $+6$ to $+8$ V for the illuminated surface. To conclude, differences in the order of tens of volts must be expected as regards the design of the charging protection.

2.1.3 Protection mechanisms

[34] suggests several design guidelines and recommendations to harden spacecraft systems against charging effects. First of all, the primary spacecraft structure, electronic component enclosures and electrical cable shields must provide a physically and electrically continuous shielded surface around all electronics and wiring. The aim of this shielding is to act as a Faraday cage, preventing the entry of charged particles into the spacecraft interior. In addition, it should provide a certain level of ailment of the interior electronics towards the radiated and conducted noise of electrical discharges on the exterior. Concerning this last aspect, an aluminium thickness of around 1 mm (40 mil) provides a proper attenuation of 40 dB.

Secondly, [34] also recommends bonding all the structural elements. This is, every conductive internal part should be connected to a common electrical ground reference, which in this case could be the chassis. This collection of electrically bonded structural elements, also referred to as structure ground, is aimed to provide a low-impedance path for any current caused by electrostatic discharges. Besides, this will provide an excellent ground for all other parts of the spacecraft needing grounding

¹ Aluminium has been chosen as a reference material due to its extended use in space vehicle structures, as well as for its shielding, and it is considered as the reference protection measure.

2.2 High-energy radiation environment

2.2.1 Origins and consequences

According to [32], the study of high-energy particle space environment encompasses a classification and quantification of species arising from nominal and extreme solar activity (protons, electrons and heavier ions, as described in §2.1.2), as well as those originating from extra-solar sources (mainly protons and heavier ions). An additional contribution of the geomagnetically trapped particles (protons and electrons) will be mentioned, but not considered for this study since L_2 lies outside the Earth's radiation belts, and it is only the specific transfer trajectory of the space vehicle to the aforementioned location which will determine its exposure to this trapped radiation.

This high-energy particles are capable of penetrating spacecraft shielding materials and directly affecting the operation of electronic components within the vehicle. The main damages are the reduction of the operational lifetime of spacecraft electronics and immediate data loss or damage. [36] suggests considering three damage categories:

- Degradation from total ionizing dose (TID): Cumulative long term contribution mainly caused by solar protons and electrons. It can be reduced through thickening the shielding material. Mainly applicable to internal electronic components.
- Degradation from non-ionizing energy loss (NIEL): TID-equivalent but concerning optical elements.
- Single event effects: immediate failures caused by high-energy heavier ions.

A thorough description of the damage mechanisms is given in [32]. The three described categories concern electronics, the most critical subsystem of the space vehicle. TID and NIEL lead to long-term performance degradation. In contrast, SEE cause immediate failures, reaching from non-catastrophic inversion of single data bits, to an activation of a parasitic current path that causes a permanent functional failure due to thermal destruction.

At the same time, the prolonged exposure to ionizing radiation encompasses several material effects that are going to be described hereunder:

- As regards polymeric materials, these are subject to degradation due to having their long-chain chemical bonds broken by high-energy particle penetrations, and then relinked with near neighbors, producing short-chain polymers. The results are embrittlement, loss of strength and possible degradation of electrical and thermal insulation properties.
- Crystalline materials, such as most metals, may see their bonds broken or weakened due to lattice effects and atomic displacements. The ultimate consequences are hardening and embrittlement.
- Amorphous materials, such as glasses, can have their bulk properties altered by the formation of minute crystals inside it.

Same as happened for the spacecraft charging, these degradation effects are more pronounced at surfaces, and diminish with depth into a material due to the attenuation of the particle flux.

2.2.2 Radiation description

Further expanding the definition given in the previous section, the natural radiation environment experienced by the spacecraft at the L_2 libration point is essentially composed of galactic and solar components. The first one, denoted as galactic cosmic rays (GCR), arise primarily from protons and energetic ionized nuclei originating from outside the Solar System. GCR are characterized by an omnidirectional flux of approximately 85 % hydrogen, 14 % helium and 1 % heavier ions, showing a similar proportion to the solar plasma detailed in §2.1.2. However, a notable difference concerns the GCR energies, ranging from MeV to GeV, and occasionally reaching up to TeV. Under this high-energy particles, the spacecraft shielding is ineffective in attenuating the incoming flux, fact that jeopardises the equipment reliability.

The secondary and more relevant contribution is the caused by solar flares and coronal mass ejections (CMEs), which are eruptive events that result from solar magnetohydrodynamic instabilities. Large quantities of protons and heavier ions follow the occurrence of these eruptive events, which are most probable within two years before and four years after solar peak of activity [32].

Figure 15 compares the integral fluence of both types of radiation for a ten-year mission studied with the CREME96 model. More specifically, only the highest energetic range has been plotted, as it is the main interest of this section. That the fluence of the solar ions in close to two orders of magnitude higher for energies from 0.1 to 1 MeV. Nevertheless, the incidence of the GCR shown an approximately constant progression which ranges up to energies of tens GeV. Nonetheless, it is essential to recall that this is an analysis of the highest energy contributions, and this can be proved by comparing that the fluency for Figure 15 around the half of the order of magnitude shown in Figure 13.

Additionally, the results derived from Figure 15 indicate that both TID and NIEL have a primarily solar background, while the SEE are mainly caused by the GCR and solar punctual events. These conclusions are also stated in [36].

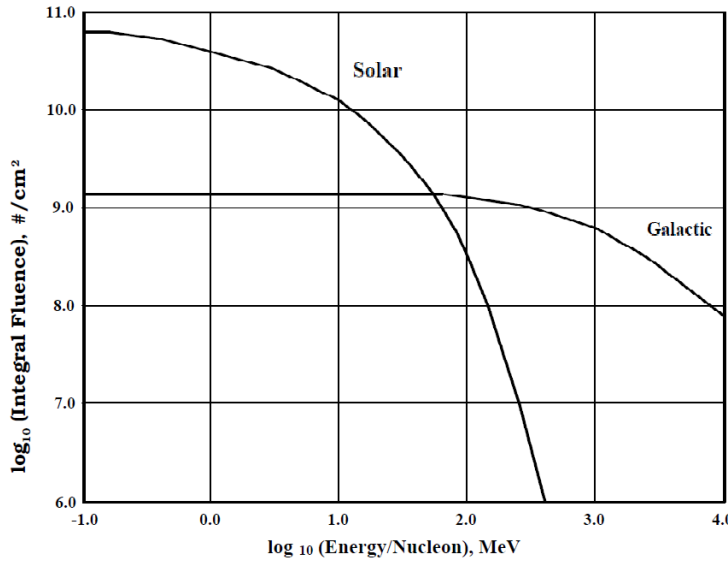


Figure 15: Ion spectra for 10 years at L2 for solar and galactic sources. Source: [32]

2.2.3 Protection mechanisms

Figure 16 shows the ionizing dose in silicon as a function of shielding thickness of aluminum for both solar and galactic cosmic radiation. First of all, and according to what was stated in §2.2.1, the solar radiation (i.e. the main contribution to TID and NIEL) can be attenuated through thickening the shielding cover. On the contrary, GCR ionizing dose is relatively insensitive to increases in shielding thickness. The graph also shows that solar protons are the primary component to the radiation dose for a shielding thickness of less than 10 cm (which accounts for most of the elements of the space vehicle). Thus, increasing the shielding may be helpful to achieve greater protection against TID and NIEL, but this measure is totally inefficient to prevent SEE caused by the GCR [32].

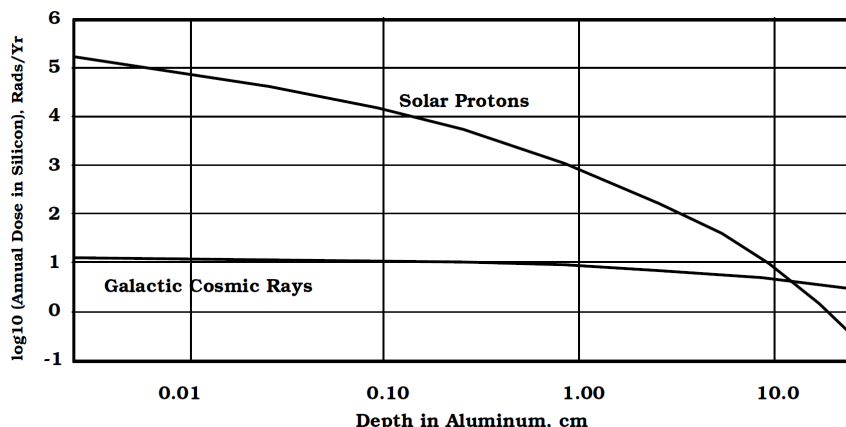
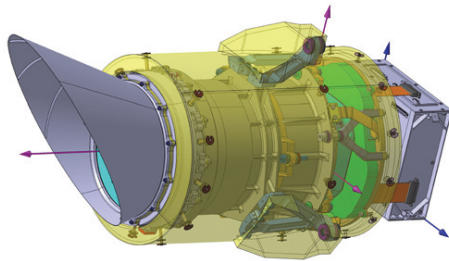


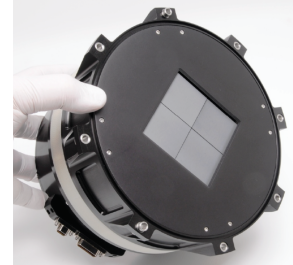
Figure 16: Dose vs. depth in aluminum for solar protons and galactic cosmic rays. Source: [32]

PLATO is an ESA exoplanet mission aimed to be launched in 2026, year that will be close to the peak of solar activity of the 25th Solar Cycle, predicted for 2025. In order to protect their cameras from the probable high-energy solar radiation episodes, a multi-layer insulating (MLI) structure has been equipped. A 3D-model view is shown in Figure 17a.

At the same time, [37] suggests including a borosilicate glass cover protection for the CCD sensors. This shielding should have a thickness of around 5 to 10 mm and would be mounted on the light shield sensor GAP, according to the picture presented in Figure 17b. This research points out that attenuation against particles with energies up to 30 MeV can be achieved.



(a) PLATO camera with MLI structure. Source: [17]



(b) TESS full detector assembly. Source: [38]

Figure 17: Magnetotail and halo orbit interference.

As a conclusion, the high-energy radiation environment at L_2 is driven by both the Solar Cycle and the GCR. Although the first contribution can be attenuated by adding shielding, the weight is always a critical factor in spacecraft design. Furthermore, selecting a period of launch and operation coincident with a minimum of solar activity would benefit in this aspect, but the GCR incidence levels will be maximum. The reason is that the solar wind is capable of scattering the GCR flux. The design will have to take this aspect into consideration.

2.3 Meteoroid environment

According to [32], the meteoroid background for L_2 is non-isotropic and sporadic, enhanced by streams of material ejected from short-period comets that pass near the Earth's orbit. Although some of these streams are notorious for producing a beautiful natural spectacle discernible from the Earth, such as the Perseids, the Draconids and the Leonids, they actually represent a time of increased risk for the spacecraft.

Table 2 presents information on those meteor streams that are known to have the potential for causing a meteor storm at L_2 . It can be seen that some of the average speeds of the streams may reach values up to 59 km/s for the Perseids and 71 km/s for the Leonids. When compared to the average of 37 km/s of the normal background, these meteor streams translate into greater-than-normal striking power.

Stream	Average speed [km/s]	Time of max. activity
Quadrantids	41	August 3 rd
κ Cygnids	25	January 18 th
Lyrids	49	April 22 nd
Draconids	20	October 9 th
Perseids	59	August 13 th
Leonids	71	November 17 – 18 th

Table 2: Meteor streams known to produce enhanced or storm level activity. Source: [32]

The impacting meteoroids are primarily small and their densities are lower than many orbital debris. However, their high impact speed makes them a serious penetration concern. They are capable of ripping thermal and radiation insulation away, as well as harm the solar cells. Again, setting a thicker shielding would be the most recommendable option.

3 Orbital Mechanics

3.1 Lagrange points destination analysis

Lagrange points are zones in space where gravitational forces of a two body system produce enhanced equilibrium regions of attraction and repulsion. These regions are highly advisable for space missions since they reduce drastically the fuel consumption needed to remain in that position. In other words, at Lagrange points, the gravitational pull of two large masses precisely equals the centripetal force required for a small object to move with them [39].

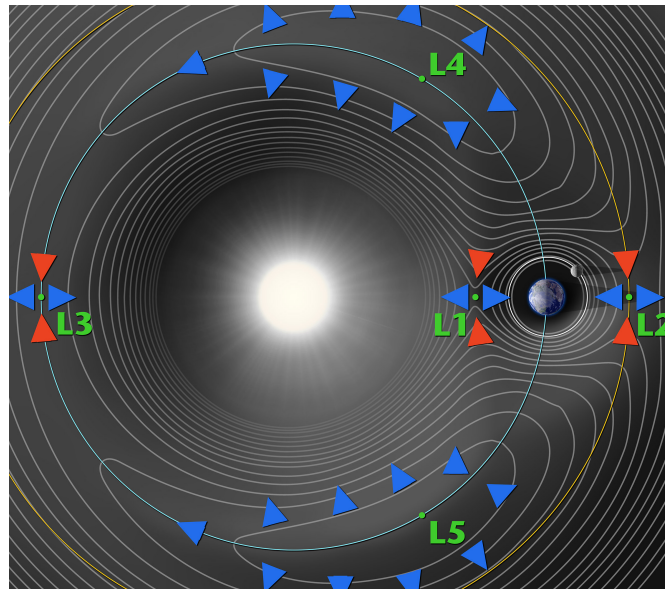


Figure 18: Visual representation of Lagrange points (not drawn in scale). Source: [39].

Any system of two large objects in space, such as the Earth and our Sun, will produce 5 points of stability, where the gravitational pull of both objects cancel each other out to create a small area where stations or satellites could be kept at a relative halt, without the need for control thrusters or orbital correction. Although this resemble a three body problem, as the third body is much less massive it is called a restricted three-body problem.

As mentioned before, these points exists in any system of two larger masses and a third much smaller mass, i.e. a space probe between Sun-Earth Lagrange points system. Nevertheless, systems like this exists between any other objects, for instance, Earth-Moon and Sun-Jupiter system.

Taking as an example the Sun-Earth Lagrange points system [40]:

- **L1:** On a direct vector between Earth and the Sun lies the Lagrange L1 position. This is the point where the direct gravitational influence of the Earth and Sun cancels out.

Lagrange point one is particularly useful as it allows for a satellite placed there to not only remain equidistant for both the Sun and Earth but also provides a position for a consistent visual the sun and the illuminated surface on Earth.

One example, of a satellite is the Solar and Heliospherical Observatory or *SOHO* satellite, which provided with Sun's gas currents below the Sun's visible surface and tracking changes in its magnetic fields.

- **L2:** On the same direction vector, but beyond Earth's orbit lies L2. The Earth gravity well maintains the position of L2 in spite of its higher orbit around the Sun, which increases the orbital period.

On disadvantage at being at L2 point is that if there is a satellite communication between Earth and the satellite, every time there's a solar flare, which gives out radio waves that interfere with radio communications so typically it is advisable to point the communication disk to the Earth but

also to the Sun behind it. So normally an orbit oscillating around L2 solves this issue, these orbits are called Halo orbits.

The L2 point of the Earth-Sun system would be future home of the James Webb Space Telescope. L2 is ideal for astronomy because a spacecraft is close enough to readily communicate with Earth, can keep Sun, Earth and Moon behind the spacecraft for solar power and (with appropriate shielding) provides a clear view of deep space for the telescopes.

- **L3:** The third Lagrange point is located on the other side of the system, far beyond the Sun. This is the point where the Sun and Earth's gravitational pull align in the opposite direction to L2.

An object place there would be eclipsed by the Sun and completely hidden from Earth. An applications of this point is to predict solar storms coming. Looking at the far side of the Sun is particularly useful as the Sun rotates and in the Earth would be able to foresee this event.

Lagrange points 1, 2 and 3 are considered unstable equilibrium points meaning an object placed there will be in equilibrium as long as they are not influenced by other forces. For this reason, these positions will still need constant thrust control to correct any misalignment. A spacecraft must use frequent rocket firings to stay in so-called Halo orbits around the Lagrangian point.

- **L4 and L5:** Lagrange points L4 and L5 are located by charting equilateral triangles above and below the direct vector of the Sun to find the gravitational barycenter.

L4 and L5 are extremely stable gravity wells that pull objects into themselves so many asteroids have been captured naturally by these wells. These regions would not require ΔV or orbital correction to maintain their position relative to the Earth and Sun.

What makes this regions interesting is that the distance and travel times between Earth and those regions always remain the same.

Let's dive on how to represent graphically the Lagrangian problem. Kepler's laws only applies to two body problems so the addition of a third mass into the equation would not be applicable.

The problem this mission is facing is a three-body problem in which the satellite's motion is affected by the gravitational motion of both the Sun and Earth. While there is no solution to general three body problem the following steps shows a Lagrangian approach to the classical Newtonian mechanics and reshape it to eliminate the need of balancing forces and inertias. In Lagrangian mechanics, the solution is obtained by taking derivatives of the kinetic and potential energy functions.

Working out the equations of a two body problem, assuming the Sun and other and its planet in a circular orbit with the respective masses to be m_p and the Sun's mass m_s , and the distance between their centers to be R and μ represent [41] [42]:

$$M = m_s + m_p$$

Where:

$$m_p = \mu M \quad \text{and} \quad m_s = (1 - \mu)M$$

The center of mass of a two-body system is called barycenter. The barycenter is located in the direction between the two bodies. With a distance μR from the Sun and a distance $(1 - \mu)R$ from the planet. Both the Sun and the planet resolve about the barycenter with an angular speed ω , where

$$\omega^2 = \frac{GM}{R^3}$$

The period is related to the angular speed through the relation

$$T = \frac{2\pi}{\omega}$$

which leads to well-known expresion for Kepler's Third Law, which states that the square of the period is proportional to the cube of the distance:

$$T^2 = \frac{4\pi^2 R^3}{GM}$$

The above expressions are the result of the *two body problem*, however, the case of study considers a *three body problem*. Hence, the Lagrangian methodology is to be applied.

First, let's introduce the reference frame. Figure 19 shows the global three body reference frame. The Sun is represented in yellow and also the satellite and Earth are depicted with its respective distances from the Sun r_s and r_p , respectively.

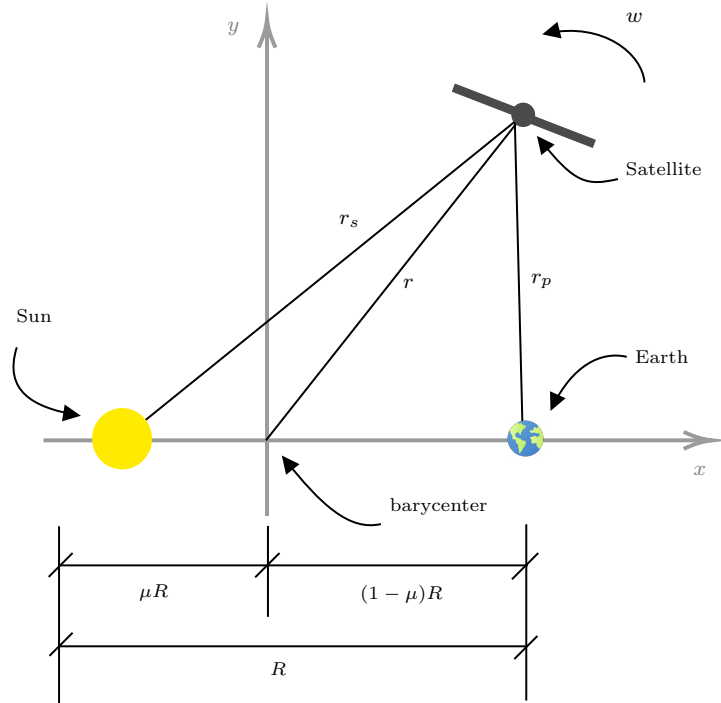


Figure 19: Three body problem rotating reference frame. Source: Own.

The origin is located in the barycenter and on the x axis between the Sun and Earth. What makes this reference frame highly interesting is the fact that it rotates with the angular velocity w . Besides, within this reference frame both the Sun and Earth is motionless and the problem is reduced to find the points where the planet is motionless too. Nonetheless, a rotating reference frame is not inertial.

As the reference frame is not inertial, acceleration terms are meant to be considered. According to Alembert's Principle [43], which is an extension of the virtual work from static to dynamical systems and separates the total forces and inertial forces (which are considered due to the movement of the non-inertial reference frame to maintain the validity of Newton's second Law):

$$F = ma \iff F - ma = 0 \quad (1)$$

D'Alembert's Principle is applicable to energy terms as well. In the restricted three body problem, the potential energy of the satellite has three terms:

$$U = \underbrace{-\frac{Gm_s m}{r_s}}_{(A)} - \underbrace{\frac{Gm_p m}{r_p}}_{(B)} - \underbrace{\frac{1}{2}m(r\omega)^2}_{(C)} \quad (2)$$

where

- (A) Gravitational potential energy due to the Sun
- (B) Gravitational potential energy due to the Earth
- (C) Centrifugal potential energy due to the rotating frame².

and

- m is the satellite's mass.

²This third term would not appear in a potential energy expression written for an inertial frame.

- r is the distance between the satellite and the barycenter.
- r_s is the distance between the satellite and the Sun.
- r_p is the distance between the planet and the satellite.

Now, let's transform the above mentioned expression into an adimensional expression. To do so, the first thing is to substitute the expressions for m_s , m_p and ω^2 into the expression for U .

$$U = -\frac{Gm(1-\mu)}{r_s} - \frac{G\mu m M}{r_p} - \frac{GMm}{2R^3} r^2 \quad (3)$$

Rewriting the r terms using non-dimensional variables,

$$r = \rho R, \quad r_s = \rho_s R, \quad r_p = \rho_p R \quad (4)$$

Rewriting the expression pf the potential energy U :

$$U = \frac{GMm}{R} \left[-\frac{1-\mu}{\rho_s} - \frac{\mu}{\rho_p} - \frac{1}{2}\rho^2 \right] \quad (5)$$

Then, finding the stationary points of U now reduces to finding the stationary points of non-dimensional within the brackets, which is represented by u .

$$u = -\frac{1-\mu}{\mu_s} - \frac{\mu}{\mu_p} - \frac{1}{2}\rho^2 \quad (6)$$

Briefly, this changed the x and y axis, see Figure

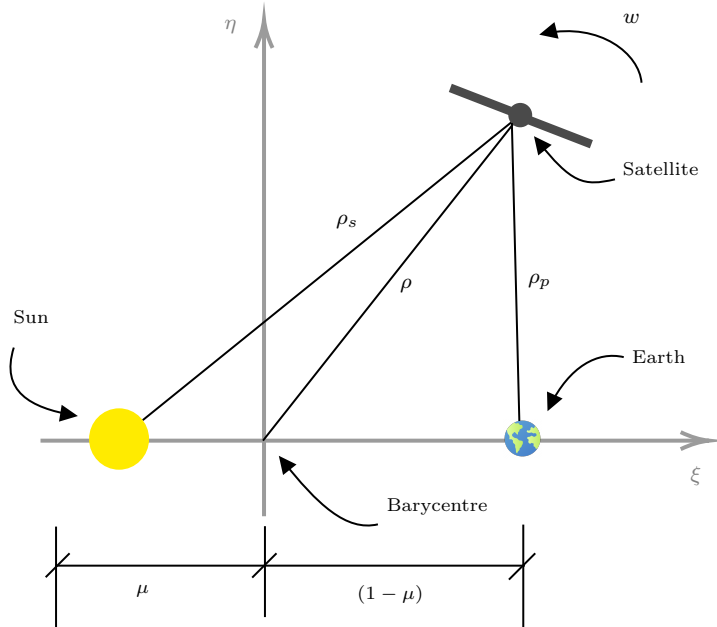


Figure 20: Three body problem reference frame (adimensional). Source: Own.

Expressing u in terms of ξ and η using Pythagoras theorem,

$$\rho^2 = \xi^2 + \eta^2 \quad (7)$$

$$\rho_s^2 = (\xi + \mu)^2 + \eta^2 \quad (8)$$

$$\rho_p^2 = [\xi - (1 - \mu)]^2 + \eta^2 \quad (9)$$

The resultant expression of the adimensional gravitational energy u goes,

$$u = -\frac{1-\mu}{\sqrt{(\xi+\mu)^2 + \eta^2}} - \frac{\mu}{\sqrt{[\xi-(1-\mu)]^2 + \eta^2}} - \frac{1}{2}(\xi^2 + \eta^2) \quad (10)$$

The above expression is represented in the Figure below:

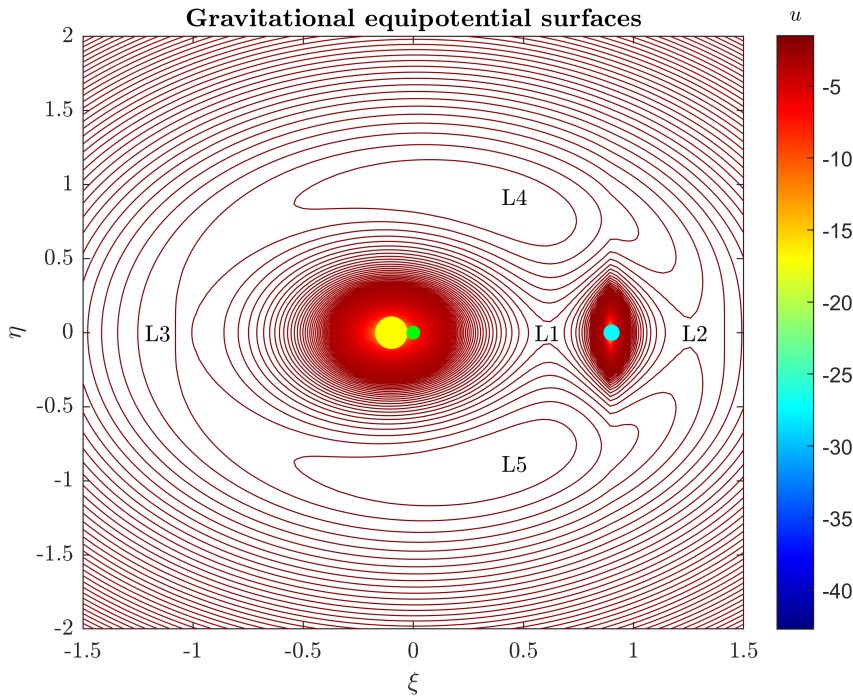


Figure 21: Representation of gravitational equipotential surfaces of Sun-Earth system and Lagrange points in a rotating system coordinates. Source: Own.

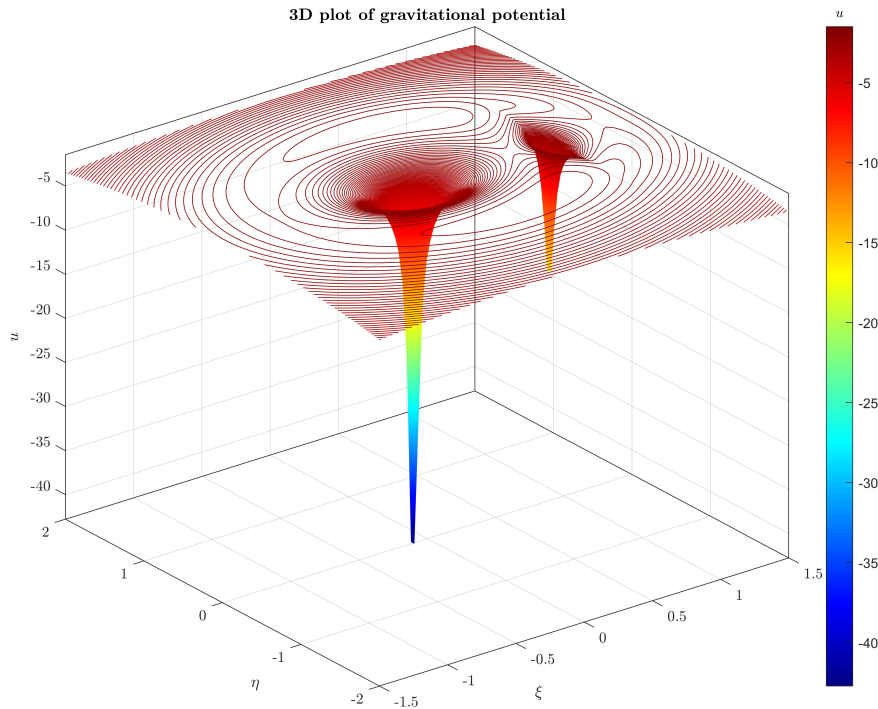


Figure 22: 3D Representation of gravitational equipotential energy of Sun-Earth system. Source: Own.

The gravitational energy (10) is presented in 2D and 3D contour plots. In Figure 21 is represented the plot of u as a function of ε (abscissa) and η (ordinate). The Sun and Earth are depicted in colour yellow and blue, respectively. Also, the barycenter is depicted which at the same time is the coordinates origin $(0,0)$ of the reference frame. Additionally, the figure shows 5 regions in which potential gravity energy is almost null due to force equilibrium between the two bodies (Sun-Earth).

It is noticeable to mention that the plot atop is presented with a $\mu = 0.1$ since that is the value that allows the plot to illustrate all Lagrange points. Otherwise, it will place points L1 and L2 so close to Earth that it would not be able distinguish them clearly.

These contour lines represent a equipotential value of gravitational energy, that is, they represent equal spacing in the value of u .

Thereby, the coordinates of the Lagrange points (though they are spatial regions) can be extrapolated. The table here-under shows the location of the 5 Lagrange points.

Point	ε	η
L1	0.609	0.000
L2	1.260	0.000
L3	-1.042	0.000
L4	0.400	0.866
L5	0.400	-0.866

Table 3: Lagrange point locations

Finally, Figure 22 presents the a three-dimensional plot of the gravitational potential energy. This figure clearly presents the different stability Lagrange points in which the influence of u is very small, whereas near the two great bodies there is a deep hole of gravitational potential energy. This explains that a satellite nearby those bodies will be highly influenced by the gravitational pull of the two massive bodies but if they stay at Lagrange points, those effects are much minor. Furthermore, recall that previously it was mentioned that L1, L2 and L3 were meta-stable points in the way that those points were unstable

equilibrium points. Take a look at L1, the picture above clearly supports this phenomena as L1 is in between the two gravitational holes.

As it will be further explained in §3.3, the L2 Lagrange point is selected to be the target destination, mainly due to its thermal stability, low radiation and absence of eclipses.

3.2 Orbital Transfers

As regards the orbital Earth to L2 transfer selection, two main options are in place: a Hohmann transfer and a high energy Lambert transfer, which are compared in Table 4.

Orbit transfer type	Advantages	Disadvantages
Hohmann transfer	High efficiency (low ΔV)	High elapsed time Circular rendezvous phasing required to L2
High energy Lambert transfer	Low elapsed time Direct injection to L2 rendezvous	High ΔV budget required Higher acceleration (rough environment)

Table 4: Orbital transfers alternatives.

The Hohmann transfer offers a low ΔV budget, thus enabling the possibility of optimising the required fuel for the mission. Nevertheless, the transfer time is considerably higher in comparison with a high energy transfer, which can make use of the entire fuel budget in order to minimise the elapsed time. Obviously, the need of more fuel implies a higher cost, so the Hohmann transfer is the most economically suitable option in spite of its higher travel time.

In addition, it must be noted that for the Hohmann alternative, since the spacecraft intercepts the L2 orbit with a slight lead angle, an additional rendezvous phasing could be required so that the spacecraft can be captured by the L2 region. In this matter, the high energy transfer is capable of performing a direct injection to the L2 rendezvous, but obviously at the expense of a higher acceleration, which involves a rougher environment for the spacecraft, highly sensible to possible vibrations.

In light of these aspects, a Hohmann transfer will be implemented due to its higher efficiency, more simplicity and lower cost. It is worth mentioning that a bielliptic Hohmann transfer has not been studied since the associated radii ratio is $\alpha = R_{L2}/R_0 = 1.01 < 11.94$, which indicates that a Hohmann transfer will always be worthier.

It must be noted that all the orbital mechanics calculations have been performed by using the implemented MATLAB code added in Appendix 2.

3.2.1 LEO parking orbit

The Hohmann transfer's starting point is to be a LEO parking orbit, as illustrated in Figure 23. For the sake of simplicity, such orbit will be circular and its height h_{LEO} will be a design variable ranging from 160 km to 1000 km, which is the height interval of a LEO orbit according to [44]. The chosen height will affect the Hohmann transfer's periapsis velocity V_0 , so its influence on both velocity budget, transfer time and mass ratio will be assessed when computing the Hohmann transfer.

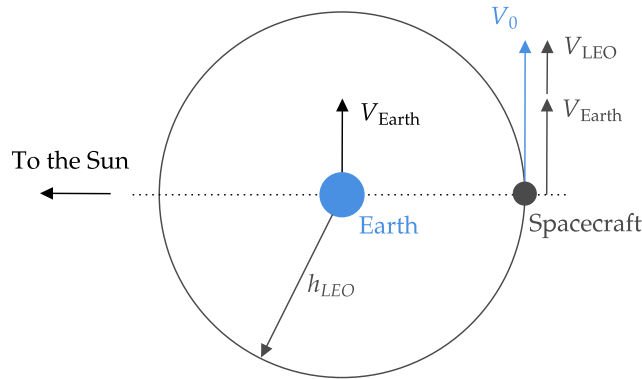


Figure 23: LEO parking orbit scheme. Source: Own.

3.2.2 Sun-Earth System L2 Hohmann transfer

The Hohmann transfer consists of a two-impulse transfer between two co-planar circular orbits. Two impulses are needed, the first to achieve the transfer orbit and the second to circularize the orbit. Thus, the total impulse is defined by the following expression:

$$\frac{\Delta V_{HT}}{V_0} = \frac{\Delta V_1}{V_0} + \frac{\Delta V_2}{V_0}$$

In this case, the apoapsis will be located at the L2 Lagrange point heliocentric orbit, whose orbital radius is $R_{L2} = R_E + h_{L2} = 1.496 \cdot 10^8 + 1.497 \cdot 10^6 = 1.511 \cdot 10^8$ km. A scheme of the orbital transfer is represented in Figure 24 for illustrative purposes.

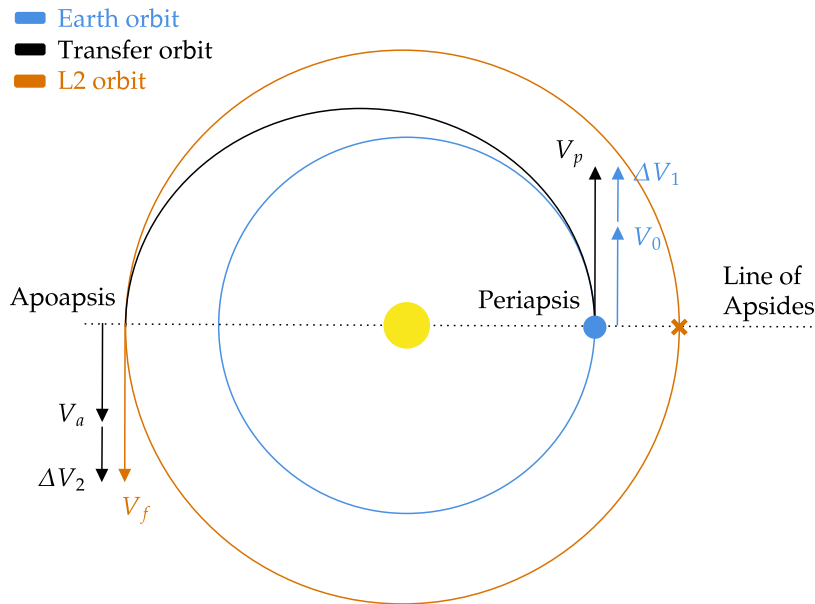


Figure 24: Earth-L2 Hohmann transfer scheme. Source: Own.

The main objective is to optimize the orbital transfer's needed fuel Δm_{HT} , defined by the expression:

$$\Delta m_{HT} = m_0 \cdot \frac{\Delta m_{HT}}{m_0}$$

where m_0 is the mass of the Soyuz's Fregat upper stage (launcher selection explained in §4.1) and its payload and $\frac{\Delta m_{HT}}{m_0}$ is the mass ratio of such vehicle.

In order to determine the minimum fuel required to complete the transfer, both terms $m_0 = m_0(m_p)$ and $\frac{\Delta m_{HT}}{m_0} = \frac{\Delta m_{HT}}{m_0}(h_{LEO})$ must be minimised as a function of the Fregat's loaded propellant mass m_p and the LEO parking orbit height h_{LEO} , respectively. The study of these terms will be assessed in the following two sections §3.2.2.1 and §3.2.2.2, respectively.

3.2.2.1 Transfer performance as a function of the LEO parking orbit height

As explained before, the height of the parking orbit is a design value, so a study is carried out in order to determine the best HT performance.

Impulse

The impulse needed in order to complete the Hohmann transfer is graphed in Figure 25 for the possible LEO heights.

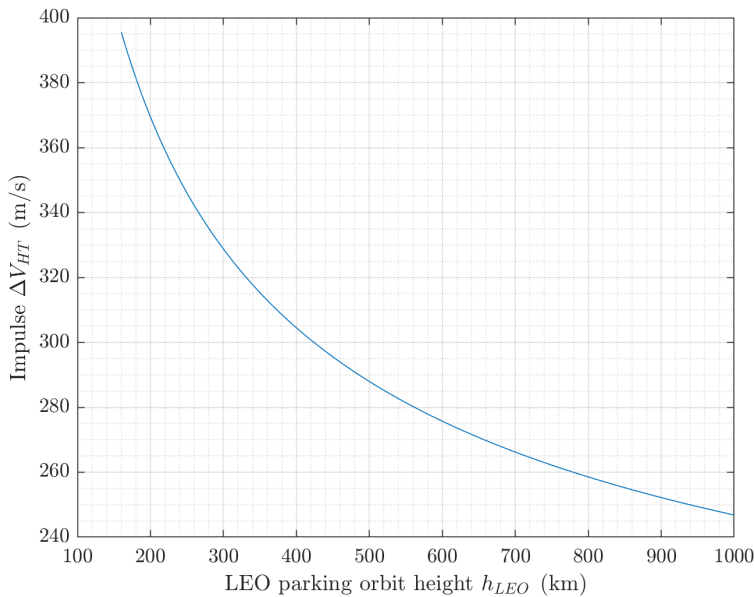


Figure 25: HT impulse variation with the height of the parking orbit

As expected, a higher LEO parking orbit implies a smaller impulse since the orbital radii ratio $\alpha = R_{L2}/R_0$ is lower, that is to say, the Hohmann transfer ellipse's eccentricity is closer to the original circular orbit, so the energy required to implement such transfer orbit is relatively low.

Transfer time

In the matter of the transfer time for different parking orbits, represented in Figure 5, it is clearly observed that there is no perceptible change in the elapsed time, being this around 184.00 days.

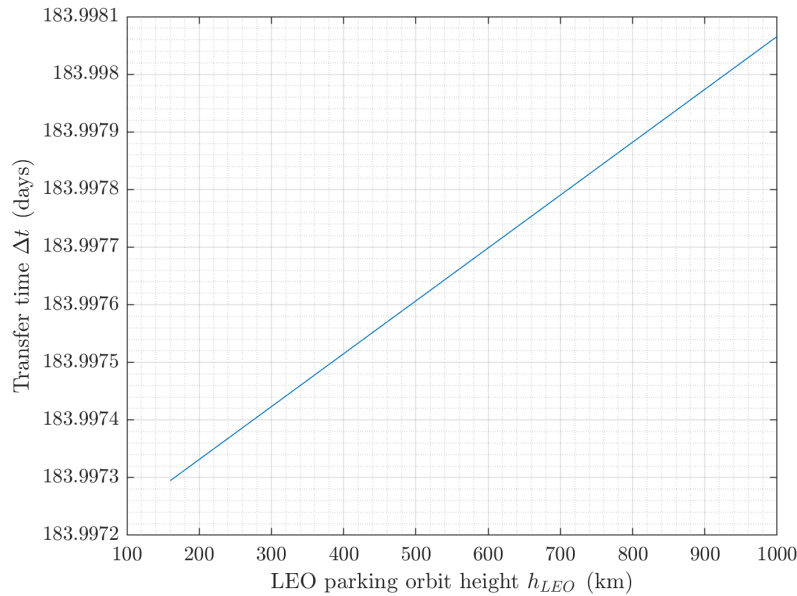


Figure 26: Transfer time variation with the height of the parking orbit

Mass ratio

As regards the mass ratio, the higher the orbit is, the lesser amount of fuel is required since the spacecraft mass variation ratio is smaller. This is an obvious consequence of the decrease in the impulse when rising the parking orbit height.

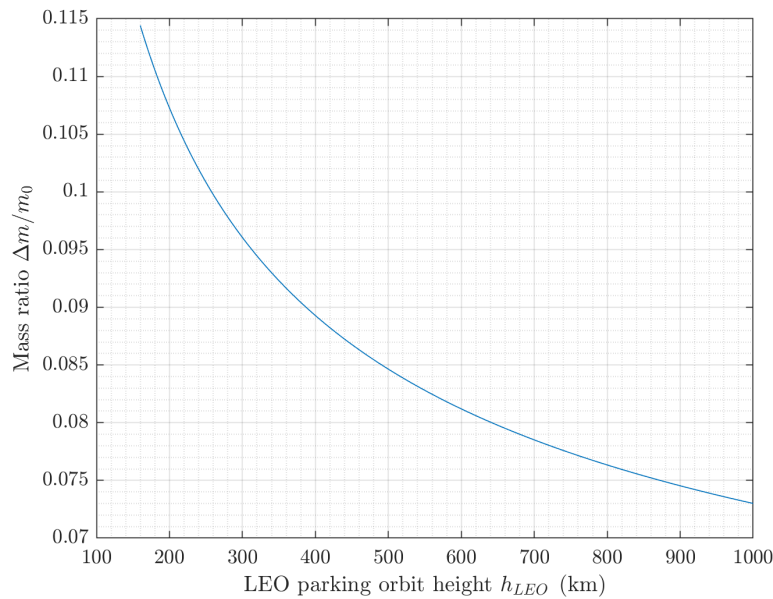


Figure 27: Mass ratio variation with the height of the parking orbit

Final performance

In light of these results and with the aim of obtaining the most efficient transfer orbit as well as remaining in the LEO height interval, a final parking LEO height of 1000 km is chosen due to its minimum impulse required and minimum mass ratio. Thereby, the corresponding performance data are summed in Table 5:

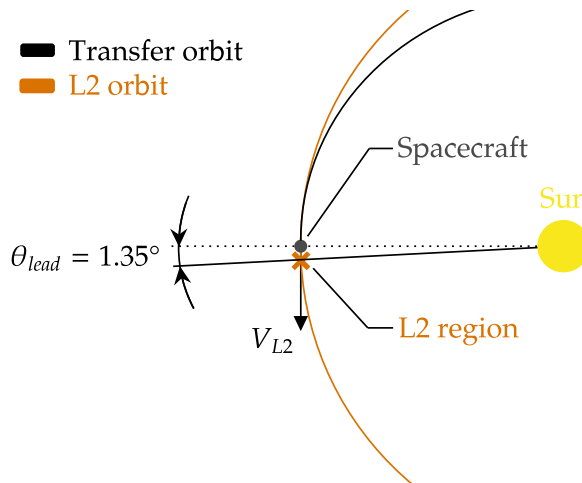
Budget ΔV_{HT} [m/s]	Transfer time t [days]	Mass ratio $\Delta m_{HT}/m_0$
246.82	184.00	0.0730

Table 5: Hohmann transfer performance.

The resulting transfer time is slightly more than 6 months, which is a 0.76% greater than the orbital period of the L2 point (coincident with the Earth's period). Since the time that is required to L2 to reach the apoapsis of the orbital transfer is less than the transfer time, there will be a little lead angle between the L2 region and the spacecraft at its arrival at the apoapsis, as represented in Figure 28. Specifically, such lead angle is defined by:

$$\theta_{lead} = \theta_{apoapsis} - \theta_{L2-} = 180^\circ - 181.35^\circ = -1.35^\circ$$

This angle difference is negligible, so there is no need of performing a circular rendezvous phasing in order to exactly reach the L2 region. In fact, since the spacecraft final orbit must be a halo orbit around L2, the corresponding injection start is executed in the apoapsis of the Hohmann transfer and taking into account the aforementioned lead angle.

**Figure 28:** Spacecraft arrival at L2 region. Source: Own.

It must be mentioned that this lead angle cannot be suppressed by the implementation of a rendezvous opportunity window since the angular velocity of both Earth and L2 are identical.

Finally, the geometric data of the transfer is shown in Table 6:

Initial orbital radius R_0 [km]	Radius ratio α	Semi-major axis a [km]	Eccentricity e
$1.496 \cdot 10^8$	1.010	$1.504 \cdot 10^8$	0.005

Table 6: Hohmann transfer orbit geometric data.

3.2.2.2 Transfer fuel budget optimization

In order to do minimise the fuel required to complete the Hohmann transfer, the propellant that is loaded into Fregat will have to be the minimum that it needs not only to complete the orbital transfer, but also to perform attitude control actions as well as bearing in mind a margin fuel for reserve purposes. These aspects are further explained in §4.3.2.

It must be recalled that the initial mass m_0 at the transfer's periapsis only depends on the loaded propellant m_p and is defined by the following expression:

$$m_0 = m_0(m_p) = m_{Fregat}(m_p) + m_{PL} \quad (11)$$

In the case of Fregat, its mass m_{Fregat} is defined such that:

$$m_{Fregat}(m_p) = m_p + m_{dry} = m_p + 902 \text{ kg}$$

where the dry mass is $m_{dry} = 902$ kg and the loaded propellant mass m_p is a design value to be computed later.

The other term that contributes to the initial mass is the payload, whose mass m_{PL} can be modeled as:

$$m_{PL} = m_{sc} + m_{ASAP} + m_{main} = 2075\text{kg}$$

where $m_{sc} = 400\text{kg}$ is the mass of the EXOHALO L2 spacecraft, $m_{ASAP} = 425\text{kg}$ is the mass of the ASAP-S payload adapter and $m_{main} = 1250\text{kg}$ is an estimated maximum mass for the main Soyuz passenger. Bear in mind that the latter mass must be considered since the EXOHALO L2 spacecraft only travels as piggyback. In addition, it must be noted that since this is intended to be a realistic mission, the tailored m_{PL} value is practically the maximum the Soyuz can carry to L2 (2165kg), so there is no much payload mass margin left as it would be in a real mission.

In order to minimise the cost of the mission and according to equation (11), the amount of fuel required in order to complete the Hohmann transfer must be optimised with the variation of the amount of propellant loaded in the Fregat upper stage m_p . The obvious decision is to load only the fuel needed to perform the orbital transfer (Δm_{HT}) and the corresponding attitude control and reserve tasks, being the total fuel mass symbolised as Δm_{total} . Thus, the minimum fuel used is $\Delta m_{total} = 1.22\Delta m_{HT}$ (refer to §4.3.2 to see the equation's origin), so the optimisation is achieved in the case of loading this same amount, that is to say $m_{p,min} = \Delta m_{total}$. If this condition is imposed in equation (18), the minimum fuel budget can be computed as:

$$\Delta m_{HT, min} = \frac{m_{PL} + m_{dry}}{1 - 1.22 \frac{\Delta m_{HT}}{m_0}} \cdot \frac{\Delta m_{HT}}{m_0}$$

Specifically, this minimum fuel budget is:

$$\Delta m_{HT, min} = 238.59 \text{ kg}$$

In order to validate this minimum value, the progression of the transfer fuel is represented as a function of the propellant mass loaded, graph which can be observed in Figure 29:

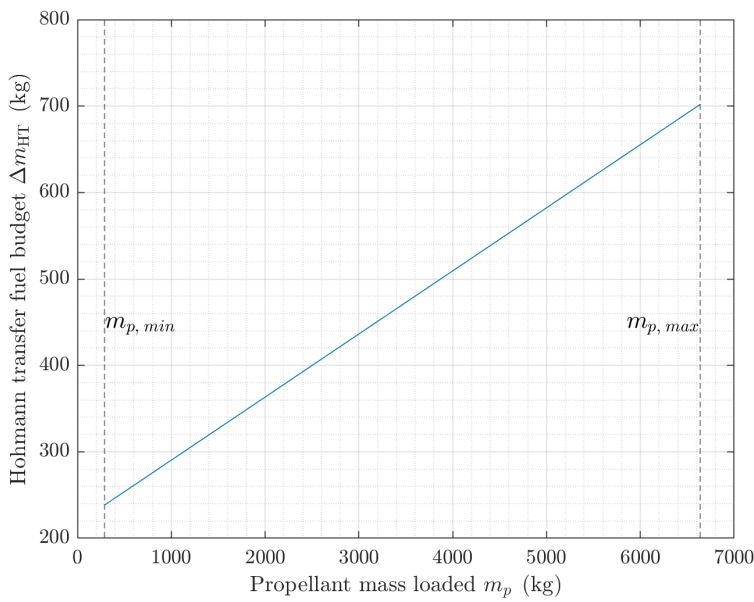


Figure 29: Transfer budget variation with the fuel loaded

As observed, the minimum propellant mass $m_{p,min}$ implies the minimisation of the HT fuel budget m_{HT} . This represents a 66.01% fuel reduction in comparison with the required budget for the Fregat maximum propellant load $m_{p,max} = 6638$ kg.

3.3 Justification of the chosen orbit in relation to the mission objective(s)

3.3.1 Lagrange L2 point

Once all the Lagrange points have been analysed, the L2 point is the one selected for the EXOHALO L2 mission.

Considering that all lagrange points allow a stable environment to carry out exoplanetary exploration, the orbits around the L2 point are the ones that offer the best performance in order to match the mission requirements while facilitating the design of the mission. As a justification, the L2 point environment offers:

- **Absence of eclipses:** The fact that of being a point where there is no presence of ellipses allows the power subsystem to have the solar energy as its primary and uninterrupted source. Likewise, the use of solar panels is optimized and secondary sources such as batteries are much less requested, thus being able to offer better performance.
- **Thermal stability:** A stable environment at a thermal level allows all electronic components to work at maximum performance without great concerns about the abrupt temperature gradients that may be caused. Likewise, if the satellite is located in a thermally stable environment, the heat and energy balance will be much easier and cheaper to balance.
- **Low radiation:** As is well known, radiation is one of the great reasons why most of the electronic elements on board satellites suffer great degradation. By locating our mission the L2, we achieve that the radiation doses that will affect our satellite are remarkably small, so the useful life of the electronic components that will make it up can be lengthened.

3.3.2 L2 Halo orbit

As Lyapunov orbits are not suitable for space applications since they do not allow the out-of-plane motion, an approach with a Halo orbit is considered. Then, although a Lagrange point is just a point in empty space, it can be orbited as the result from an interaction between the gravitational pull of the two planetary bodies and the Coriolis and centripetal accelerations of the satellite.

A halo orbit is a three dimensional orbital movement, based on the combination of two-dimensional periodic motion in the ecliptic plane and one independent periodic motion out of the ecliptic, resulting in the description of a three-dimensional path figure. Moreover the halo orbits are also known because its orbital plane does not intersect any celestial body as a classical orbit does.

As appreciated in figure 30, halo orbits are characterised by its amplitudes corresponding to the three movements defined before. Therefore the corresponding frequencies to these periodic oscillations will also define the halo orbit character. Both amplitudes and frequencies can be computed depending on the desired mission observation objectives and they would define the ΔV requested for the orbit injection, and the required ΔV for the orbital maintenance.

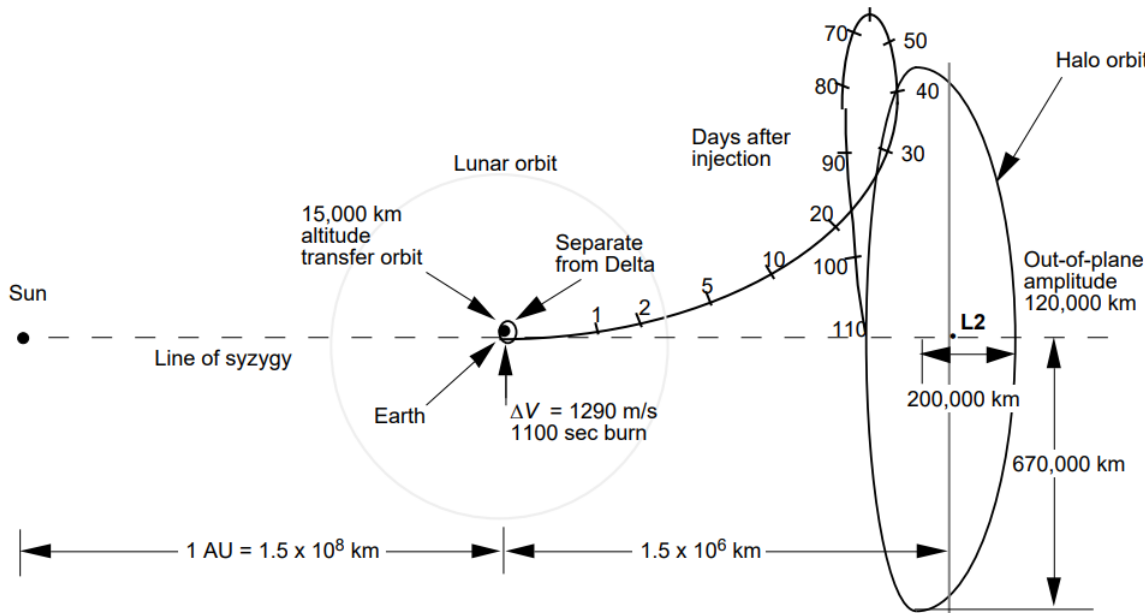


Figure 30: Geometry of L2 halo orbit. Source: [45]

According to [46], a satellite around the Sun-Earth L2 point must avoid eclipses and so requires a 3D periodic orbit. Since the R3BP does not have any analytic solution, the halo orbits are difficult to obtain because the problem is highly non-linear and small changes in the initial conditions break the periodicity of the orbits. However, it is possible to find a simplified line of study if we consider the periodic behaviour that solutions achieve when the R3BP equations are linearized. Therefore, due to this periodic tendency of the solutions, some of the halo orbits main parameters can be studied in order to set some approximated values and define the halo orbit that our spacecraft is supposed to achieve.

Following the [47] guidelines and proceeding with the appropriate mathematical development, the linearized equations resulting from the R3BP study between the Sun, Earth and the Satellite orbiting around L2, can be computed:

$$\ddot{x} - 2\dot{y} - (1 - 2c_2)x = 0 \quad (12)$$

$$\ddot{y} + 2\dot{x} + (c_2 - 1)y = 0 \quad (13)$$

$$\ddot{z} + c_2\dot{z} = 0 \quad (14)$$

Where:

$$c_2 = \gamma^{-3}(\mu + (-1)^2(1 - \mu)(\frac{\gamma}{1 - \gamma})^3)$$

$$\gamma = d(m_2, L2) : \text{distance between Earth and L2}$$

$$\mu = d(m_1, \text{GC Sun-Earth}) : \text{distance between Sun and Sun-Earth system gravity center}$$

From the equations presented above, it can be appreciated that while the orbital motion in the x-axis and y-axis is coupled, the z direction has a simple harmonic solution, easy to calculate, and not depending on any x or y term. Despite existing several solutions for these differential equations, just one of them has a periodic tendency, and they are given by the following expressions:

$$x = -A_x \cos(\lambda t + \phi) \quad (15)$$

$$y = kA_x \sin(\lambda t + \phi) \quad (16)$$

$$z = A_z \cos(\nu t + \psi) \quad (17)$$

Where:

$$k = \frac{\lambda^2 + 1 + 2c_2}{2\lambda}$$

Additionally, it is observable that the amplitudes for the x,y and z axis movement are different. A_x is referring to the in-plane amplitude, when A_z refers to the out-of-plane motion. Hence, both of them allow to characterize the size of the halo orbit.

The 15, 16 and 17 expressions are a result of the linearized periodic motion regarding the Lissajous orbits. More specifically, halo orbits are a group of orbits embedded within the group of Lissajous. In the following figure 31 the three Lissajous orbit plane motions, X-Y, X-Z and Y-Z respectively, are presented. The combination of different values for the amplitudes A_x and A_z at the same time that frequencies λ and ν can variate too, result in the several overlapping plots that appear in the figure below and characterise the Lissajous orbits. As example, the Gaia mission used a Lissajous orbit resulting from the combination of these 3 plane motions and its 3D motion is represented in the figure 32.

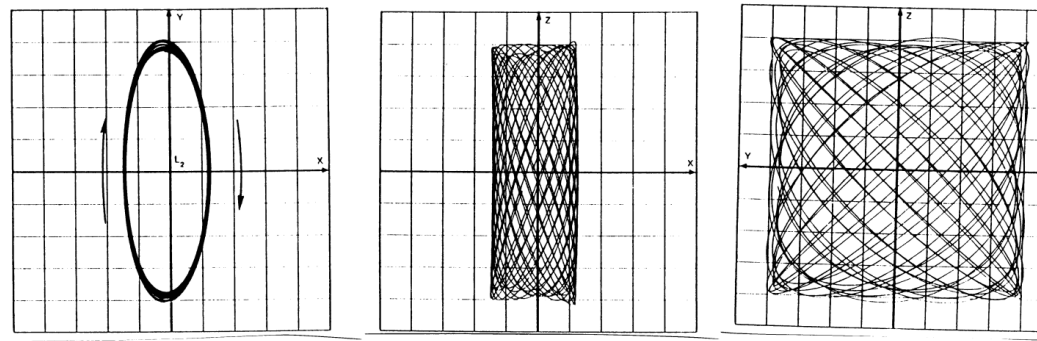


Figure 31: 3 plane motion referred to a Lissajous orbit. Source: [47]

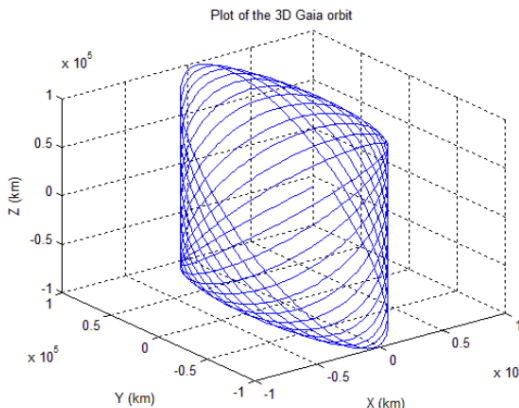


Figure 32: 3D representation of a Lissajous orbit. Source: [48]

Considering that only the halo orbits are our study subjects, as [47] states, they took place when the previous solutions are particularized to the point where frequencies for in-plane and out-of-plane motions are the same ($\lambda = \nu$). However, $\lambda = \nu$ could only happen when both in-plane and out-of-plane amplitudes are large enough to start considering the nonlinear contributions of coupled movements and particularise the satellite motion round the L2 point as a halo orbit.

The 3 plane motions presented in figure 33 are representing the International Sun-Earth Explorer 3 (ISEE3) halo orbit that is characterised by:

- $\lambda = 2.086$

- $\nu = 2.086$
- $A_x = 206000 \text{ km}$
- $A_y = k \cdot A_x = 665000 \text{ km}$
- $A_z = 110000 \text{ km}$

*Data extracted from [47]

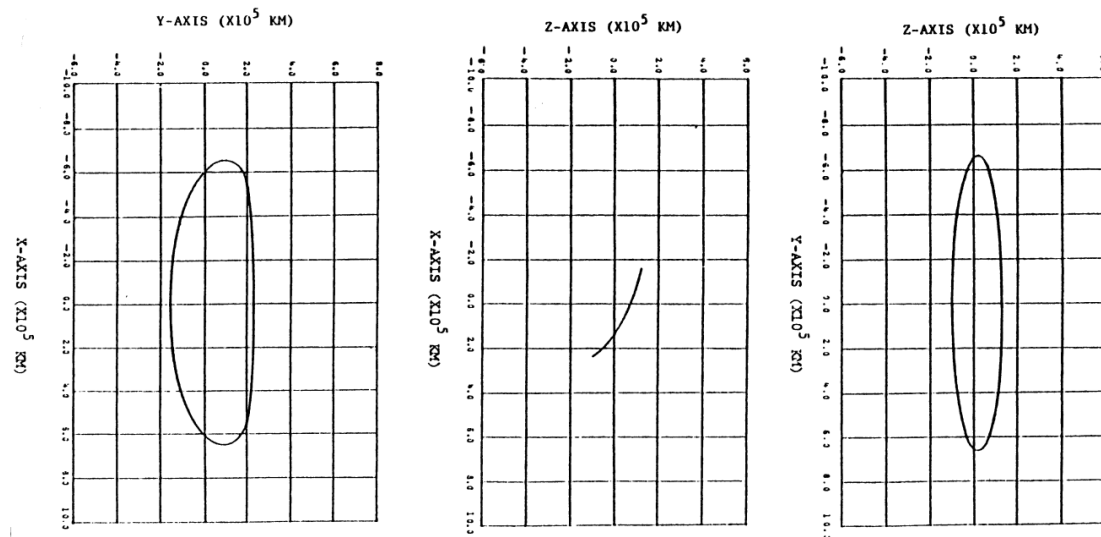


Figure 33: ISEE 3 halo orbit motion round Sun-Earth L1. Source: [47]

However, on the one hand, ISEE3 is following its halo orbit around L1 Sun-Earth point, and for that reason the amplitude values presented above, must be checked with other amplitude values corresponding to other missions orbiting L2. On the other hand, halo orbits tend to share the similar frequency values, depending on the mission observation requirements and the expected life-time. Therefore the frequency values of the ISEE3 mission that characterise its halo orbit could fit for our mission too.

When the Sun Earth Lagrange point is orbited, also with the main mission objective referred to the exoplanets exploration, large amplitude halo orbits offers a better performance.

In order to set a more accurate values for our halo orbit amplitude around L2, the approximated and estimated parameters of the ESA's PLATO mission [17] and Herschel mission [49] halo orbits, when they are considered with a linearized evolution following the previous equations, are presented in the next table.

Parameter	Herschel Mission	Plato Mission
A_x amplitude	250000 km	300000 km
A_y amplitude	750000 km	850000 km
A_z amplitude	300000 km	250000 km

Additionally, figures 34 and 35 show the halo orbits of Herschel mission and the one expected for the Plato mission.

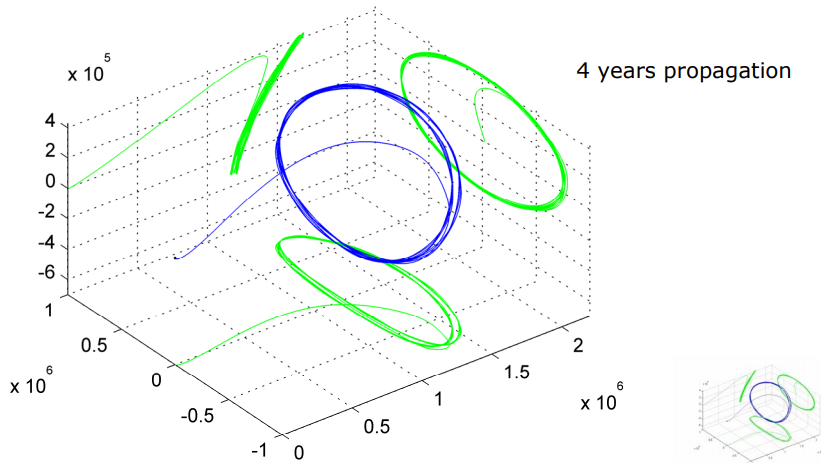


Figure 34: 3D representation of the Herschel mission halo orbit. Source: [50]

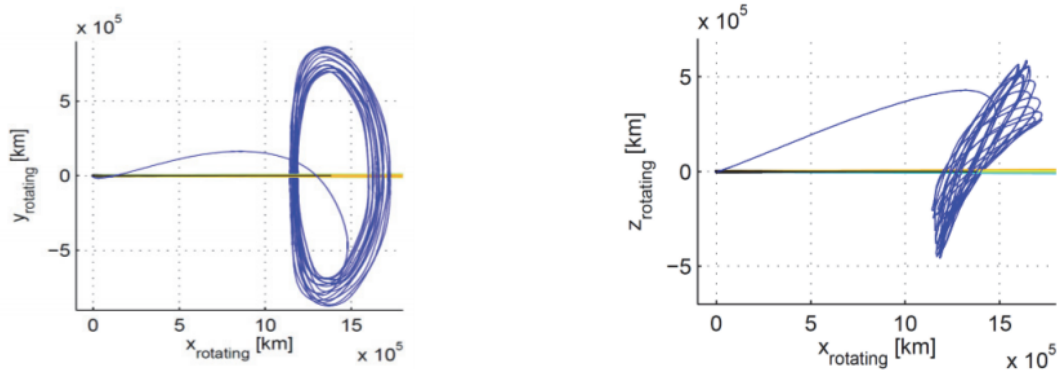


Figure 35: 2D plot of the in-plane motion for the expected Plato's halo orbit. Source: [17]

Hence, with all the information related with the halo orbits and which is presented in the previous pages, we are able to make an idea of how the main amplitude and frequency parameters that will characterise the EXOHALO L2 mission orbit round L2 will be. However, if a more exhaustive studied of these kind of orbits is regarded, numerical and computational methods, will be needed to perform in order to achieve more accurate solutions of the differential equations regarding the R3BP.

Finally, once all the parameters and definitions for the halo orbit have been set, in addition to the previous justifications for using the halo orbit round the L2 point, this type of orbit makes possible the fact of providing a continuous and uninterrupted view of the mission subject, therefore it is the orbit option that matches the most with the mission observation requirements. In conclusion, these kind of orbits are supposed to provide the best opportunities for surveillance, communications or exploratory missions.

4 Launch Considerations

4.1 Launcher selection

There are several criteria to be considered in order to select the proper launch vehicle. In first place, due to ESA's partnership with ArianeGroup, only the vehicles from this fleet will be considered as potential candidates to be used as the definitive space launcher. Specifically, these will be:

- Soyuz 2-1b Fregat: ESA's and Roscosmo's medium-lift launcher
- Ariane 5G: ESA's reference heavy-lift launcher
- Ariane 6-62: ESA's next-generation launch vehicle and successor of the Ariane 5

The initial criteria to select the launch vehicle are: performance, availability, payload compatibility, costs and reliability, aspects which will be analyzed in the following subsections.

Table 7 gathers the main criteria for each launcher, being the best options the ones highlighted in blue.

Criteria		Soyuz 2-1b Fregat	Ariane 5G	Ariane 6-62
Performance	Weight capability to L2 (kg)	2165	6600	3500
	Insertion accuracy ($\pm 3\sigma$)	a: $\pm 12\text{km}$ e: $\pm 1.20 \cdot 10^{-3}$	a: $\pm 7.5\text{km}$ e: $\pm 1.05 \cdot 10^{-3}$	
Availability	Attempts per day	≥ 2 (33min launch window)	≥ 2 (45min launch window)	
	Launch site	Kourou, French Guiana		
Payload adapter compatibility		ASAP-S ($\leq 400\text{kg}$ as minisatellite piggyback)	Dual launch	MLS ($\leq 400\text{kg}$ as piggyback)
Costs	Specific cost (k\$/kg)	27.8 ³	23.4	-
	Launch cost (M\$)	37.5	165.0	75.0
Reliability (%)		98.40	94.85	-

Table 7: Selection criteria for each launch vehicle. Source: data retrieved from [17][51][30][52][53][54][55]

4.1.1 Performance

Weight capability to L2

Since the target orbit is the Lagrange point L2, the different payload weight capabilities must be compared.

Soyuz offers the least performance with 2165kg, followed by Ariane 6-62 with 3500kg and finally Ariane 5G with 6600kg. It must be mentioned that there are more powerful versions of Ariane 6, as the model 64, but since the EXOHALO L2's spacecraft is classified as a microsatellite, there is no need of using launchers in the heavy lift operational mode since the launch cost would be higher. Due to these facts, both Soyuz 2-1b Fregat and Ariane 6-62 are the best suited launchers in terms of weight capability.

Injection accuracy

The launcher's navigation system determines its accuracy to perform the injection to a specific orbit. This accuracy is measured with a variation of 3 times the typical deviation ($\pm 3\sigma$).

For simplicity purposes, only the semi-major axis and the eccentricity of the orbit will be compared for a SSO mission. As observed, both Ariane 5G and 6 offer a 37.5% and 12.5% better accuracy in terms of semi-major axis and eccentricity, respectively.

³Lower cost only if the piggyback option is considered in comparison with an Ariane 5G dual launch payload configuration

4.1.2 Availability

Attempts per day

The three launchers provide at least 2 launch attempts per day, being the launch window the differentiating factor. Specifically, both Ariane provide a 36.4% greater window.

Launch site

There is no difference regarding the launch location, being this the ESA's Kourou spaceport at French Guiana.

4.1.3 Payload adapter compatibility

When selecting the best launcher, the payload accommodation is one of the most critical factor to consider. Bear in mind that the weight requirement of EXOHALO L2's mission states that the spacecraft's mass shall be no more than 400kg, thus being considered a minisatellite (range of 100-500kg).

In order to reduce costs, the piggyback options will be considered for each launcher. Both Soyuz and Ariane 6 offer piggyback configurations for satellites with $\leq 400\text{kg}$. In the Soyuz's case, this is achieved by the ASAP-S payload adapter, whereas Ariane 6 uses the Multi Launch Service (MLS) adapter. Both options are valid in comparison with Ariane 5G, which offers an insufficient minisatellite accommodation capability of $\leq 300\text{kg}$ as piggyback with the ASAP-5 adapter^[56]. Hence, a dual launch payload configuration must be used, thereby increasing the launch costs.

4.1.4 Costs

The specific cost of Soyuz is a 18.8% higher than Ariane 5G's, nonetheless, this is not truly representative since the specific cost would be reduced for the Soyuz by using the piggyback option, in comparison with the Ariane 5G's more expensive dual launch configuration.

As per the launch cost, Soyuz offers a 4-times cheaper launch in comparison with the heavy lifter Ariane 5G, and half the price of Ariane 6-62's cost.

4.1.5 Reliability

In terms of reliability, Soyuz posses a 3.55% better performance in comparison with Ariane 5G after a total log of 128 success and 2 failures on the 2000-2017 time interval. In comparison, the 92 successes and 2 failures of Ariane 5G decrease its reliability to 94.85%.

obviously, there is no data available for Ariane 6 since its operational cycle is set to begin on 2022.

4.1.6 Final selection

Even though Soyuz has slightly lower performance and availability, it offers the best payload accommodation with the minisatellite piggyback option and the corresponding costs are the minimum thanks to the piggyback configuration. Besides, its reliability is the highest with a 98.4%. Due to these facts, Soyuz (Figure 36) is the selected launcher, nonetheless, Ariane 6 could be an excellent option when it starts its operational cycle.

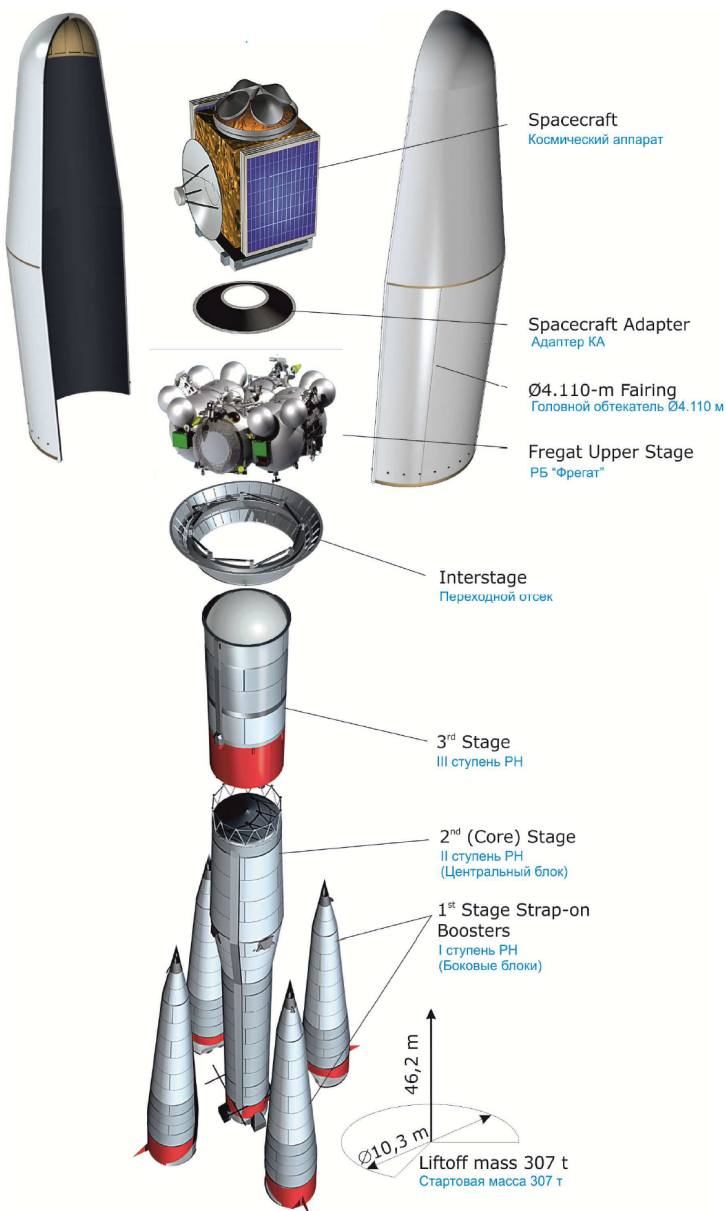


Figure 36: Soyuz launch vehicle. Source:[51]

4.2 Launch dynamics: Ascent profile

Once the vehicle has been selected, the launch dynamics of the Soyuz is studied from two different point of views, the simplified one and the more complex and realistic one.

The simplified way is based on the application of the theory guidelines equations regarding the launch dynamics, by taking several assumptions that make the calculations easier and much more acceptable to work with.

- The trajectory will be considered a rectilinear ascent, with no pitch angle rate.
- The equation referring to the summation of moments with respect to the center of gravity of the rocket is not considered for the dynamics calculation.
- The thrust force direction will be considered totally aligned with the launcher axis of symmetry. Thus the δ angle will be assumed nearly to 0.

Therefore the ascent trajectory which is going to be used be means of this simplified analysis will only consider the first two stages of the flight, where these assumptions will not interfere too much in the final results and those could be consider similar to the realistic ones. For the third and upper stages the constant pitch angle assumption will become too abusive and the results won't be similar to the desired.

With these assumptions the resultant equations for the preliminary study of the first and second stages ascent trajectory are the following.

Firstly the ascent trajectory study will involve the altitude and the range computation. These two variables are calculated by working with the two kinematic equations from the X-axis and the Y-axis, resulting in:

$$\frac{dh}{dt} = v \cdot \sin(\gamma)$$

$$\frac{dx}{dt} = \frac{R_E}{R_E + h} v \cdot \cos(\gamma)$$

On the other side, the dynamic equations evolution will give us the velocity ascent profile and consequently the acceleration level to which the spacecraft is going to be subjected. Due to the fact of projecting the forces in both tangential and normal axis of the rocket, the total acceleration module is divided on its two main components, the tangential one and the normal one.

For the tangential evolution:

$$\frac{dv}{dt} = \frac{T}{m} \cos(\alpha) - \frac{g}{m} \sin(\gamma) - \frac{D}{m}$$

Then, regarding the normal evolution, the final pitch angle that which characterise the final relative position of the spacecraft can be computed. However, as we have assumed that during the first two stages ascent, a constant pitch angle is going to be considered, the equation resulting from these normal axis balance is not going to be object of study.

Finally in order to characterise the Soyuz engines performance at the time of generating the Thrust force for boosting the launcher, the most relevant data extracted form [51] as the specific impulse, the nozzle throat and nozzle exit section surfaces, the exhaust gas temperature resulting from the combustion process and the total propellant mass needed for each stage is obtained.

Additionally is necessary to mention that, as a constant pitch angle is considered during both of the stages ascent evolution, in order to make the results the more realistic as possible:

- First stage: 90°
- Second stage: 45°

Once all the data and the equations are set in the attached Matlab code, the differential equations system, resulting from the altitude and the velocity evolution, is solved using the Runge-Kutta fourth order algorithm which allows us to find the altitude and velocity values and evolution during the first two stages time duration, which is near to 300 seconds, more exactly 282 seconds.

Therefore the following plots of are obtained:

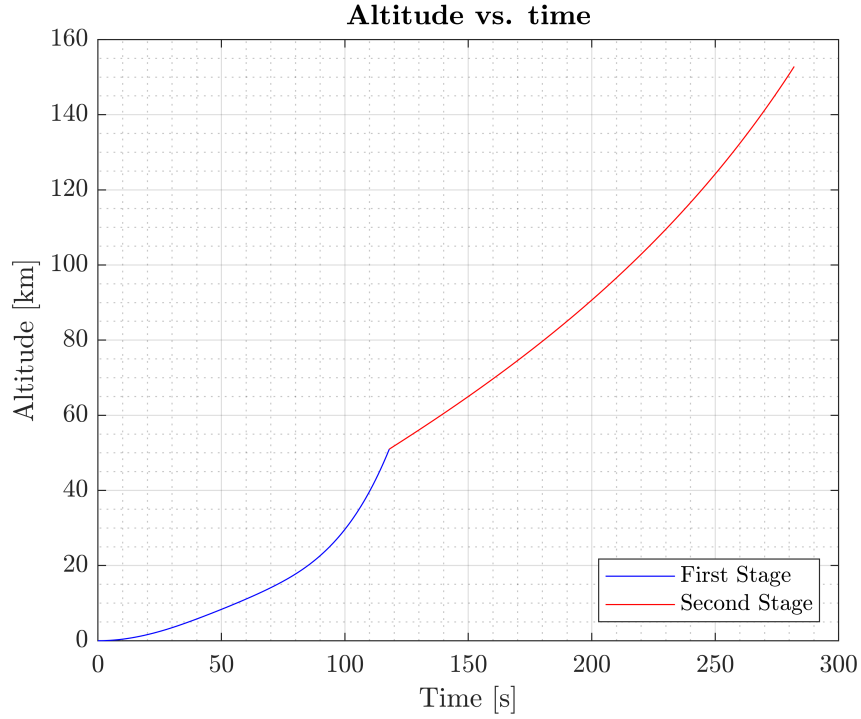


Figure 37: Altitude evolution vs time.

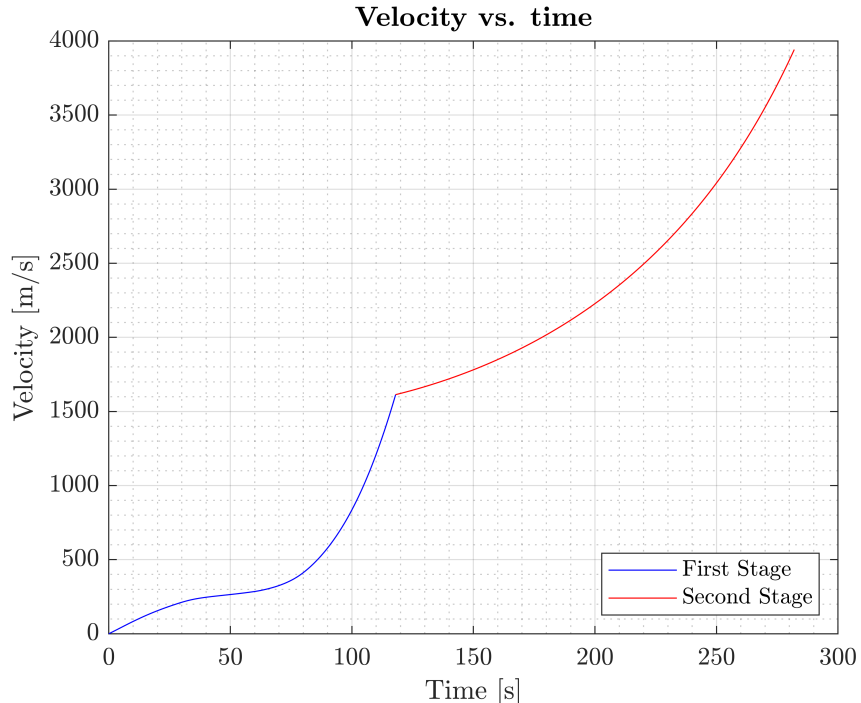


Figure 38: Velocity evolution vs time.

During the early stages of the ascent profile, the forces evolution and the dynamic pressure become two determinant factors which are advisable to study and take into account. During the first stage phase, despite having relatively low speeds, the rocket has not still reached high altitudes, therefore the product of velocity by density becomes larger and causes an area where the drag force effect and the dynamic pressure become really considerable. Hence, the spacecraft and all the launcher vehicle will have to be designed and manufactured considering these critical moments in which they are going to be subjected to the greater structural loads. According to this argument, the forces and the dynamic pressure evolution in front of time since the lift-off moment, are presented in the following figures.

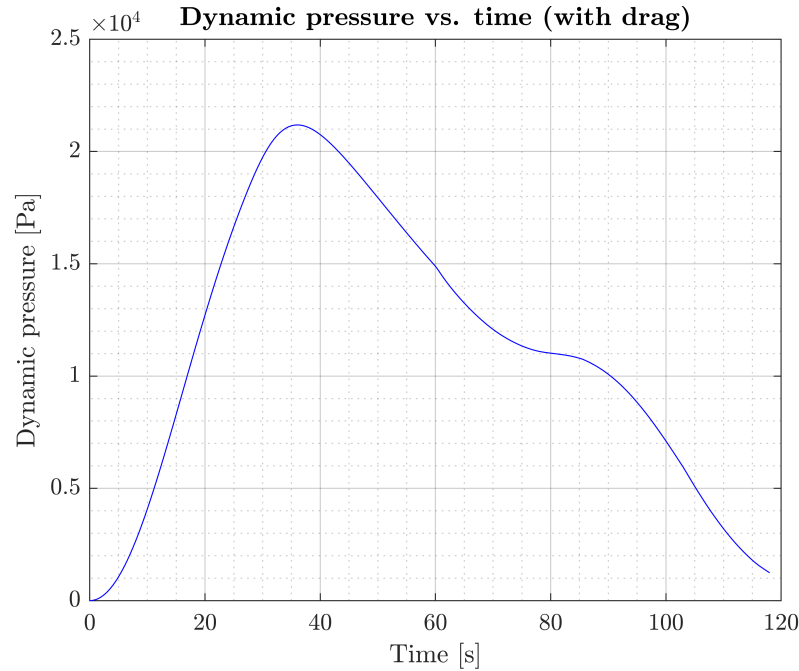


Figure 39: Dynamic pressure evolution during first stage launch phase.

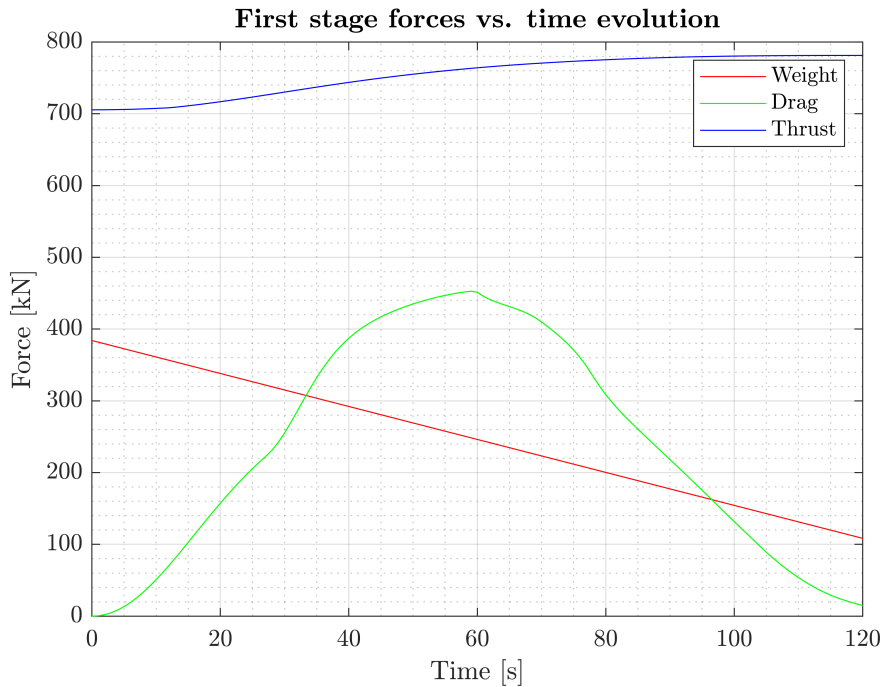


Figure 40: Forces evolution during first stage launch phase.

On the other hand, in order to complete and complement the information obtained with the simplified analysis of the ascent profile for the Soyuz launcher, taking the information from [51], the whole ascent profile regarding the altitude and the velocity variables, can be presented. Therefore, the following graphical representations would give us a more complex study results of the time evolution involved during the first flight of the spacecraft to the LEO orbit from which the interplanetary flight to the Halo L2 orbit will take place.

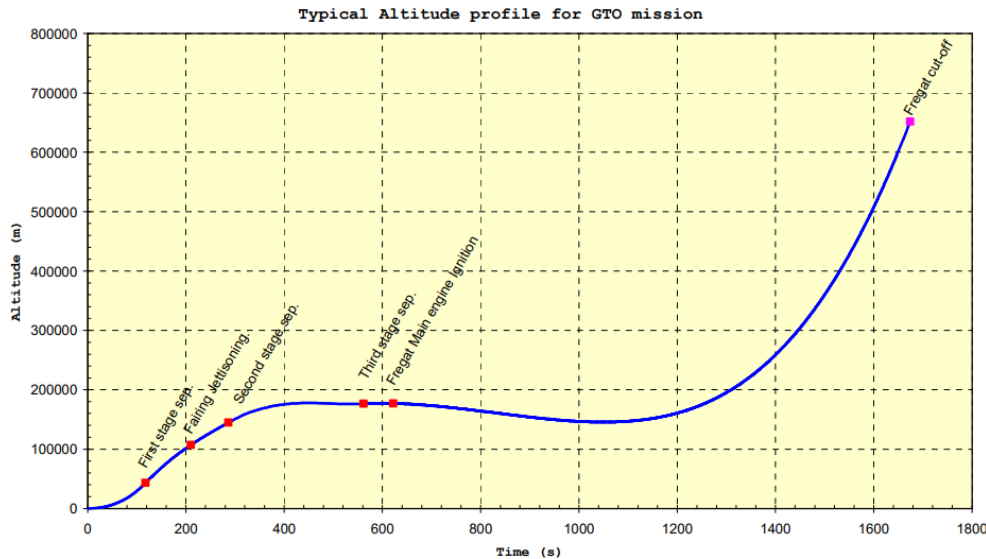


Figure 41: Altitude evolution during the all burning stages process. Source: [51]

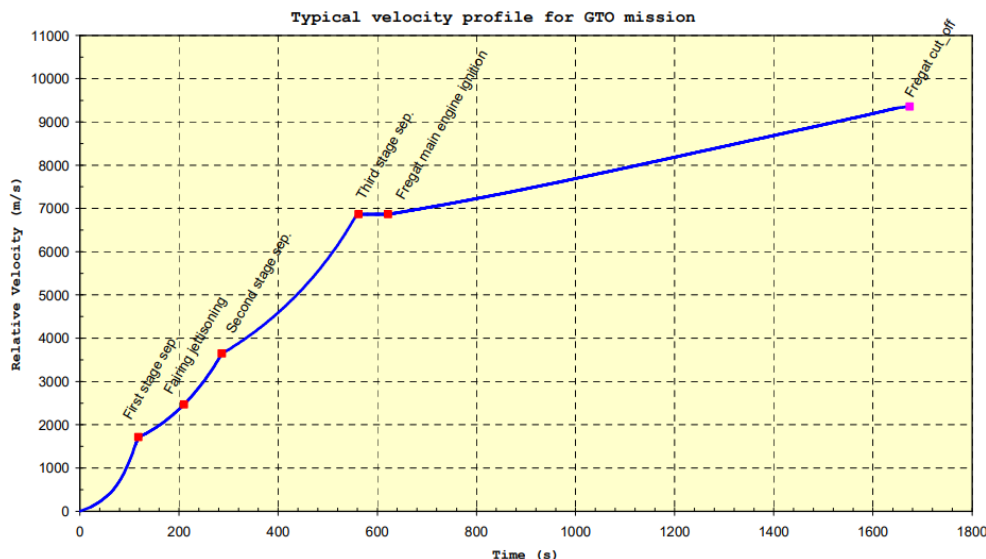


Figure 42: Velocity evolution during the all burning stages process. Source: [51]

As mentioned in the previous chapter, the height of the LEO parking orbit, that will be considered the initial point of the EXOHALO L2 mission interplanetary flight is 1000 km.

Consequently, as it can be appreciated in the figures above, ascent flight to this altitude would take more than 1800 seconds and the engines required for the interplanetary stage flight would be needed in order to achieve the LEO orbit estimated height.

4.2.1 Environment

In the matter of the launch environment, several phenomena will take place during the most critical stages of the flight ascent, involving some risks that could be disastrous for the payload if they are not taken into account during the spacecraft manufacturing process. Then following the information provided by the Soyuz User's manual [51], a briefly description of the environment that the spacecraft is intended to withstand is presented.

- **Accelerations:** During ground operations and flight, the spacecraft is subjected to static and dynamic loads. The 43 shows a typical longitudinal static acceleration evolution overtime for the launch vehicle during its ascent flight. As it can be appreciated the highest longitudinal acceleration occurs just before the first-stage cutoff and does not exceed 4.3 g.

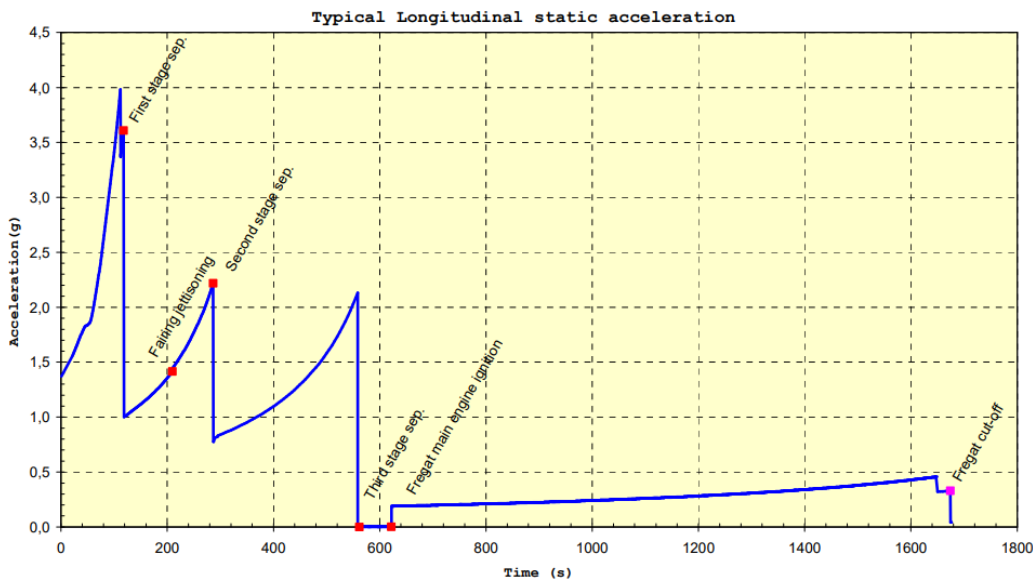


Figure 43: Longitudinal static acceleration evolution. Source: [51]

Moreover, the highest lateral static acceleration may be up to 0.4 g at maximum dynamic pressure and it is considering the effect of wind and gust attached to this phase.

- **Vibrations:** Due to a multiple factors, like the variable combustion flows, or the Pyrotechnic loads in separation devices, the launch vehicle and consequently the spacecraft where the payload is located will appreciate several vibrations that must be taken into account during the spacecraft design process.. These vibrations are classified in two different groups depending on the frequency range and the behaviour where they are used to work, and the payload must be able to support both of them. As regards the Soyuz launcher vibration generation, the most commonly appreciated vibrations during the launch phase are:

1. Sinusoidal Vibrations: They appear during the engine powered flight (mainly for the atmospheric flight stages), but also during some of the transient phases. Its typical duration is 6 min. Consequently as defined in [57], the limit sinusoidal vibrations that the spacecraft must be able to support and which will have to be demonstrated by testing the spacecraft are presented in the following table.

Sine direction	Frequency Range (Hz)	Vibration peak level (g)
Longitudinal	0-25	1.0
	25-45	1.0
	45-60	2.5
	60-110	1.25
	110-125	0.25
Lateral	0-25	1.0
	25-45	0.62
	45-60	1.87
	60-110	0.62
	110-125	0.25

Table 8: Sinusoidal limit vibrations for Soyuz auxiliary passengers. Source: [57]

2. Random Vibrations: These kind of vibrations are generated by propulsion system operation and by the adjacent structure's vibro-acoustic response. It is known that the Maximum excitation levels are obtained during the early stages of the ascent flight. Hence, in the figure 44 the limit levels of the acceleration power spectral density associated to these random vibrations appreciated by the spacecraft, for the Soyuz auxiliary passenger condition, during the first stage of the flight is presented.

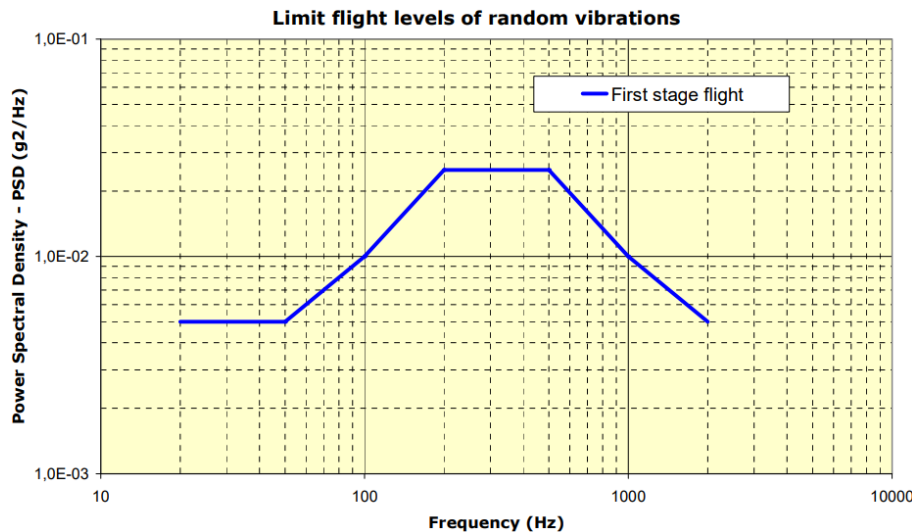


Figure 44: Random Vibrations acceptable levels during first stage of flight. Source: [57]

- **Acoustic Environment:** Related to the last phenomena presented, due to noise pressure acting on the spacecraft surfaces, additional random vibrations are generated. Therefore it is interesting to study the overall acoustic sound pressure level by considering the acoustic noise spectrum 45 to which the payload is subjected to, under the fairing protection factor that Soyuz launcher vehicle provides for auxiliary passengers.

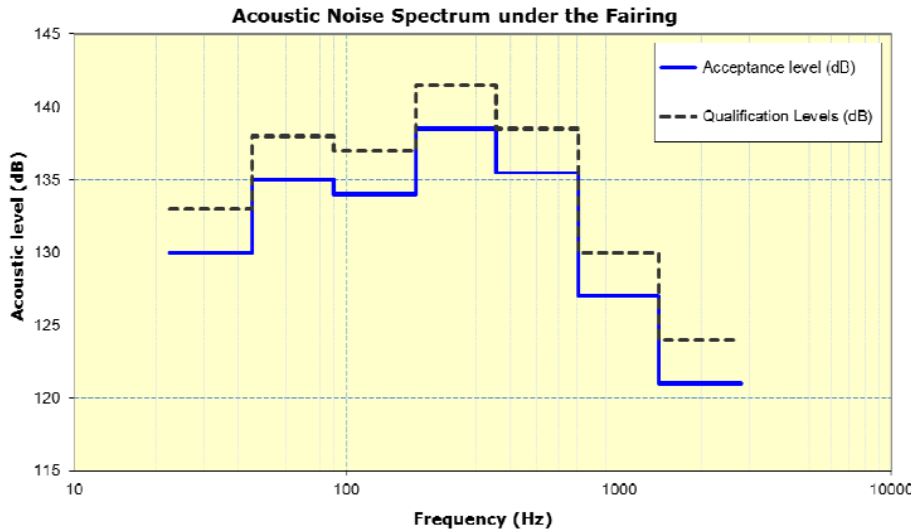


Figure 45: Acoustic noise spectrum under the Fairing. Source: [57]

Easily it can be appreciated the the highest flight limit level of acoustic pressure is given by a nearly value to 140 dB, more specifically 137.5 dB and this critical acoustic environment will be applied during a period of approximately 60 seconds: 15 seconds for lift-off phase and 45 seconds for atmospheric flight.

4.2.2 Payload protection

Trying to protect the spacecraft from the possible damage that it may suffer during the launch phase, two different protections mechanisms are used.

- **Fairing:** A fairing based on two half celled of carbon fiber reinforced by plastic (CFRP) with aluminum honeycomb core and a total thickness of 25 mm will be used to cover the payload. Additionally a 20mm thick thermal cover made of polyurethane foam with a protective liner is applied to the internal surface of the cylindrical part of the Fairing.

At the same time, the fairing allows to correctly define the usable volume for the payload. The payload usable volume is the area under the Fairing, available to locate the spacecraft. This volume marks the limits that the static dimensions of the spacecraft, including manufacturing tolerance, may not exceed. These usable volume is presented in the two following figures, where, as mentioned before, the mission payload is going to be located in the mini-satellite regarded emplacement.

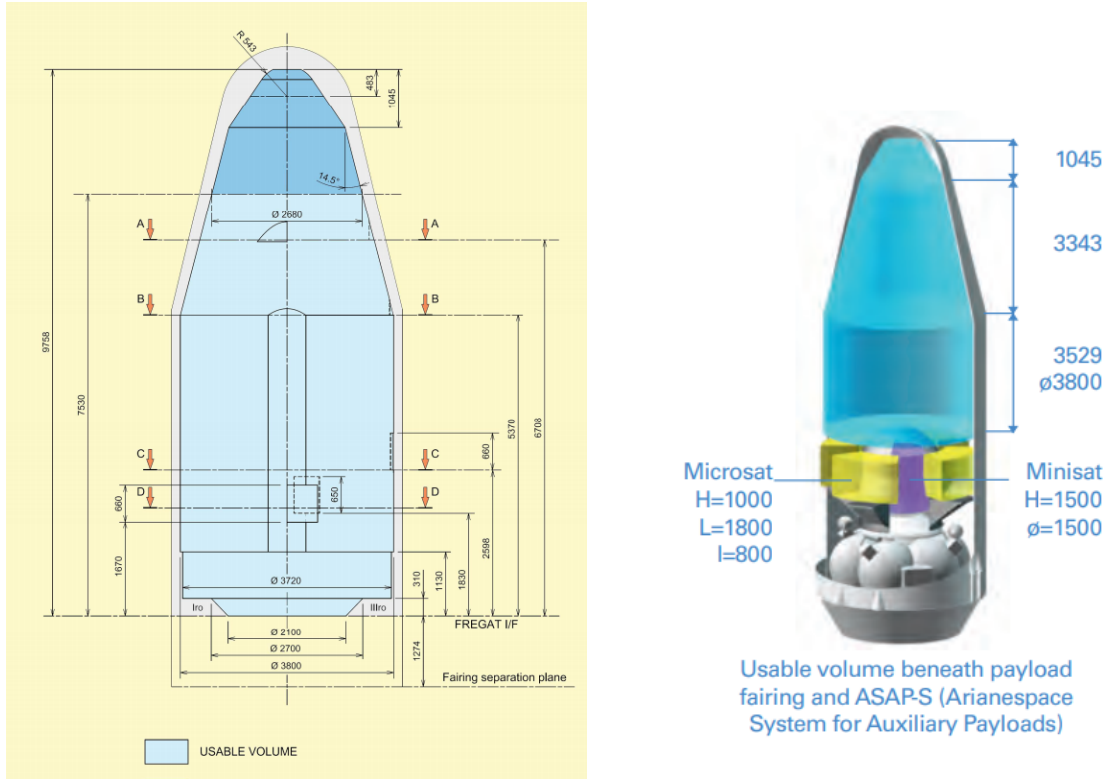


Figure 46: Soyuz total usable volume under the fairing.

- **Safety Factors:** The safety factors presented in the below table, will be applied during the different pre-flight tests in order to guarantee the integrity of the payload for take-off, when the launch environment most critical phenomena are applied to the spacecraft.

SC tests	Safety Factors	Tests duration
Static Accelerations	1.25	N/A
Sinusoidal Vibrations	1.25	0.5 oct/min
Random Vibrations	2.25	240 s
Acoustics	+3 dB	120 s

Table 9: Pre-flight required safety factors

4.2.3 Payload emplacement

As mentioned during the previous sections, for the payload emplacement, the piggyback option has been considered.

Due to our mission has been set as a low-budget mission, the piggyback option allows to reduce considerably the launch costs by sharing the Soyuz launcher with any other primary missions going to L2.

As presented in the figure 47, the Soyuz, allows two different piggyback configurations. The mini-satellite and the micro-satellite. For locating the payload of EXOHALO L2 mission, the

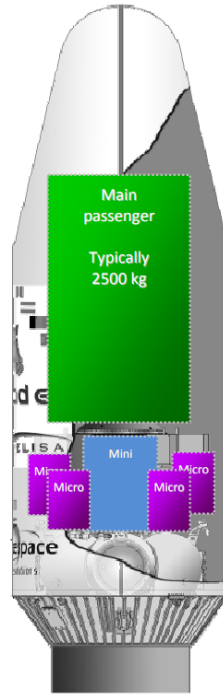


Figure 47: All possible payload configurations inside the Soyuz Spacecraft. Source: [57]

Regarding the launch vehicle adapter, the Soyuz ASAP's platform for auxiliary payloads allows multiple launch configurations thanks to the specialized adapted ring which allow to carry an auxiliary satellite with a maximum mass of 425 kg and a maximum height of 1841 mm. Additionally the payload from structure separation system allow to jettison the upper part ring and improve the maneuverability of the payload once the vehicle has reached its orbit objective.



(a) Specialized carrying structure for Soyuz ASAP-System. Source: [51]

(b) Auxiliary payload inside ASAP-S system vehicle adapter. Source: [57]

Figure 48: Soyuz ASAP-S vehicle adapter total configuration

4.3 Propulsion justification

4.3.1 Launcher's propulsion system

As regards the Soyuz's propulsion performance, a summary table with the most relevant data is added herebelow:

Criteria	Soyuz 2-1b Fregat			
Stage	1st	2nd	3rd	Fregat upper stage
Propellants	27 900 kg LOX 11260 kg Kerosene	63 800 kg LOX 26300 kg Kerosene	17 800 kg LOX 7600 kg Kerosene	6638 kg N ₂ O ₄ /UDMH
Engine	RD-107A	RD-108A	RD-0124	S5.92
Isp [s]	262 SL (319 vac.)	255 SL (319 vac.)	359 vac.	332 vac.
Attitude control				Pitch, yaw, roll: 50 N hydrazine thrusters

Table 10: Soyuz 2-1b Fregat propulsion performance. Source: data retrieved from [51]

4.3.2 Justification

Propellant type

In the matter of the propellant used, all Soyuz's stages make use of liquid bi-propellant as propulsion technology. In comparison with other options such as solid or hybrid propulsion, the liquid bi-propellant offers every possible feature needed to perform a complete flight. These capabilities are:

- Orbit insertion
- Orbit maintenance and maneuvering
- Attitude control

Specifically, the Fregat upper stage (Figure 49) uses N₂O₄/UDMH liquid bi-propellant, which is, in turn, a storable propellant. This category of fuel, in contrast with the cryogenic, offers the following advantages:

- Essential in interplanetary stages
- Liquid at room temperature
- No tank venting needed

Fuel budget

Once the launcher has reached the LEO parking orbit, the Fregat upper stage is the responsible for transferring the spacecraft to its L2 operational orbit. In order to assess the validity of the upper stage performance, the fuel budget must be analyzed.

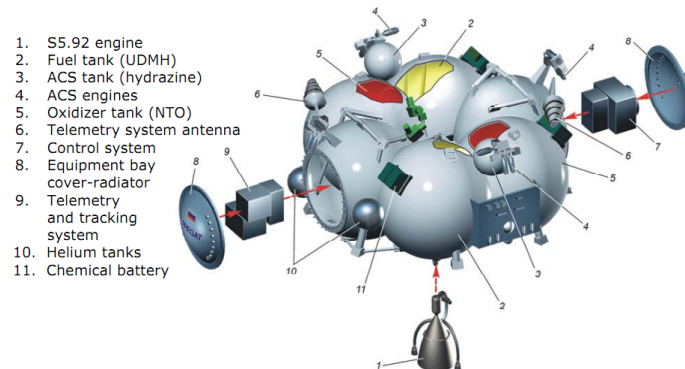


Figure 49: Fregat upper stage scheme.

The total propellant needed, according to [27], is defined by the following expression:

$$\text{Total propellant} = m_{\text{injection}} + m_{\text{attitude control \& residual}} + m_{\text{margin}} \quad (18)$$

From the orbital mechanics study in §3.2.2.2, it has been obtained that the needed fuel to complete the HT injection is:

$$m_{\text{injection}} = \Delta m_{\text{HT, min}} = 238.59 \text{ kg}$$

In addition, some amount of fuel is also needed for controlling the upper stage's attitude and residual aspects. Thereby, this quantity is given by the equation:

$$m_{\text{attitude control \& residual}} = 0.07m_{\text{injection}} = 16.70 \text{ kg}$$

Finally, a propellant safety margin is needed in case of unexpected emergencies. For this matter, the margin fuel is such that:

$$m_{\text{margin}} = 0.15m_{\text{injection}} = 35.79 \text{ kg}$$

Hence, the minimum total fuel budget to be loaded in the Fregat upper stage in order to complete the travel to an L2 orbit is:

$$\text{Total propellant} = 291.08 \text{ kg}$$

This just represents a mere 4.39% of Fregat's maximum fuel load (6638 kg), so it is clearly verified that the selected launcher fulfils the propulsive needs to reach the target L2 orbit.

5 Spacecraft definition

5.1 Payload selection and adequacy to the mission objective

The EXOHALO L2 payload comprises the cameras including focal planes and related electronics as well as the on-board data processing system. In this section all these components will be discussed.

5.1.1 Optical telescope assembly (OTA)

General layout

The instrument concept is based on a multi-telescope approach, involving a set of 4 wide-field cameras. This configuration breaks with the traditional mirrored-telescope one, which has been extensively used for decades. Indeed, the reason to use a multi-camera configuration is the possibility to cover wider fields of view (FoV). For example, mirrored-telescope satellites such as CHEOPS [24] or GAIA [58] have only FoV diameters of 0.4° and 1° , respectively, whereas TESS [59] and PLATO [17] reach values of 27° and 38° for each camera, respectively. However, Kepler [60] is an exception, achieving a diameter of 16° . Thus, a tendency towards greater sky coverage can be glimpsed. Then, according to the aforementioned reference data, a FoV diameter of 28° (slightly higher than TESS) has been selected, providing a resulting FoV of 625°^2 .

In this particular case, the dimensions of the mission are conditioned by the type of launching vehicle facility (§4.2.3). An orientative maximum mass of ~ 400 kg is the limit, and as CHEOPS and TESS have respective launch masses of 280 kg [13] and 325 kg [61], both can be taken as reference missions. The number of cameras has been actually chosen according to the latter one, and a model of the focal configuration, also based on TESS, is detailed in Figure 50.



Figure 50: Illustration of the four TESS cameras, lens hoods, and mounting platform. Source: [38]

Following the TESS model, as the current spacecraft design is for a small mission, the 4 cameras of EXOHALO L2 will be arranged so that no overlapping between their sky coverage is produced. Then a total FoV of 2500°^2 will be eventually achieved.

Lens assembly

The telescope optical unit is going to be characterised by the presence of several consecutive lens element, which refract the incident light and conduct it to the focal plane assembly (FPA), where the sensors can be found. The design of this element is going to be qualitatively done based on both TESS and PLATO configurations, represented in Figures 51a and 51b, respectively; and also complemented with the technical data provided by [17] and [59].

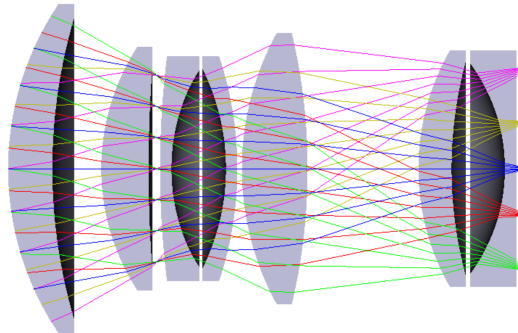
First of all, it is interesting to state that both configurations are constituted by seven optical elements. As regards TESS, they are mounted on two separated aluminium barrels fastened together, while in PLATO there only exists a single structure, consisting of a machined tube where the components are mounted. It is interesting to remark that in the latter spacecraft, the first optical element is not a lens, but a window that provides protection against radiation and thermal shocks. Then, it may be possible to implement in this window the 5 – 10 mm borosilicate glass protection suggested in §2.2.3. At the same time, and

due to the great number of optical elements required for the whole set of cameras, both space telescopes maximize the number of spherical lenses owing to its ease of manufacture.

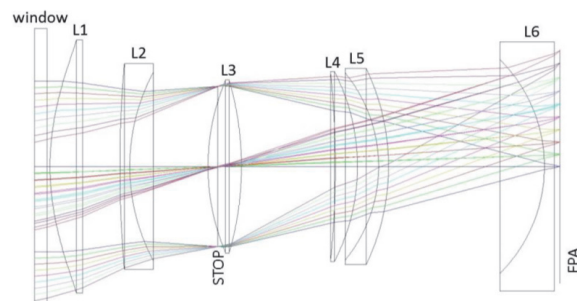
Another common feature involves light filters: in both TESS and PLATO (only applicable for its fast cameras), a wavelength filter coating is applied onto one of the optical elements, providing a cutoff at shorter wavelengths, close to the ultra-violet class in type of space telescopes.

Additionally, two details will be incorporated to the current design. The first one aims to reduce the vignetting effect, which consists of the reduction of an image's brightness or saturation toward the periphery compared to the image center. A solution applied to TESS encompasses the oversizing of the first lens element. This will minimize the geometric vignetting at large field angles, which is the case of the current telescope unit.

The second measure concerns the focus mechanisms, which TESS lacks. EXOHALO L2's cameras will follow the technique applied in PLATO: each telescope unit is going to be equipped with a passive radiator (see §5.2.1), but also with a heater, which will provide an active temperature control, and thus will allow to control the expansion of the lenses in order to achieve the desired focusing.



(a) TESS lens assembly. Source: [59]



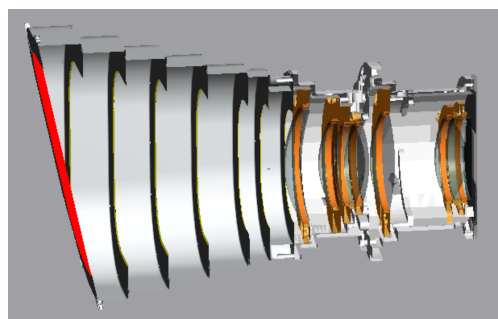
(b) PLATO lens assembly. Source: [17]

Figure 51: Cross-section showing the optical paths for light at a range of incident angles.

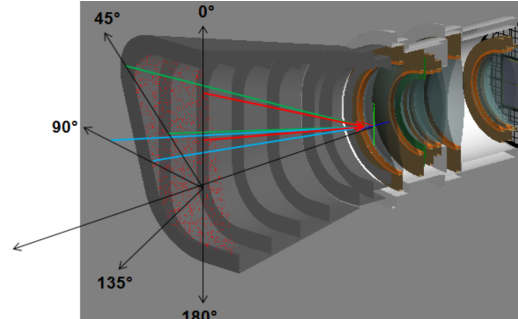
Lens hood

As it has been done for both TESS and PLATO, each camera is going to be equipped with a lens hood to minimize the levels of stray light from the Earth or Moon striking the detectors. However, there are several differences as regards its design. TESS' lens hoods are roughly conical in shape, with flattened sides to allow for clearance. In addition, these hoods are truncated just below the level of the spacecraft sun shade to prevent direct illumination by sunlight. As a result of this layout, two types of lens hoods may be defined in accordance to the required bevel angle.

Meanwhile, the second space telescope implements perfectly conical hoods as can be seen in Figure 17a. In this case the bevel is uniform for all the cameras, as also is their orientation. This second configuration will be followed in this design.



(a) Lenses and hood assembly.



(b) Representation of the level of scattered light suppression.

Figure 52: Cross-section of the cameras including the hood. Source: [59]

Furthermore, some remarkable design features of TESS' cameras will be studied. First, it is essential to consider that, despite the inclusion of the lens hood, the scattered light suppression performance will be dependent of the azimuth and incidence angle of the light rays. The cause is the azimuthal asymmetry owing to the short and long hood walls originated by the bevel.

Secondly, deep vanes in the inner part of the hood have been included to prevent the inner light reflection of the stray light that the hood is not able to cover.

5.1.2 Focal plane module (FPM)

The focal plane module is an intrinsic part of each camera. Located at the rear end of the elsn assembly, it encompasses the focal plane assembly and the front end electronics, as well as its supporting structure and related thermal equipment (for further details, see §5.2). This layout is common for mostly space telescopes, and for this particular distribution, PLATO [17] and CHEOPS [24] have been considered as references.

Focal plane assembly (FPA)

The focal plane assembly host the light sensors, which are the first component after the last lens of the telescope unit. The type of implemented sensors are going to be charge-coupled devices (CCDs), which are silicon light-detectors widely used in exoplanet observers, such as TESS [59], PLATO [17], CHEOPS [24] and GAIA [58]. Each camera will have a corresponding focal plane equipped with 4 CCD sensors.

More specifically, CCD270 sensors manufactured by e2v [62] have been selected. These are state of the art, thin-gate, back-illuminated sensors and that are going to be implemented in PLATO mission. Table 11 shows some of the most relevant specifications, and a great improvement can be observed image format when compared to the 1024×1024 , 2048×2048 and 512×512 present in CHEOPS, TESS and GAIA, respectively.

Parameter	Specification
Image format	4510×4510 pixels
Pixel size	$18 \times 18 \mu\text{m}^2$
Nominal operating temperature	-70°C (203 K)

Table 11: Specifications for the e2v CCD270. Source: [63] and [64]

Another aspect that will be analyzed is the quantum efficiency (QE), which can be defined as the ratio of the number of carriers collected by the solar cell over the number of photons of a given energy incident on the solar cell. In simpler words, it is a measure of the absorptivity of the incident light. The quantum efficiency is often given as a function of the wavelength, as it is shown in Figure 53. In this case, the maximum levels of absorptivity can be found between 500 and 700 nm. Then, it can be seen that the chosen sensors will be specially effective at measuring visible-light wavelengths close to infrared, as well as in the near-infrared margin.

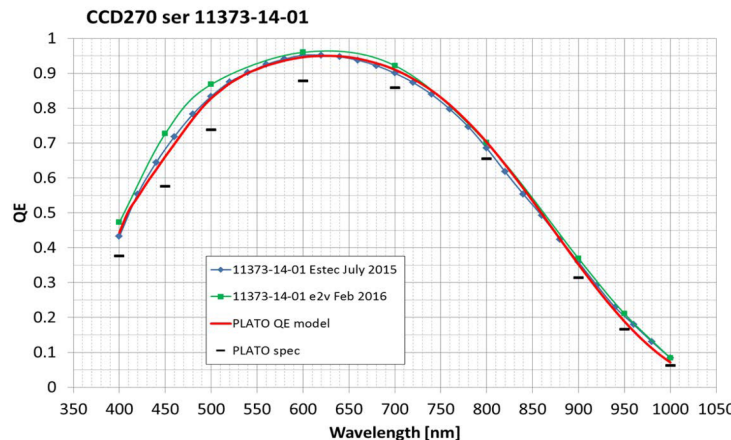


Figure 53: Measured quantum efficiency at -70°C for CCD270. Source: [63]

Additionally, this technology has been already studied and validated under laboratory conditions that simulate the real environment [63] [64] [65], which accounts for a technology readiness level (TRL) of 5 according to ISO 16290:2013 [66].

Front end electronics (FEE)

Consecutively following the focal plane assembly of each single camera, the front end electronics is going to act in essence as an analogical-digital converter (ADC). It is composed by the three boards suggested in [59] and described hereunder:

- **Driver board:** Provides operating voltages and clocks to the four CCDs in the camera.
- **Video board:** Amplifies and digitizes the outputs from the four CCDs.
- **Interference board:** Implements a field-programmable gate array (FPGA), which is the core of the FEE and orchestrates the acquisition of digitized video and housekeeping. At the same time, it commands the voltage and current regulator.

The acquired data is sent to the data processing subsystem (DPS).

5.1.3 Data processing subsystem (DPS)

The on-board data processing subsystem, also called back end electronics, can be subdivided in:

- Data processing unit (DPU): Implemented one for each camera, also includes a flash memory to store the processed data.
- Instrument control unit (ICU): The central computer of the space vehicle. It covers telecommunications and data flows, compresses the exchanged data, emits diagnostics of the current state and manages the other subsystems.

According to the optics information, and the comparison to the stored star catalogue, it is able to activate subsystems belonging to the service module (SVM) the attitude and orientation control subsystem (AOCS). Concurrently, it is also capable of triggering the power control unit (PCU), which can in turn regulate the heater's power supply.

Furthermore, two parallel ICUs are comprised for redundancy.

Figure 54 shows a block diagram of the electronics structure.

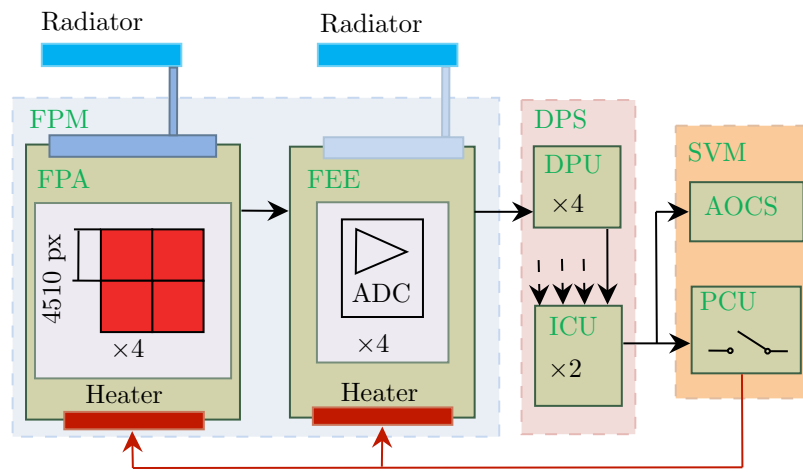


Figure 54: FPM, DPS and SVM block diagram.

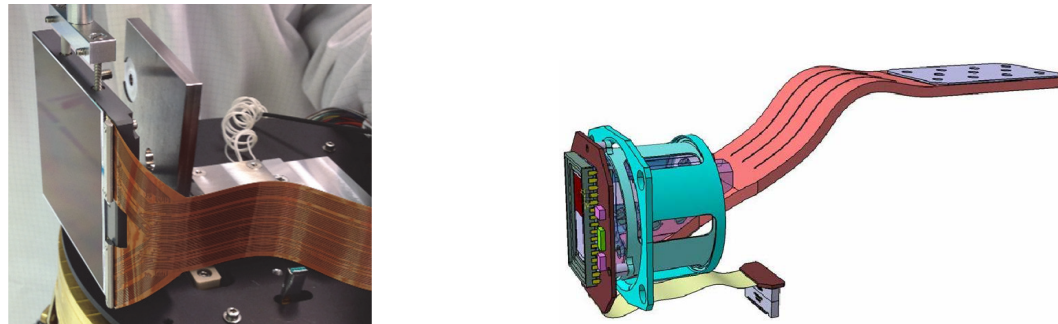
5.2 Thermal subsystem

5.2.1 Telescope optical unit

According to the CCD description developed in §5.1.2, it is essential to implement an effective cooling system in order to keep the sensors under the nominal performance temperature, which is -70°C . Thus,

it is necessary to provide a surrounding structure that acts as a “cold block”. Additionally, lower environmental temperatures will imply, in turn, lower signal noise. For this design, the reference configuration is going to be the one used at CHEOPS [24], detailed in Figure 55b.

The aforementioned structure will host the CCD sensors, part of the front end electronics, the radiator heat straps, and will allow at the same time mounting the thermal sensors. The thermal transfer is going to be achieved through copper straps as can be seen in Figure 55a. Copper, apart from being an excellent electric conductor, also has an excellent thermal conductivity, which makes it the most suitable material to manufacture these “heat wires”.



(a) CCD frame connected to the copper straps. Source: [17] (b) FPA practical implementation. Source: [24]

Figure 55: Illustrations of the copper straps connection and layout.

Nonetheless, all the extracted heat must be absorbed or irradiated somewhere else. Following the same approach applied for TESS [59], the lens hood is going to act as heat sink for the heat emitted by the sensors and front end electronics. At the same time, the hood is able to act a passive radiator. Then, the copper straps departing from the focal plane assembly structure will be attached to the inner part of the tubular structure of the telescope unit. Due to the close proximity between both, the length of the strap (and in consequence, its surface) will not be a problem concerning radiation emission.

In order to achieve a proper performance of this passive cooling system, it is essential that sunlight is not able to reach the hood at any time or orientation, otherwise there could be risk of the inversion of the heat flux, which would eventually lead to an overheating failure of the CCD sensors. With the aim to avoid that, the hoods must be beveled just below the level of the spacecraft sun shade, as was mentioned in §5.1.1.

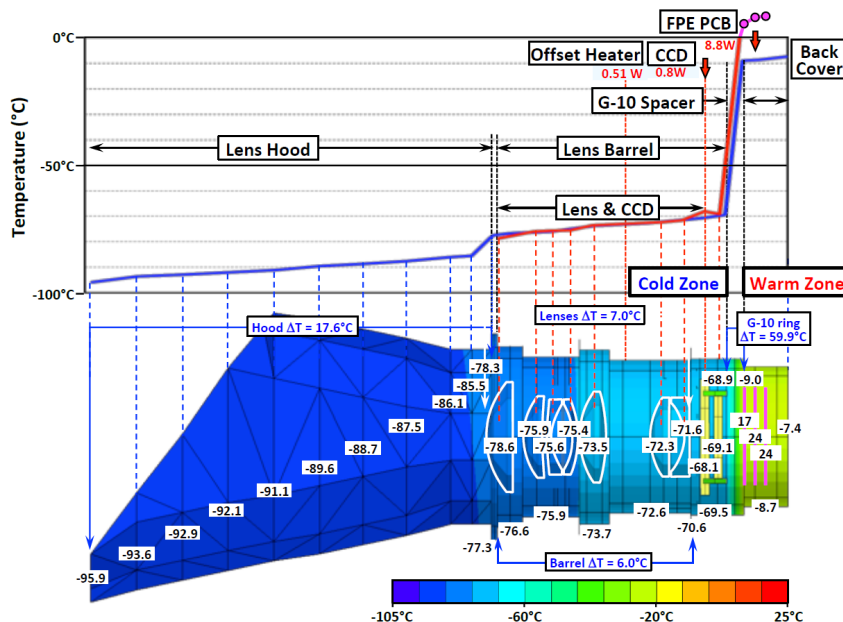


Figure 56: The predicted thermal profile of a TESS camera under flight conditions. Source: [59]

Figure 56 illustrates the thermal profile under nominal performance conditions for the TESS, a satellite of reference in this design. An additional aspect shall be discussed: the thermal insulation between the frontal “cold block” and the data processing units and further electronic components. Although the physical, direct connection that will exist through wiring, a thermal decoupling must be ensured. As a reference, TESS implemented G-10 fiberglass as an insulating material.

5.2.2 Solar shield

EXOHALO L2’s Halo orbit will place the satellite under constant sunlight. Thus, it is necessary to equip the space vehicle with an outer protection that ensures thermal isolation of the inner modules. More specifically, low solar absorptivities α_S and high infrared emissivites ε_{IR} are sought-after.

According to Table 7.2 of [67], the lowest absorptivity-to-emissivity ratio is achieved by optical solar reflectors (OSR). Despite metalized Teflon (FEP surfaces) may approach its properties, OSR has been being implemented in recent L2 missions, such as GAIA [58]. This last fact makes OSR the first insulation material to consider.

As a reference model, 10 mm-thick OSR [68] could be considered. They are manufactured by Qioptiq [69], company with wide experience in thermal space insulation systems, fact that would set the TRL for this product to the maximum level of 9 because it is an already existing and implemented technology.

More specifically, the chosen manufacturer allows to choose between different glass coverings and coatings in order to properly suit all the spacecraft derived requirements. As a reference information, the lowest $\alpha_S/\varepsilon_{IR}$ that could be achieved is around 0.072, lower than the 0.1 stated at [67]. In addition, OSR provide greater stability, this is, the variations between BOL and EOL conditions are less significant than for FEP. Nevertheless, these optimum insulation properties will translate into an increase of the cost, which in the end may to be traded off against its performance.

5.2.3 V-grooves

Eventually, a complementary radiation protection that could be implemented are the V-Grooves radiation shields. These have been implemented in Planck mission [70], and their use has been also proposed for ARIEL [19]. These passive cooling system is composed by adjacent shields made of Aluminium-alloy honeycomb. More specifically, their surface will have a very low emittance coating, with the exception of the upper one, which is exposed to the deep space and is coated to achieve high emissivity.

A total number of three V-Groove shields were used for Planck, and the same number has been suggested for ARIEL. If the figure is maintained, a TRL of 9 can be assumed for this component. Figure 57 shows how these system would be implemented. Identically to what was done for Planck, and what is intended to do for ARIEL, this protection is located immediately under the optical unit. It must be mentioned that the need that triggers the inclusion of this additional protection is the incessant solar radiation to what the space vehicle will be exposed by being in an orbit around L2.

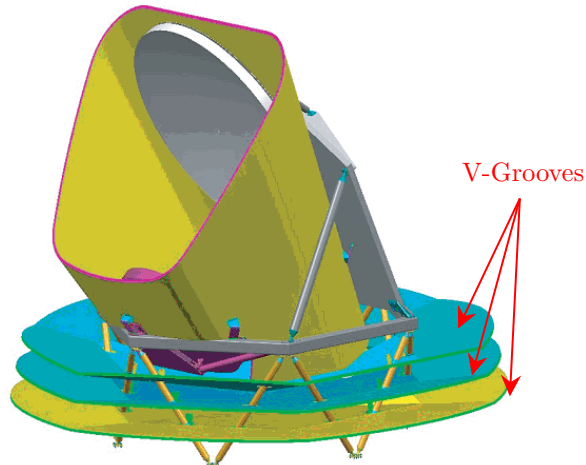


Figure 57: The Planck optical system, including the telescope baffle and V-grooves. Source: [70]

5.3 Power subsystem

5.3.1 Power consumption budget

It is always interesting to have the disaggregation of all the power consumption in order to localise the most power-demanding components, and thus focus the optimisation efforts on them. In the current case, due to the similarity in design and characteristics with CHEOPS [24] and the lack of further precise data, the payload power budget will be based on the aforementioned space vehicle. Table 12 shows the estimated numerical values for instrument unit, separated by its functions.

Function	Instrument unit	Nominal power [W]
Optics and data processing	FPA	4.2
	FPM auxiliary elements	3.0
	DPS	4.6
	Losses in power converters	0.7
Thermal control	FPA	3.9
	FEE	3.9
	OTA	28.8
	Total	59.3

Table 12: Payload power budget.

Additionally, some reference consumptions of the complementary subsystems can be obtained from [13]. These are included in Table 13. Nonetheless, the telemetry, tracking and command consumption has been obtained from the Herschel mission [71], which had a halo orbit around L2.

Subsystem	Nominal power [W]
Power distribution	9
Data handling system	22
AOCS	22
Telemetry, tracking and command	110
Total	163

Table 13: Subsystems power budget.

A resultant power budget of 222.3 W is obtained. It is interesting to see that this figure falls in the same order of magnitude than the power consumption of TESS, which is around 290 W, according to [61].

5.3.2 Power modes

According to ESA's ARIEL assessment report [19], the power budget can be separated into two mission modes:

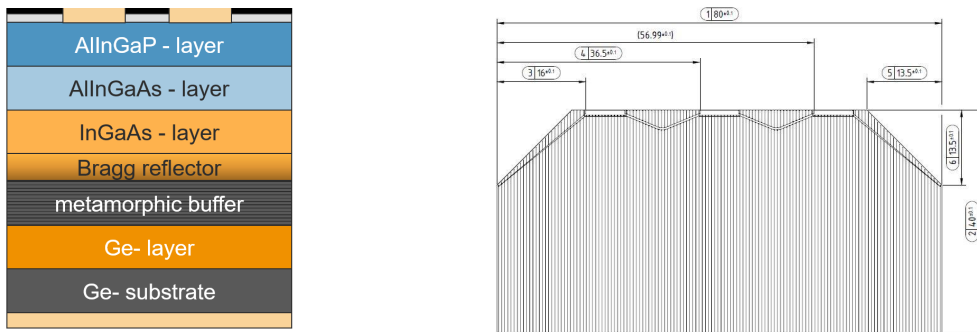
- **Commissioning and decontamination:** This mode occurs during the first months of the mission after launch. The service module is at its commissioning phase and the payload is kept warm in decontamination mode while the rest of the cryo-structure is left to passively cooling down until it reaches its operational temperatures.
- **Science and communications:** This is considered the nominal operation phase and it allows communication with ground stations apart from the collection of data.

The current mission will try to follow this conceptual structure, as its implementation in a medium-class mission such as ARIEL sets a reference to be followed in this case.

5.3.3 Solar cell technology

The implemented technology for the solar cells is going to be state-of-the-art multiple junction solar cells. More specifically, metamorphic 4-junction space solar cells developed and patented by Azur Space [72]

have been chosen as a reference model. This technology is promoted by ESA and is essentially aimed to NEOSAT programme [73]. Thus, this type of solar cell has been optimised for geostationary orbit. The difference of distance with respect to the Earth's surface may seem completely different, but the truth is that the aforementioned design's performance goal is to withstand the high-radiation environment of the Van Allen's Belts, and at the same time provide the maximum power efficiency [72]. This common harshness is what makes this model a reference for the current design.



(a) Schematic structure of the 4-junction solar cell 4G32-Advanced. Source: [74]

(b) Dimensions diagram of a single solar cell. Source: [75]

Figure 58: Illustrations of the copper straps connection and layout.

Figure 58a depicts how the cell cross-section is composed by a set of 4 subcells made from AlInGaP, AlInGaAs, InGaAs and Ge. The respective corresponding spectral quantum efficiencies (EQE) are plotted in Figure 59b. The fact that the ordinate value is kept approximately around a constant value is indicative of a balanced performance throughout the spectral bandwidth these cells are aimed to.

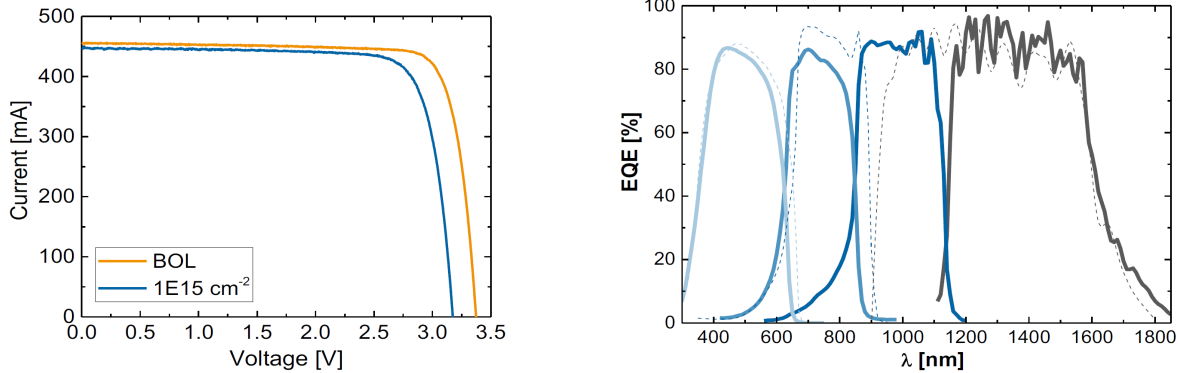
The thickness of the solar cell is also a decisive matter, as it is strongly linked to the weight. For the chosen model, a distributed Bragg reflector, aimed to reflect the high energy radiation is implemented to reduce the cell thickness and thus lower the minimally required diffusion lengths while maintaining the cell's optical thickness for light absorption [72]. The manufacturer's data states that the thickness has a nominal value of 110 μm , while the associated weight for a single cell is lower than < 1780 mg.

The following relevant aspect to analyze is the progressive degradation, which is measured considering the resultant ionizing particle fluency during the operation period. Therefore, the solar efficiency at ending-of-life (EOL) conditions will surely be lower when compared to beginning-of-life (BOL) ones. Table 14 is indicative of the aforementioned deterioration as a function of the ionizing particle (1 MeV) fluency per unit of surface.

	BOL	$5 \cdot 10^{14} \text{ [cm}^{-2}\text{]}$	$10^{15} \text{ [cm}^{-2}\text{]}$
Average efficiency η at 1367 W/m ² [%]	31.8	29.7	28.7

Table 14: Average efficiencies for different possible conditions along its operational life. Source: [75]

As the current computations are intended to gauge the power system of the space vehicle, the estimated efficiency at EOL conditions will be obtained considering an weighted average annual dose of particle fluency, obtained from data presented in Figure 16. An reference value of $2.27 \cdot 10^{11} \text{ cm}^{-2} \text{ year}^{-1}$ is obtained, and assuming a mission length of 4 years, the total dose would be close to 10^{-12} cm^{-2} , which implies that the solar efficiency would no be significantly compromised.



(a) Intensity-voltage characteristics of AZUR's 4G32C (1367 W/m^2) at BOL and at a 1 MeV fluency of 10^{15} cm^{-2} . Source: [72]

(b) External quantum efficiency of the four subcells of AZUR's 4G32C (solid) vs. the 3G30C (dashed). Source: [72]

Figure 59: Illustrations of the copper straps connection and layout.

In addition, Figure 59a illustrates the current-voltage response and has been included to visually demonstrate that the variation of performance conditions when exposed to more demanding environments would not be notorious. It shall be taken into account that the reference values provided by the manufacturer are prone to be found under GEO conditions.

Eventually, this new technology is also licit to be implemented into space missions. According to [73], 4G32C cell, as well as its auxiliary complements, are successfully qualified for GEO mission requirements according to ECSS standards. This would place the device in a technology readiness level of 8 for GEO missions. As the Lagrange L2 environment has been initially proved to be less harmful than the former one, a slightly lower or even equivalent category could be extrapolated.

5.3.4 Solar array sizing

The first step in order to size the solar arrays is to compute the solar irradiance at L2 point. This parameter is indicative of the solar power incident per unit of area:

$$I_{L2} = \frac{P_{\text{sun}}}{4\pi R_{L2}^2} = \frac{3.856 \cdot 10^{26}}{4\pi \cdot (1.511 \cdot 10^{11})^2} = 1343.9968 \approx 1344 \text{ W/m}^2$$

Where R_{L2} has already been defined in §3.2.2. Additionally, a uncertainty of $\pm 5 \text{ W/m}^2$ could be considered owing to the eccentricity of the Earth's orbit.

Then, the efficiency of the solar cells must be taken into account. Owing to the progressive degradation of the cells, the sizing must be done using EOL values, in order to ensure the proper power supply along the nominal mission period. In §5.3.3 it was stated that the radiation environment was not going to be harmful for the cells, as they had been designed to perform under the demanding conditions of the Van Allen's belts. Nevertheless, as the state of the panels cannot be consider to be identical to the BOL, the assumed efficiency will be the immediately posterior to the BOL one, as detailed in Table 14. Hence, $\eta_{EOL} = 29.7$ and the required power will be the detailed in §5.3.1 but increased in a 20 % safety margin, considering the possible degradation caused by the meteoroid environment.

$$A_{\text{ef}} = \frac{222.3 \cdot 1.2}{1344 \cdot 0.297} = 0.6683 \text{ m}^2 \approx 0.67 \text{ m}^2$$

This A_{ef} is the effective area, assuming that the solar arrays are placed totally normal to the Sun. Nonetheless, rotations around this normal reference should be consider. Figure 48b (see §4.2.2) establishes the maximum dimensions for the piggyback payload in the Soyuz launcher. The maximum assumable diameter for the Minisat is of $\phi_{\text{max}} = 1.5 \text{ m}$ considering auxiliary harness structure. Thus, the maximum diameter should be around $1.1 - 1.2 \text{ m}$. Considering inclinations up to 45° , the resulting diameter would be:

$$\phi_{\text{real}} = 2 \sqrt{\frac{A_{\text{ef}}}{\pi \cos(45)}} = 1.0970 \text{ m}$$

Leading to a resultant solar array surface $A_{\text{real}} = 0.9451 \text{ m}^2$. Figure 58b (see §5.3.3) depicts the dimensions of a solar cell, which can be assumed to be $80 \times 40 \text{ mm}^2$. As a reference, around 300 cells are going to be implemented within the array.

5.3.5 Batteries

The chosen Lissajous' (Halo) orbits bring significant benefits as regards power matters. These orbits have been detailed in §3.3.2, and owing to its large radius, the possibility of suffering eclipses by both the Moon and the Earth is minimal [76] [32].

Despite being the solar arrays the primary power source, a secondary power source is going to be required during the launch phase and until the deployment of the arrays [30]. *EXOHALO L2* is going to depart from a LEO orbit (see §3.2.2.1), similarly to the trajectory followed by GAIA [58]. According to this power requirement during ascent, it can be seen that batteries are the only feasible secondary power source, as the other alternative, the flywheel energy storage, cannot be operative during launch and ascent due to stability reasons.

In order to gauge the battery requirements, the reference consumption provided for Launch Mode in Table 16 at [24] will be used. A total figure of 61 W h is used during the 40 min that lasts the launch. This last fact is in accordance with [58], which suggested time is 60 min for the battery sizing. Assuming a required maximum output voltage of 28 V, it can be seen that the battery capacity shall be greater than 2.2 Ah.

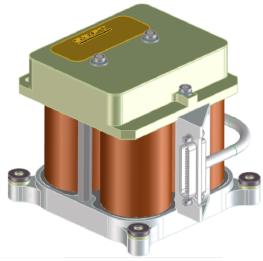
There are two main space batteries manufacturers in Europe: ABSL Space [77] and Saft [78]. Two models, one from each manufacturer, have been considered. Both implement the rechargeable Li-Ion technology, and despite their differences, both models should be taken into account for further stages on the design, where the power requirements are more precise. Table 15 shows an overview of the distinctive design parameters for each battery. In case of choosing the Saft model, the sizing calculation regarding the nameplate capacity should be repeated, bringing a new value of 4.1 Ah, still within the allowable range. It can be seen that the ABSL would provide a really wide margin of energy storage. Nonetheless, its weight is more than the double of its competitor.

Characteristic	Saft 4s1p VES16	ABSL 8s3p 28V
Nameplate capacity [Ah]	4.5	4.5
Voltage range [V]	13.2 – 16.4	20 – 33.6
Nominal energy [Ah]	64	129.6
Weight [kg]	0.7	1.6
Length × Width × Height [mm]	$90.5 \times 84.1 \times 77$	$176 \times 96 \times 98$
Technology readiness level	8 (minimum)	9

Table 15: Battery reference data. Source: [79] and [80]

As regards the TRL, the Saft battery holds an ECSS certification, while the ABSL's performance has been proved throughout real missions such as the CYGNSS [81].

As a preliminary conclusion, the Saft model should be chosen as weight is a very limiting factor, and this model fulfils the energy storage requirements whereas its weight is the lowest of both. Logically, it is also the most compact one. Nevertheless, as the power estimations are mainly based on CHEOPS mission [24], the possibility of unexpected variations in further stages of the power design does not allow discarding the ABSL model. Eventually, Figure 60 depicts both analysed models.



(a) Saft 4s1p VES16. Source: [79]



(b) ABSL 8s3p 28V. Source: [80]

Figure 60: Battery illustrations.

5.4 Attitude Determination and Control subsystem

The **Attitude Determination and Control subsystem** (ADCS) senses the orientation of the satellite observatory, maintains the satellite in a stable orbit, and provides the coarse pointing of the Observatory to the area on the sky that the Science Instruments want to observe (Line of Sight). In other words, this subsystem is responsible for acquiring the orientation of the spacecraft (Attitude), computing the orientation of the spacecraft (Determination) and guiding and orienting it (Control).

For instance, James Webb Telescope's attitude control subsystem is responsible for maintaining attitude and pointing, slew maneuvers, momentum unloading, ΔV (orbit correction) maneuver control, high gain antenna pointing, observatory safe modes, and ensuring that the observatory remains within Sun avoidance constraints [82].

In order to determine the satellites attitude, 3 pieces of information that relate the spacecraft to an inertial reference need to be measured. There measurement subsystem must provide accurate information with reasonable simplicity and this must be done in all phases of the satellite mission.

The ADCS requirements are split into two main pointing modes: a coarse pointing mode and a fine pointing mode [19]. Literature shows that separation of pointing modes applies not only to ARIEL spacecraft but also to Plato and Herschel as well.

- The **coarse pointing mode** is less precise than fine pointing mode. It is achieved by only using the ADCS units accommodated in the service module. This mode is mainly used to slew between target stars and its Absolute Performance Error is no major than 8° across the satellites Line of Sight. Consequently, this mode ensure that fine guidance sensor is capable of acquiring the target star within its field of view and then transition to fine pointing mode. The main errors that this mode encounters are the star tracker measurement noise, the ADCS control loop error and the alignment error between the stars and the fine guidance sensors field of view, this latter is biased by the materials thermo-elastic effects.
- The **fine pointing mode** is the precise pointing mode that will be used during observations of all science targets. It is achieved by means of the fine guiding sensors pointing knowledge at a 2 axes across the instrument's line of sight and an additional star tracker for attitude determination around the third roll axis. The Absolute Performance Error is no major than 1° . Moreover, auxiliary reaction wheels can supply all the guiding system as a sole actuator. To achieve this, the reaction wheels need to be operated in a narrow angular speed range, away from any peak vibration mode and away from any possible amplification frequency of the satellite's structure.

According to [82], James Webb Telescope uses multiple sensors such as sun sensors, star trackers, and gyroscopes to sense the satellite orientation and movement as well as reaction wheels or thrusters to control the observatory for different manoeuvres. EXOHALO L2 also employs similar technology for the requirements that apply to spacecraft telescope attitude control and measurement subsystem.

The overall attitude control and measurement architecture is presented in the figure below:

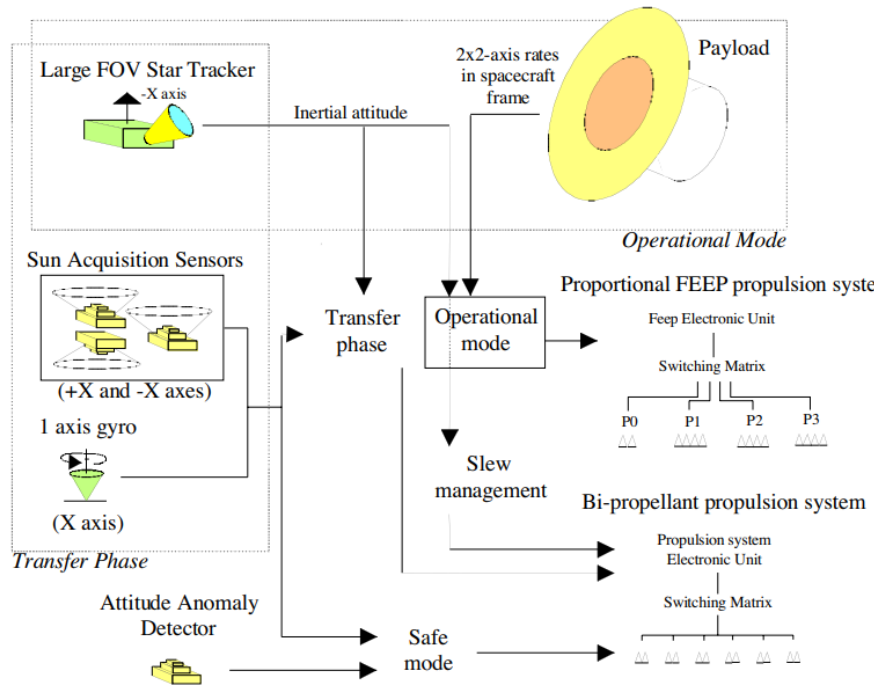


Figure 61: Architecture of the Attitude Determination and Control Subsystem (ACDS) and the Reaction Control Subsystem (RCS). Source: [58].

The elements of the atop figure is presented with further detail depending in which operational mode the satellite is undergoing:

- Acquisition mode:** Star sensor + Sun acquisition sensors + X-axis gyroscope + 3×8.9 N cold gas thrusters
- Transfer mode:** Sun acquisition sensors + X-axis gyroscope + 3×8.9 N cold gas thrusters + 400 N bi-propellant engine
- Transition mode:** Star sensor + Payload instrument sky-mappers + 13×8.9 N cold gas thrusters + FEEP thrusters
- Operational mode:** Star sensor + payload instrument sky-mappers + FEEP thrusters
- Slew mode:** Star sensor + 3×8.9 N cold gas thrusters
- Safe mode:** Attitude anomaly detector + Sun acquisition sensors + gyroscope + 3×8.9 N cold gas thrusters

The ACDS controls all orbit correction manoeuvres from launcher separation to injection into the final operational orbit around L2 [58]. It is possible to make some data acquisition towards the end of the transfer phase, when the Sun-spacecraft-Earth angle is sufficient to make communication with ground stations. Payload instruments are nominally switched off during transfer phase which means that they are inaccessible to be used. Thus, the ACDS will carry its own dedicated ACDS sensors, these subsystem sensors must ensure the following requirements:

- Those derived to meet spacecraft performance requirements.
- Those that come from data that is processed *a posteriori*.
- Those requirements that are linked to maintenance from operational phase.

Additionally, as mentioned before, the spacecraft's ACDS subsystem must be able to provide the necessary orbit maintenance manoeuvres during the operational phase.

During operational phase, the astrometric instruments are used to measure their displacement within the instrument field of view (this function known as sky mapper function). Consequently, the transition between the transfer phase (which employs dedicated ACDS sensors) and transfer phase (which uses astrometric instruments as attitude sensors) will be designed to utilise the latter ones at the end of the transition phase. This is mainly due to the fact that the main requirement of the dedicated ACDS sensors is to stabilise the spacecraft to its nominal state.

Moreover, sun sensors are kept on-board for safety reasons. However, the operational position can be now done using the star sensor. The spin stabilisation of the spacecraft during the transfer phase (which is the most robust design for the transfer phase) requires only standard Sun acquisition sensors completed with a simple 1-axis low-cost gyro on the spin axis.

Since the attitude pointing accuracy can be achieved with the star sensor, there is no need of using payload instruments except for rate measurements. Besides, noise can be filtered out by means of a Kalman filter between attitude information provided by the star sensor and rate information provided by the instrument.

5.4.1 Transfer phase propulsion system control

There is a wide variety of technologies, either being under development or available. The selection of the technology for attitude control is justified by the specific impulse (I_{sp}), which gives an indication of the efficiency of the thrust and is inversely proportional to the propellant mass required to realise a given acceleration.

Gaia mission [58] utilises a high thrust engine (400 N) together with a set of small thrusters (10 N). These engines ensure correct manoeuvres, ensure to minimise the time needed for the correction of those manoeuvres and simply using a single high thrust engine to the final injection to L2 orbit adds high complexity. Thereby, the high engine thrusters are used to surpass Van Allen belts and minimizing impact risks while smaller 10 N thrusters adjust final orbit insertion.

On the other hand, EXOHALO L2 mission is equipped with a cold gas thruster (see §5.4.5) to perform a series of attitude control manoeuvres with the aim of orienting the spacecraft.

Despite Gaia mission has a high thrust 400 N thruster to control great manoeuvres, EXOHALO can use either this technology or make use of reaction wheels. Nevertheless, according to [83], there is some variants from TWR and Daimler-Benz (models MRE 15 and CHT 400 with 86 N and 400 N respectively) that weights no more than 4 kg and can provide the 400 N for big manoeuvres.

5.4.2 Observation phase propulsion system control

During observation phase, a well suited solution is to use Field Emission Electric Propulsion (FEEP), this propulsion system has an extremely high specific impulse $I_{sp} = 6000$ s which leads to a global propellant budget of only 2.6 kg for a 6 year mission. Besides, it can also produce pure torque and forces in all directions. Thereby, orbit maintenance will be performed with the same set of FEEP thrusters as well as attitude and rate control. Part of the correction can be computed on-board using a solar pressure force estimator, the other part will be computed on-ground and sent to the spacecraft.

Additionally, one would ask how disturbance affect the spacecraft. Fortunately, disturbance torques which are induced by the Sun and the gravitational effects of nearby planets would only drift the satellite's trajectory with a rate of 3 m/s per year.

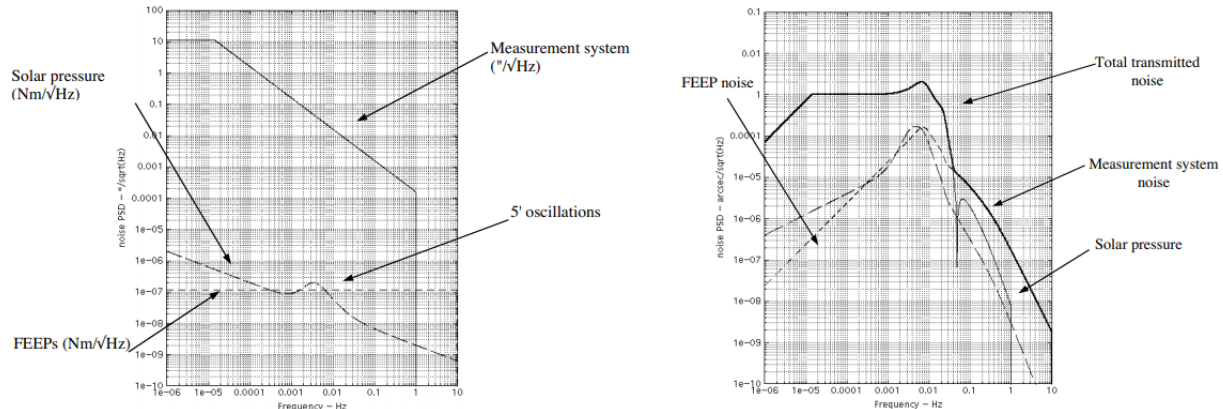


Figure 62: Results of the pointing stability analysis. Source: [58].

Notice Figure 62, in order to analyse the stability, a frequency based analysis was performed to identify the effects of a perturbing source. This was developed using simplified noise and control models. Since the noise is driven mostly by the solar pressure disturbances, one way to solve this issue is to increase the control bandwidth frequency. However, this results in an increased measurement noise into the instruments line-of-sight. Nonetheless, this problem is easier to solve as it only needs to adjust the center of gravity by decreasing the lever-arm. This can be done by a small inclination of the sun-shield.

5.4.3 Star sensors

EXOHALO L2's technology includes star trackers, reaction wheels sun acquisition sensors and propellers to control the attitude.

To begin with, it will carry a Galileo Avionica [71] star tracker [Figure 63]. This model has 16.4° field of view and weights only 3 kg. The STR sampled at twice the nominal frequency (4 Hz), measuring 9 stars at a time and combined the information for the two sets of measures to get greater positional accuracy.

Weight	3 kg
Power consumption	8.9-13.5 (20-50V)
Operating temperatures	-30/+60 C
Data interface	RS422, MIL-STD-1553
Field of view	16.4 x 16.4 degrees
CCD	512 x 512 pixels
Sun exclusion angle	
Accuracy	7 arc-seconds pitch, yaw 25 arc-seconds roll
Slew rate	0.5 deg/s full accuracy 2 deg/s reduced accuracy
Update rate	10 Hz
Acquisition time	< 6 seconds
Mission flown	Rosetta, Mars Express, Venus Express, Cassini, Stereo, Herschel, Planck etc



Figure 63: The Galileo Avionica star tracker used on Herschel and many other ESA missions and its principal characteristics). Source: [71].

Star sensors are the most accurate reference sensors for measuring attitude. The point of impact on the surface is determined using Charged Coupled Devices (CCDs), similar to the optical element in a video camera. Galileo Avionica uses a subset of Hipparcos catalogue as its input catalogue to consult the visible stars, this catalogue has over 3600 bright stars built in.

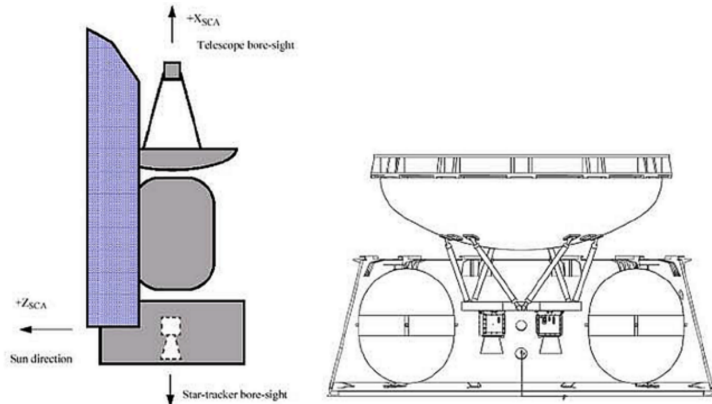


Figure 64: The Startracker and telescope. The Startrackers are shown as simple square black boxes with conical baffles in this schematic representation (from Herschel). Source: [71].

The Galileo Avionica startracker hardware includes:

- An objective lens.
- A baffle to protect the startracker from undesired straylight from the Sun and other bright sources.
- The focal plane assembly of CCD.
- The sensor electronics.

From a practical point of view, the startracker can be seen as a video camera plus an image processing unit that extracts the attitude's information from an image in the sky and then it determines its position with respect to a reference frame, in this case, the Earth-centered reference frame or (J2000). Eventually, the information is sent to a CPU which processes the data and send commands to the actuators for attitude control. Notice that the ACC also gathers data from instruments and payload.

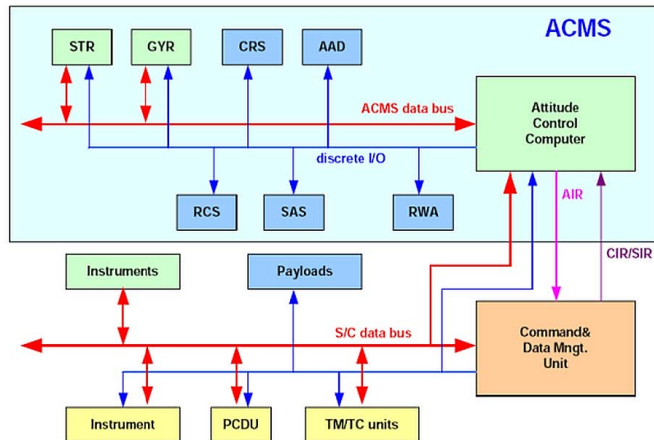


Figure 65: A schematic diagram of EXOHALO L2 avionics. Source: [71].

A simplified schematic of the avionics system is presented in Figure 65. ACMS stands for Attitude Control Measurement System which is equivalent to the ADCS mentioned before. This system has an Attitude Control Computer (ACC) that processes the data collected from the Startracker (STR) and (GYR) gyroscope and then sends control commands to the actuators. To complement the Startracker, Herschel was also fitted with Gyroscopes (GYR). The principle of gyroscopes is very simple: they are devices that use a rapidly spinning mass to sense and respond to changes in the inertial orientation of its spin axis. The STRs provided an absolute reference in the sky, but with limited accuracy. In contrast, the GYRs were very accurate, but only on short temporal and spatial scales.

5.4.4 Reaction wheels

As regarding the reaction wheels, these are a type of flywheel used to change the orientation of a spacecraft. The satellite needs constant changes in pointing antenna to either communicate with Earth or point to stars.

In order to explain its functioning, consider a satellite in space that needs to turn itself back to communicate with Earth. A reaction wheel is just a coupled system of rotating disks. Indeed, there is no air resistance in space so when a wheel rotates in one direction, the satellite will rotate in the opposite direction. This is basically Newton's Third Law of motion. Consequently, with wheels spinning in all three directions, the satellite can turn in any direction it aims. These wheels are fixed in place and spin between 1000 to 4000 rpm, building up angular momentum. To change the desired direction, the wheels spin in different velocities [84].

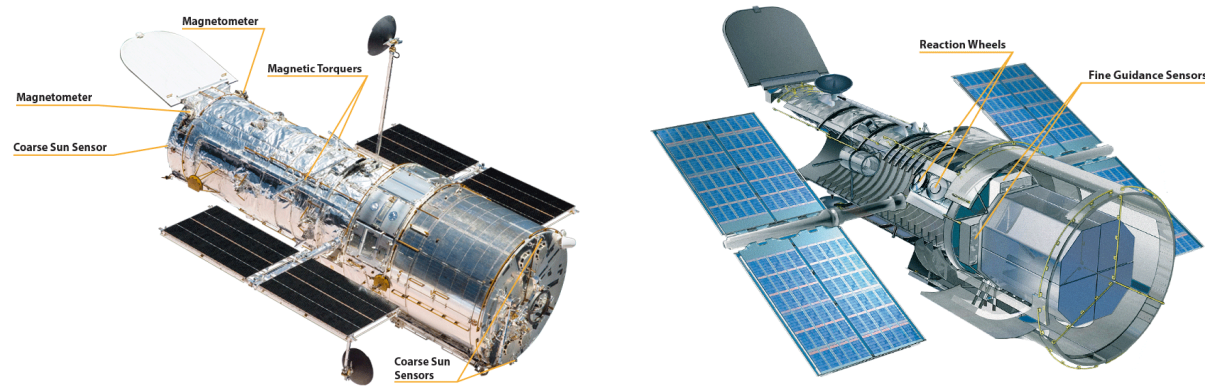


Figure 66: Cutaway diagram of the Hubble Space Telescope. Source: [84]

Eventually, EXOHALO L2 will employ 4 sets of Rockwell Collins Deutschland (Formerly Teldix) reaction wheels just as James Webb Telescope does. 3 of them are orthogonal and the latter is used for safety reasons. These wheels have heritage traceable to the Teldix wheels flown on NASA's Chandra, EOS Aqua and Aura Missions. These wheels have an angular momentum storage capacity spanning a range between 0.04 Nms and 68 Nms. And they accommodate the requirements of attitude control systems for spacecraft weighing between 30 kg and 7000 kg [85]. At first, it was considered using Honeywell reaction wheels [86], however this option was discarded, since the lifetime expectancy was lower (15 vs 5 years).

Some of the main features Rockwell Collins reaction wheels have are listed below:

- Power/loss torque optimized
- Hermetically sealed
- Modular configuration
- Includes space-qualified subsystems (rotor, motor, bearing unit and electronics)
- Offers a broad spectrum of different wheel types
- Thermal optimized
- More than 15 years of lifetime design

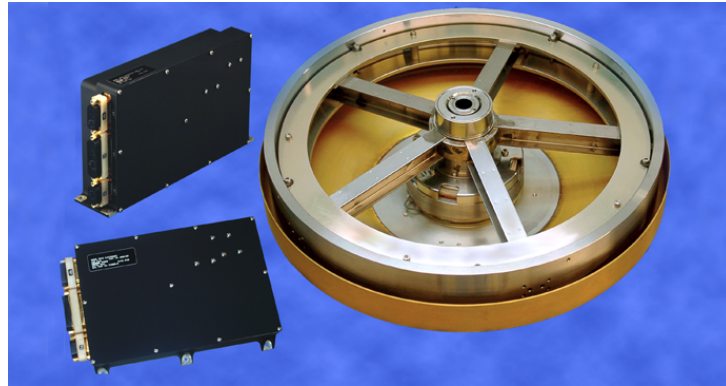


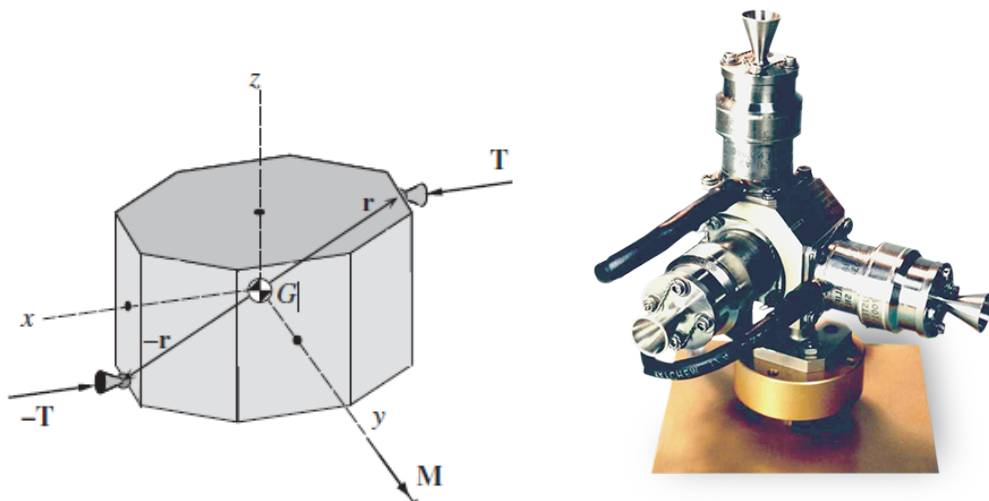
Figure 67: RDR 68 Reaction wheels from Collins Aerospace. Source: [85]

5.4.5 Cold gas thrusters

In order to perform attitude control maneuvers with the aim of reorientating the spacecraft, a cold gas thruster system is selected as the preferred option. These gas jets produce torque thus controlling the spacecraft's rotational motion, so a pair of thrusters must be implemented, one mounted on each side of the spacecraft and being their location the spacecraft's principal planes passing through its center of mass (refer to Figure 68a).

The main advantages of this external device is that it is capable of torquing about any axis, thereby suiting any possible orbit. Nevertheless, in comparison with other attitude control systems as reaction wheels or magnetic torquers, the gas jets have some drawbacks such as requiring fuel and the fact that the thrust is based on a switch on/off operation, in contrast with variable continuous thrust systems.

The selected model is the VACCO Cold Gas Thruster Triad (see Figure 68b). This device is characterised by being a 3-axis control thruster, with a thrust of 8.9 N and operating pressure of 1.8 MPa. This 3-axis thruster is capable of performing high pointing accuracy maneuvers in a fast way. Nonetheless, it is a complex system that requires a thrust vector and propellant control, apart from being a high weight subsystem. Despite these aspects, the cold gas thruster is chosen due to its high reliability, thus complementing the implemented reaction wheel's capabilities in terms of attitude control.



(a) Cold Gas Thruster forces diagram. Source: [87] (b) VACCO Cold Gas Thruster Triad. Source: [88]

Figure 68: Cold Gas thruster representations

5.4.6 Sun sensors

The Coarse Sun Sensors determine the orientation of the satellite in relation to the Sun. The sensors use silicon diode detectors to determine whether the Sun is present in their field of view and, if so, the angle of the Sun relative to the sensor.

Analogously to the star sensor this information is used to orientate the satellite according to the needs and protect the instruments against severe radiation or heat. Hubble telescope incorporated sun sensors, however, since it was designed to capture very low light stars and galaxies, the telescope was needed to be inclined 50° to prevent the sunlight from damaging the spacecraft. Additionally, the heat could cause expansion in the structure that holds the mirrors, interfering with the telescope's focus [84].

EXOHALO L2 also will be equipped with this technology. As a matter of fact, this sensor is highly precise (though less than star sensors) and its main advantage is that it has far more field of view ($\pm 130^\circ$).

Spacetech GMBH provides a solid solar sensor called CESS (Coarse Earth Sun Sensor), [89]

The key features of the CESS are:

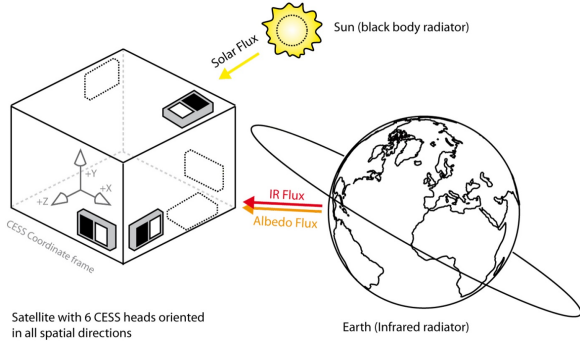
- Attitude information during de-spin and earth-oriented safe-mode
- Robust, lightweight, easy to accommodate
- Zero power consumption
- Excessive flight heritage



Figure 69: CESS Sun Sensor from Spacetech. Source: [89]

It's working principle is simple, 6 orthogonal CSS will be attached to determine the relative earth and sun vector in the following way:

1. First, it will perform a continuous measurement of the temperatures of all black and mirror reference surfaces.
2. Secondly, it will extrapolate the temperatures to a steady-state regime.
3. Thirdly, it will estimate the irradiated infra-red and solar flux, for both black and mirror OSR via their respective values for α and ε
4. Lastly, it will deduce IR (solar) flux imbalance for opposing CESS heads and construct earth-solar vector.



(a) CESS working principle illustration. Source: [89]

Performance	
Earth Vector Error (mean/max)	< 5° / < 15°
Sun Vector Error (mean/max)	< 3° / < 11°
Supported Spin Rate (max)	< 10 °/sec
Specifications	
Mass	80 g (for single unit)
Dimensions (LxWxH)	108 x 58 x 42 mm³
Electrical I/F	D-Sub 26 HD Connector

(b) CESS specifications. Source: [89]

Figure 70: CESS working principle and specifications. Source: [89]

5.5 Communication subsystem

The communication subsystem concept will be similar to James Webb Space Telescope, this communication subsystem architecture will provide two-way communications through all operational phases using S-band for command uplink and low-rate telemetry downlink, and Ka-band for high rate telemetry downlink [90].

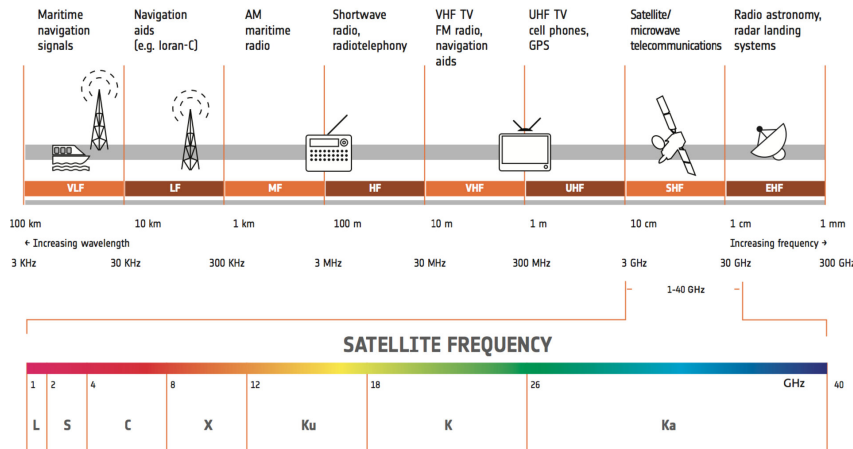


Figure 71: Satellite frequency nomenclature. Source: [91].

- S-band (2 – 4 GHz): This range of frequency is mostly used for communications satellites (especially of NASA communication with ISS) and surface ship radars. The S-band uplink frequency will be in the 2025 to 2110 MHz band, and the S-band downlink frequency will be in the 2200 to 2290 MHz band, allocated to Space Operations, Earth Exploration-Satellite, and Space Research. S-band frequencies are used for command uplink, low-rate telemetry downlink, and ranging.
- Ka-band (26–40 GHz): This range communications satellites, uplink in either the 27.5 GHz and 31 GHz bands, and high-resolution, close-range targeting radars on military aircraft. The Ka-band downlink frequency will be in the 25.5 to 27 GHz band allocated to Earth Exploration-Satellite. Ka-band frequencies are used for high rate downlink of science data and telemetry.

As the telescope will be located at a constant distance from Earth at approximately 1.5 M km away. It is feasible to have continuous communications with it as the Earth rotates through the Deep Space Network (DSN) since all communications are routed through NASA's DSN. The ground observatory can perform a series of commands for both pointing and observations.

Major components of the telecommunication subsystem include:

- **Antennas:** For transmitting and receiving commands.
- **Amplifiers:** For boosting the power of radio signals so that they are strong enough to be received at the Deep Space Network antennas.
- **Transponders:** For translating navigation and other signals from the orbiter.

5.5.1 Antennas

Let's consider the antennas that the spacecraft must include, regarding the different needs it is possible that a spacecraft is equipped with both high gain antennas and low gain antennas. The main difference between them is that a high-gain antenna is particularly good at transmitting signals in a narrow beam whereas a low-gain antenna tends to send its signal in a much wider sweep of directions. Thus, since the low gain antenna spreads its information in a much wider field of space, its intensity is lower and thereby, the signal received by a ground station is much weaker [92].

The reason why EXOHALO L2 will include both antennas is to secure that all information is transmitted. The main problem with high gain antennas resides in little disturbances in the direction pointing to Earth can lead to loss of communication. Low gain antennas does not suffer from this since the radio beam is spread much more broadly.

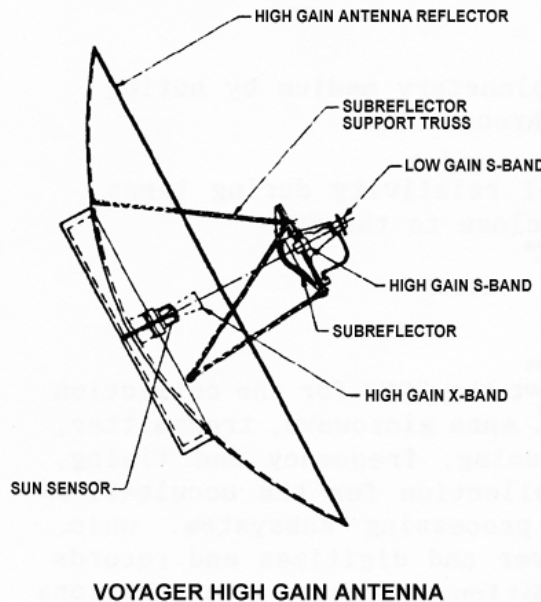


Figure 72: Voyager High Gain Antenna. Source: [93].

5.5.2 Amplifiers

Amplifiers are usually located on the back side of the high-gain antenna. Their main function is to boost the power of the spacecraft's radio signals so that they are strong enough to reach its destination receiver and able to be detected by the Deep Space Network antennas. Mars Reconnaissance mission's [92] criteria is to add an amplifier to each frequency band needed. Besides, they incorporate 3 amplifiers: two for X-band radio frequency (one for backup) and one for Ka-band.

The same criteria is used for EXOHALO L2, the spacecraft has 3 built-in amplifiers:

- **Two for S-band:** in order to improve ground station signals for commands (in case of emergency maneuvering). The additional amplifier is added for security reasons.
- **One for Ka-band:** This is capable of transmitting 25 W.

5.5.3 Transponders

A transmitter-receiver device works under the principle of amplifying and transmitting a range of frequencies (the transponder bandwidth) to another location/terminal/antenna on the earth. Usually, there can be many transponders on a typical satellite, each capable of supporting one or more communication channels. Satellite transponders can transmit directly to other satellites; this is known as *satellite mesh topologies*. Mars Reconnaissance Orbiter carries two transponders, special radio receiver/transmitters designed for long-range space communications. The second transponder is a backup just in case the first one fails [92].

Particularly, EXOHALO L2 also is equipped with transponders, the transponders main function The transponders have several functions:

- **Transmit and receive data:** The first thing the transponder does is to translate digital and electrical signals into radio signals and viceversa.
- **Transponding function:** The second function of the transponder.
- **Navigation function:** Finally, the transponder transmits several types of signals that provide critical navigation clues, enabling navigators on the ground to make precise calculations of the spacecraft speed and distance from Earth.

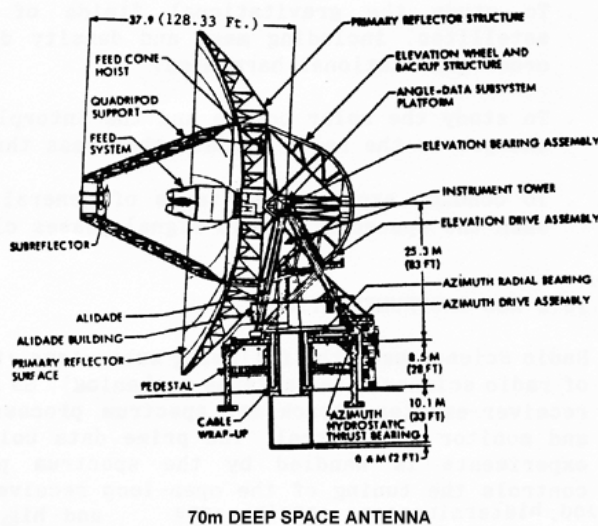


Figure 73: Deep Space Network Antenna. Source: [93].

During science operations, there will be constant nominal communication between ground station and the satellite, seven days per week. The largest part of it (> 3.5 hours) is dedicated to file-based science and stored housekeeping data transmission at 36 Mbps in K-band and real-time housekeeping data transmission at 26 kbps in S-band via a dual S/K-band high gain antenna. This means that 435 Gbits of science observation data is produced daily by the payload. Within this slot, a small window is used for communication setup and ranging and the 16 kbps uplink is ensured via S-band. Outside these nominal communication periods, a low-rate data link will be ensured via low gain antennas in S-band for minimum and contingent telemetry (2 kbps), telecommand (4 kbps). [94].

5.5.4 Ground segment

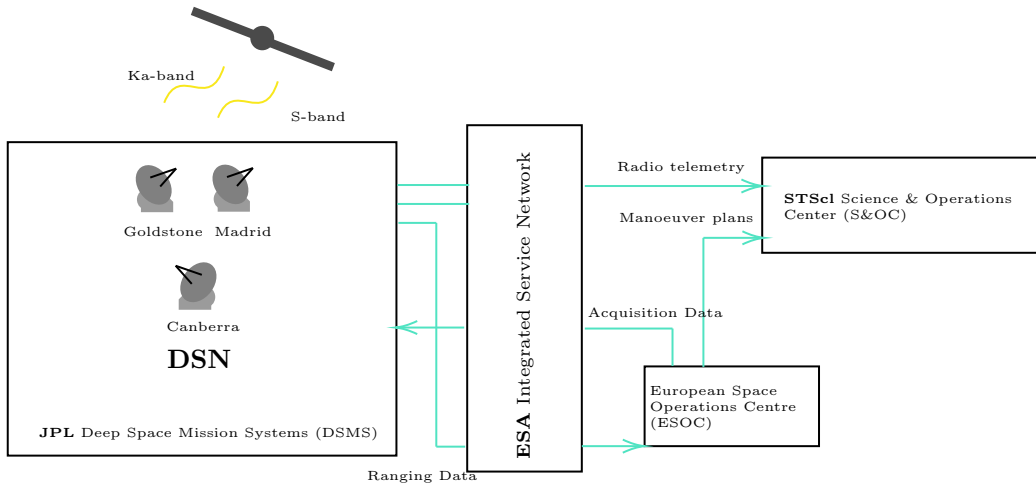


Figure 74: Ground station mission operation segment.

Finally, to sum up the ground station segment, mission operations are conducted through the JWST ground system shown in 74, which includes:

- **Deep Space Network (DSN):** The Deep Space Network is NASA's international array of giant radio antennas that supports interplanetary spacecraft missions, plus a few that orbit Earth. It also provides radar and radio astronomy observations that improve our understanding of the solar system and the larger universe.
- **ESA Integrated Services Network:** is a global system of communications transmission, switching, and terminal facilities that provides ESA with wide area network communications services.
- **European Space Operations Center (ESOC):** it operates spaceflight tracking and data acquisition networks, develops and maintains advanced space and Earth science data information systems.
- **Science and Operations Center (S&OC):** In which they control and calibrate the instruments to be pointed to study particular objects. In other words. The S&OC enables the planning and execution of scientific investigations.

EXOHALO L2's architecture has driven the design of the ground system's architecture. The spacecraft is designed to operate autonomously on orbit at the L2 for extended periods of time by incorporating event-driven, rather than time-driven and activity management. This level of autonomy will permit 5-day per week staffing of the S&OC for most operations (though the communications are constant) [95].

5.6 General layout

When studying the general configuration of previous space vehicles that have previously orbited L2, a tendency in their layout, specially as regards the localisation of their optics module, can be envisaged. The large radius of Lissajous (and Halo) orbits around the aforementioned point lead to a lack of eclipse time, which in turn translates into an incessant sun incidence. Despite this may have benefits from the power point of view, as no batteries will be required during the period of nominal operations, it drives the development of newer strategies to achieve a proper protection of the sunlight.

Figures 75, 76 and 77 allow a detailed view of the general configuration of the Herschel, Planck and ARIEL missions. The most remarkable common factor is that the payload module is placed in the three cases over a sunshield, which acts concurrently as a the support structure for the solar arrays. This is not a matter of coincidence and Figures 2, 5 and 6 (see §1), which depict artistic representations of GAIA, James Webb Space Telescope and PLATO, also share this component distribution.

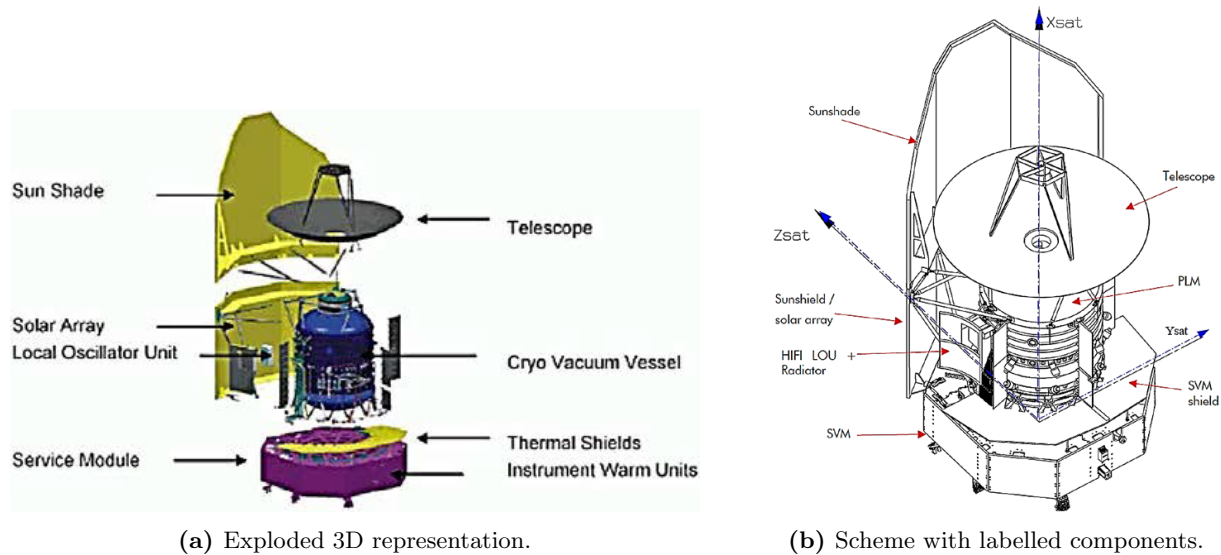


Figure 75: Herschel's general layout illustrations. Source: [71]

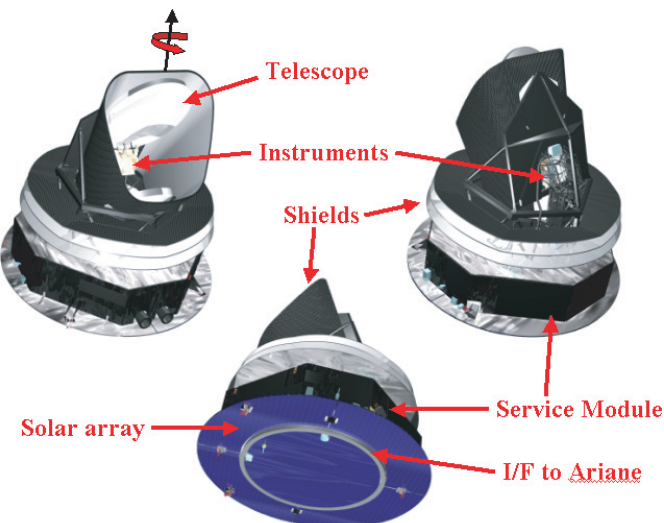


Figure 76: Planck's general layout illustration. Source: [70]

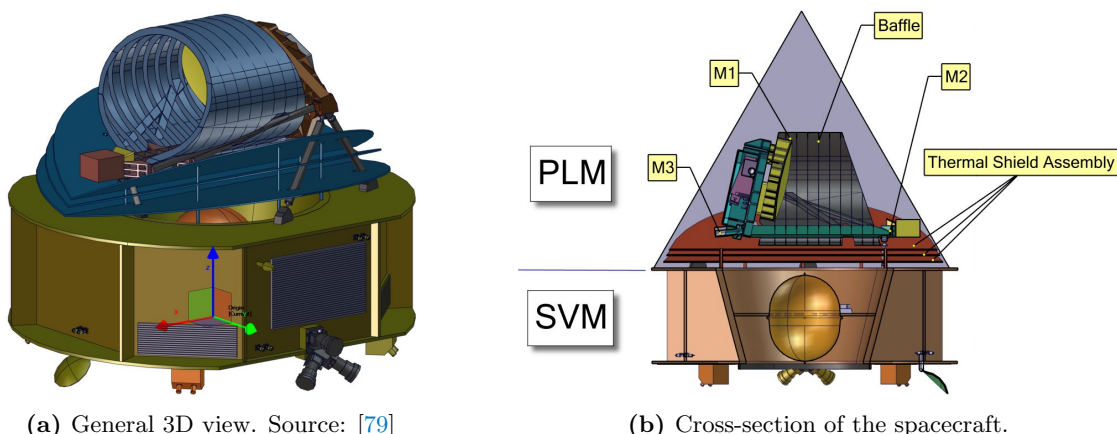


Figure 77: ARIEL's general layout illustrations. Source: [19]

Nevertheless, there exists a difference when it comes to the placement of the service module: ARIEL and Planck have it located immediately over the solar arrays, while Herschel leaves a lateral surface with direct contact with the Sun. This has the direct advantage that the maneuvering thrusters' exhaust flow is located further from the solar panels, and there thus exist less probability of propellant deposition on the cells.

For the computations performed in §5.3.4, a circular reference surface has been considered to allocate the solar array. Indeed, and according to the cylindrical shape of the fitting space at the piggyback of the Soyuz launcher (see §4.2.2), a close-cylindrical configuration would be the optimal from the holding point of view. In addition, the lack of extensible solar panels would reduce the constructive complexity, and at the same time would lead to a more compact structure, with lower inertia, and thus greater easiness to control the attitude.

Then, the position of the 4 cameras would be locating upwards, at the upper surface of the cylinder. According to [17], the length of each camera's lens assembly is around 30 cm, which implies that the axis-longitudinal placement is going to be the most optimum one in terms of dimensions. A vertical height of 0.8 – 0.9 m could be expected, then.

6 Conclusions

EXOHALO L2 will be the third small-size mission within the Cosmic Vision ESA programme. The technical design carried out in this report aims to provide a new space observation platform which will follow essentially CHEOPS' tasks in exoplanet localisation.

Lagrange L2 has been selected as the optimum location due to its intrinsic gravitational stability, as well as its free-eclipse advantage. This will allow to achieve larger observation periods. Thus, a Halo orbit around such point has been chosen owing to the provided continuous and uninterrupted view of the mission subject.

This placement involves subtle advantages as regards its space weather phenomenology. The presence of plasma will lead to spacecraft charging, but methods to ensure the protection of the inner electronics have already been suggested in §2.1.3. As regards radiation, the conditions in the Van Allen's belts' are more demanding than in the current case. Thus, technology designed for the aforementioned conditions can be also applied in this design, bringing high TRL with implicit extra safety margins.

In the matter of the orbital mechanics, a Hohmann transfer has been used in order to reach the L2 destination basically due to its high efficiency and the low fuel cost associated. In this line, an optimisation of the required fuel mass has been achieved by selecting a high height LEO parking orbit and only loading the minimum required propellant on the Fregat upper stage.

Regarding the launcher selection, due to ESA's partnership with ArianeSpace, one of its 3 main launch vehicles has been selected. Therefore, the Soyuz, Ariane 5 and Ariane 6 performance capabilities have been studied and compared. Consequently, Soyuz has been chosen due to its best payload accommodation option with the piggyback configuration, thus enabling a high reduction of the launch costs, and also due to its reliability, which is the highest with a 98.4 %.

Concerning power sources, solar arrays are going to provide the nominal power due to the lack of eclipse, while batteries are only aimed to be used during the first launch phase. Regarding the attitude determination and control subsystem, the spacecraft is equipped with several instruments that not only ensures the safeness of the instruments as well as maintaining a constant dual communication with Earth. Eventually, advanced passive cooling systems have been implemented. ORS will keep the spacecraft thermally insulated, while copper straps will serve as heat extractors for the optic sensors and electronics. In addition, V-Grooves could be a complementary shield to be considered.

This report has covered separately the main aspects of the mission, starting from the orbit and launch, until the subsystems definition. Nonetheless, a clearer definition of the system requirements and a more detailed study of the junction and interrelation of all the aforementioned aspects would be necessary in order to move forward to the Preliminary Definition Review, following the Space Mission Analysis and Design procedure suggested in the ECSS [26].

References

- [1] NASA - Kristen Walbolt. (2020). *How many exoplanets are there?* <https://exoplanets.nasa.gov/faq/6/how-many-exoplanets-are-there/>
- [2] European Space Agency. (2018a). *Exoplanet mission timeline.* <https://sci.esa.int/web/exoplanets/-/60649-exoplanet-mission-timeline>
- [3] National Aeronautics and Space Agency. (2020). *Exoplanet Exploration: Planets Beyond Our Solar System.* <https://exoplanets.nasa.gov/discovery/missions/#first-planetary-disk-observed>
- [4] NASA, Michelle Johnson. (2018). *Kepler and K2.* https://www.nasa.gov/mission_pages/kepler/overview/index.html
- [5] ESA Earth Observation Portal. (2021). *ESA Earth Observation Portal - Gaia Astrometry Mission.* <https://directory.eoportal.org/web/eoportal/satellite-missions/g/gaia>
- [6] European Space Agency. (2020a). *Gaia operations.* http://www.esa.int/Enabling_Support/Operations/Gaia_operations
- [7] European Space Agency. (2019). *Detecting exoplanets with astrometry.* <https://sci.esa.int/web/gaia/-/58788-detecting-exoplanets-with-astrometry>
- [8] Perryman, M. et al. (2020). *Astrometric exoplanet detection with Gaia.* <https://arxiv.org/abs/1411.1173>
- [9] Phillips, D. (2020). *Gaia.* <https://solarsystem.nasa.gov/missions/gaia/in-depth/>
- [10] MIT. (2020). *Mission overview - TESS - Transiting Exoplanet Survey Satellite.* <https://tess.mit.edu/science/>
- [11] Walbolt, K. (NASA). (2020). *Transiting Exoplanet Survey Satellite (TESS).* <https://exoplanets.nasa.gov/tess/>
- [12] Garner, R. (2020). *TESS Exoplanet Mission.* <https://www.nasa.gov/tess-transiting-exoplanet-survey-satellite>
- [13] European Space Agency. (2020b). *CHEOPS.* https://www.esa.int/Science_Exploration/Space_Science/Cheops (accessed: 26/12/2020)
- [14] Jenner, L. (2020). *NASA's Webb Will Seek Atmospheres around Potentially Habitable Exoplanets.* <https://www.nasa.gov/feature/goddard/2020/nasa-s-webb-will-seek-atmospheres-around-potentially-habitable-exoplanets>
- [15] European Space Agency. (2018b). *Nueva fecha de lanzamiento para el telescopio espacial James Webb.* https://www.esa.int/Space_in_Member_States/Spain/Nueva_fecha_de_lanzamiento_para_el_telescopio_espacial_James_Webb
- [16] Bauer, M. (2018). *Construction of Europe's exoplanet hunter PLATO begins.*
- [17] ESA. (2017a). *PLATO Definition Study Report* (tech. rep.). ESA. https://sci.esa.int/documents/33240/36096/1567260308850-PLATO_Definition_Stud..._Report_1_2.pdf
- [18] ESA/ATG medialab. (2019). *Artist's impression of PLATO.* <https://sci.esa.int/web/plato/-/artist-s-impression-of-plato-1>
- [19] ESA. (2020a). *ARIEL assessment report.* https://sci.esa.int/documents/34375/36249/1567260310680-ESA_SCI-2017-2_ARIEL.pdf
- [20] European Space Agency. (2020c). *ESA's exoplanet mission Ariel.* <https://arielmission.space/>
- [21] NASA Exoplanet Exploration. (2020). *5 ways to find a planet.* <https://exoplanets.nasa.gov/alien-worlds/ways-to-find-a-planet/#>
- [22] Caleb, H. (2020). *European Commission agrees to reduced space budget.* <https://spacenews.com/european-commission-agrees-to-reduced-space-budget/>
- [23] Masetti, B. (2013). *Why infrared? (exoplanet edition).* <https://asd.gsfc.nasa.gov/blueshift/index.php/2013/10/24/maggies-blog-why-infrared-exoplanet-edition/>
- [24] Benz, W. et al. (2013). *The CHEOPS mission* (tech. rep.). ESA. https://sci.esa.int/documents/34375/36249/1567259940843-CHEOPS_EST_SCI_RP_001_RedBook_i1.0.pdf

- [25] Mousis, O., Deleuil, M., Aguichine, A., Marcq, E., Naar, J., Aguirre, L. A., Brugger, B., & Gonçalves, T. (2020). Irradiated ocean planets bridge super-Earth and sub-Neptune populations. <https://doi.org/10.3847/2041-8213/ab9530>
- [26] ESA. (2009). *ECSS-M-ST-10C Rev.1 – Project planning and implementation*. <https://ecss.nl/standard/ecss-m-st-10c-rev-1-project-planning-and-implementation/>
- [27] Larson, W. J., Wertz, J. R., Kirkpatrick, D., & Klungle, D. (1999). *Space Mission Analysis and Design* (Third edit). El Segundo, California, Microcosm Press; Kluwer Academic Publishers.
- [28] ESA. (2020b). *ESTRACK ground stations*. https://www.esa.int/Enabling_Support/Operations/ESA_Ground_Stations/Estrack_ground_stations
- [29] ESA. (2020c). *Gaia Mission operations*. <https://www.cosmos.esa.int/web/gaia/mission-operations-esoc>
- [30] ESA. (2017b). *ARIEL Definition Study Report* (tech. rep.). ESA. https://sci.esa.int/documents/34375/36249/1567260310680-ESA_SCI-2017-2_ARIEL.pdf
- [31] European Space Agency. (2020d). *Estrack ground stations*. https://www.esa.int/Enabling_Support/Operations/ESA_Ground_Stations/Estrack_ground_stations
- [32] Evans, S. W. (2003). *Natural environment near the Sun/Earth-Moon L2 libration point* (tech. rep.). Marshall Space Flight Center. <http://www.dept.aoe.vt.edu/~cdhall/courses/aoe4065/OtherPubs/SPECS/L2environment.pdf>
- [33] Minow, J., Blackwell, W., & Diekmann, A. (2004). Plasma Environment and Models for L2. In *42nd AIAA Aerospace Sciences Meeting and Exhibit*. <https://doi.org/10.2514/6.2004-1079>
- [34] Garrett, H. B., & Whittlesey, A. C. (2012). *Guide to mitigating spacecraft charging effects*. John Wiley & Sons.
- [35] Minow, J. I., Jr., W. C. B., Neergaard, L. F., Evans, S. W., Hardage, D. M., & Owens, J. K. (2000). Charged particle environment for NGST: L2 plasma environment statistics (J. B. Breckinridge & P. Jakobsen, Eds.). In J. B. Breckinridge & P. Jakobsen (Eds.), *UV, Optical, and IR Space Telescopes and Instruments*, SPIE. International Society for Optics and Photonics. <https://doi.org/10.1117/12.393969>
- [36] Barth, J. L., Isaacs, J. C., & Poivey, C. (2000). *The Radiation Environment for the Next Generation Space Telescope* (tech. rep.). Goddard Space Flight Center. https://www.researchgate.net/publication/237482204_The_Radiation_Environment_for_the_Next_Generation_Space_Telescope
- [37] Ambrosi, R. M., Holland, A. D., Smith, D. R., Hutchinson, I., & Denby, M. (2005). The effect of the prompt particle environment at l2 on optical ccds for astronomy and astrophysics. *Planetary and Space Science*, 53(14), 1449–1465. <https://doi.org/https://doi.org/10.1016/j.pss.2005.10.004>
- [38] G. R. Ricker et al. (2014). Transiting Exoplanet Survey Satellite. *Journal of Astronomical Telescopes, Instruments, and Systems*, 1(1), 1–10. <https://doi.org/10.1117/1.JATIS.1.1.014003>
- [39] NASA. (2020a). *What is a Lagrange Point?* <https://solarsystem.nasa.gov/resources/754/what-is-a-lagrange-point/>
- [40] ESA. (2020d). *What are Lagrange points?* https://www.esa.int/Enabling_Support/Operations/What_are_Lagrange_points
- [41] Dr. Drang. (2020). *Lagrange points redux*. <https://leancrew.com/all-this/2016/08/lagrange-points-redux/>
- [42] NASA. (2020b). *The Lagrange points*. <https://map.gsfc.nasa.gov/ContentMedia/lagrange.pdf>
- [43] Britannica. (2020). *D'Alembert's principle*. <https://www.britannica.com/science/dAlemberts-principle>
- [44] ESA. (2020e). *Types of orbits*. https://www.esa.int/Enabling_Support/Space_Transportation/Types_of_orbits#LEO
- [45] Miers, T. (1994). System design of a mission to detect earth-sized planets in the inner orbits of solar-like stars. *Journal of Geophysical Research*, 101, 9297–9302. https://www.researchgate.net/figure/Geometry-and-time-line-for-an-L2-halo-orbit-The-L2-Lagrange-point-is-on-the-Sun-Earth_fig2_259063722

- [46] Bernelli Zazzera, F., Topputo, F., Massari, M., & Izzo, D. (n.d.). *Assessment of Mission Design Including Utilization of Libration Points and Weak Stability Boundaries* (tech. rep.). www.esa.int/int/act
- [47] Koon, W. S. *CDS140B: Computation of Halo Orbit*. 2004. http://www.cds.caltech.edu/archive/help/uploads/wiki/files/39/lecture_halo_2004.pdf
- [48] Jordi Carlos García García. (2009). *Analysis of the Gaia orbit around L2* (tech. rep.). Escola Politècnica Superior de Castelldefels, UPC. <https://upcommons.upc.edu/bitstream/handle/2099.1/8131/memoria.pdf>
- [49] S. Clark and G. Pilbratt. (2009). *HERSCHEL SCIENCE AND LEGACY* (tech. rep.). ESA. <https://sci.esa.int/web/herschel>
- [50] Hechler, M. *Orbiting L2 Observation Point in Space*. 2009. <https://sci.esa.int/documents/32965/35909/1567257599705-hp-sst-martin-hechler.pdf>
- [51] Arianespace. (2018a). *Soyuz User's Manual*. <https://www.arianespace.com/wp-content/uploads/2015/10/Soyuz-UsersManual-issue2-Revision1-May18.pdf>
- [52] Arianespace. (2020). *Ariane 5 User's Manual*. <https://www.arianespace.com/wp-content/uploads/2016/10/Ariane5-users-manual-Jun2020.pdf>
- [53] Arianespace. (2018b). *Ariane 6 User's Manual*. https://www.arianespace.com/wp-content/uploads/2018/04/Mua-6_Issue-1_Revision-0_March-2018.pdf
- [54] Xu, Q., Hollingsworth, P., & Smith, K. (2019). Launch Cost Analysis and Optimization Based on Analysis of Space System Characteristics, 62(4), 175–183.
- [55] Futron Corporation. (2002). *Space Transportation Costs: Trends in Price Per Pound to Orbit 1990-2000* (tech. rep.). Maryland, USA. <https://www.yumpu.com/en/document/read/36996100/space-transportation-costs-trends-in-price-per-pound-to-orbit->
- [56] Arianespace. (2000). *A.S.A.P. 5 User's Manual*. <https://www.brown.edu/Departments/Engineering/Courses/en176/2003%20Lectures/Meeting%203/ASAP5-manual.pdf>
- [57] Arianespace. (2017). *Soyuz ASuxiliary Passengers User's Manual*. https://www.arianespace.com/wp-content/uploads/2017/07/Auxiliary_Passengers_June_2017.pdf
- [58] GAIA Science Advisory Group. (2000). *GAIA: Composition, Formation and Evolution of the Galaxy* (tech. rep.). ESA. http://www.rssd.esa.int/doc_fetch.php?id=359232
- [59] Vanderspek, R., Doty, J. P., Fausnaugh, M., Villaseñor, J. N. S., Jenkins, J. M., Berta-Thompson, Z. K., Burke, C. J., & Ricker, G. R. (2018). *TESS Instrument Handbook*. https://archive.stsci.edu/files/live/sites/mast/files/home/missions-and-data/active-missions/tess/_documents/TESS_Instrument_Handbook_v0.1.pdf
- [60] Cleve, J. V., & Caldwell, D. (2016). *Kepler Instrument Handbook*. https://archive.stsci.edu/files/live/sites/mast/files/home/missions-and-data/kepler/_documents/KSCI-19033-002-instrument-hb.pdf
- [61] Kramer, H. J. (2020). *TESS (Transiting Exoplanet Survey Satellite)*. <https://directory.eoportal.org/web/eoportal/satellite-missions/t/tess> (accessed: 08/01/2021)
- [62] Endicott, J., Walker, A., Bowring, S., Turner, P., Allen, D., Piersanti, O., Short, A., & Walton, D. (2012). Charge-coupled devices for the ESA PLATO M-class Mission (A. D. Holland & J. W. Beletic, Eds.). In A. D. Holland & J. W. Beletic (Eds.), *High Energy, Optical, and Infrared Detectors for Astronomy V*, SPIE. International Society for Optics and Photonics. <https://doi.org/10.1117/12.926299>
- [63] Verhoeve, P., Prod'homme, T., Oosterbroek, T., Duvet, L., Beaufort, T., Blommaert, S., Butler, B., Heijnen, J., Lemmel, F., van der Luijt, C., Smit, H., & Visser, I. (2016). Optical and dark characterization of the PLATO CCD at ESA (A. D. Holland & J. Beletic, Eds.). In A. D. Holland & J. Beletic (Eds.), *High Energy, Optical, and Infrared Detectors for Astronomy VII*, SPIE. International Society for Optics and Photonics. <https://doi.org/10.1117/12.2232336>
- [64] Beaufort, T., Duvet, L., Bloemmaert, S., Lemmel, F., Prod'homme, T., Verhoeve, P., Smit, H., Butler, B., van der Luijt, C., Heijnen, J., & Visser, I. (2016). ESA's CCD test bench for the PLATO mission (A. D. Holland & J. Beletic, Eds.). In A. D. Holland & J. Beletic (Eds.), *High Energy, Optical, and Infrared Detectors for Astronomy VII*, SPIE. International Society for Optics and Photonics. <https://doi.org/10.1117/12.2232343>

- [65] Prod'homme, T., Verhoeve, P., Beaufort, T., Duvet, L., Lemmel, F., Smit, H., Blommaert, S., Oosterbroek, T., van der Luijt, C., Visser, I., Heijnen, J., & Butler, B. (2016). Technology validation of the PLATO CCD at ESA (A. D. Holland & J. Beletic, Eds.). In A. D. Holland & J. Beletic (Eds.), *High Energy, Optical, and Infrared Detectors for Astronomy VII*, SPIE. International Society for Optics and Photonics. <https://doi.org/10.1117/12.2231598>
- [66] *Space systems — Definition of the Technology Readiness Levels (TRLs) and their criteria of assessment* (Standard). (2013). International Organization for Standardization. Geneva, CH.
- [67] Pisacane, V. L. (2005). *Fundamentals of space systems* (2nd ed.). Oxford University Press.
- [68] Qioptiq - An Excelitas Technologies Company. *Optical Solar Reflectors*. 2021. https://www.excelitas.com/file-download/download/public/58606?filename=Qioptiq_Space-Qualified_Solar_Reflectors_Datasheet.pdf
- [69] Excelitas Technologies. (2021). *Optical Solar Reflectors*. <https://www.excelitas.com/product/optical-solar-reflectors>
- [70] Planck Collaboration. (2005). *The Scientific Programme of Planck (Bluebook)* (tech. rep.). ESA. https://www.cosmos.esa.int/documents/387566/387653/Bluebook-ESA-SCI%282005%5C291_V2.pdf/d364e30e-f85f-4191-a989-fa6b7527ba55
- [71] ESA. (2020f). *Herschel Explanatory Supplement Volume I*. <https://www.cosmos.esa.int/web/herschel/legacy-documentation-observatory>
- [72] Guter, W., Dunzer, F., Ebel, L., Hillerich, K., Köstler, W., Kubera, T., Meusel, M., Postels, B., & Wächter, C. (2017). Space Solar Cells - 3G30 and Next Generation Radiation Hard Products. *E3S Web Conf.*, 16, 03005. <https://doi.org/10.1051/e3sconf/20171603005>
- [73] European Space Agency. (2020e). *Next Generation Upright Metamorphic 4-Junction Space Solar Cells*. <https://artes.esa.int/projects/next-generation-upright-metamorphic-4junction-space-solar-cells>
- [74] AZUR SPACE Solar Power GmbH. (2019a). *News*. <http://www.azurspace.com/index.php/en/azur-news> (accessed: 26/12/2020)
- [75] AZUR SPACE Solar Power GmbH. *32% Quadruple Junction GaAs Solar Cell*. 2019. http://www.azurspace.com/images/0005979-01-01_DB_4G32C_Advanced.pdf
- [76] European Space Agency. (2017). *Spacecraft and Satellite Handbook - Herschel Explanatory Supplement Volume I*. <https://www.cosmos.esa.int/web/herschel/legacy-documentation-observatory>
- [77] EnerSys. (2021). *ABSL Space*. <https://www.enersys.com/en/solutions/batteries/absl/absl-space/> (accessed: 08/01/2021)
- [78] Saft - a company of Total. (2021). *Spacecraft Batteries*. <https://www.saftbatteries.com/market-sectors/aerospace-defense/space> (accessed: 08/01/2021)
- [79] Saft - a company of Total. *4S1P VES16 battery*. 2019. <https://www.saftbatteries.com/products-solutions/products/4s1p-ves16-battery>
- [80] EnerSys. *Li-Ion Rechargeable Battery ABSL 8s3p 28V 4.5Ah*. 2017. https://www.enersys.com/48d636/globalassets/documents---legacy/americas/batteries/absl/us-absl-1-aa-august-2017_8s3p-4.5ah-battery.pdf
- [81] Allen, B. (2019). *Cyclone Global Navigation Satellite System (CYGNSS)*. <https://www.nasa.gov/cygnss> (accessed: 08/01/2021)
- [82] NASA. (2020c). *JWST Attitude Control Subsystem*. <https://jwst-docs.stsci.edu/jwst-observatory-hardware/jwst-spacecraft-bus/jwst-attitude-control-subsystem>
- [83] Purdue. (2020). *Satellite Propulsion*. <https://engineering.purdue.edu/~propulsi/propulsion/rockets/satellites.html>
- [84] NASA. (2020d). *Observatory - Pointing Control*. <https://www.nasa.gov/content/goddard/hubble-space-telescope-pointing-control-system>
- [85] Collins Aerospace. (2020). *RDR 68 Momentum and Reaction Wheels*. <https://www.collinsaerospace.com/en/what-we-do/Space/Space-Wheels/Rdr-68-Momentum-And-Reaction-Wheel>
- [86] Honeywell. (2020). *HR04 Reaction Wheel Assembly (RWA)*. <https://aerospace.honeywell.com/en/learn/products/space/small-satellite-specific-bus-products/hr04-reaction-wheel-assembly>

- [87] Rovira Garcia, A. *Module 5 Space Vehicles subsystems*. Escola Superior d'Enginyeries Industrial, Aeroespacial i Audiovisual de Terrassa. Grau en Enginyeria en Tecnologies Aeroespacials (Pla 2010). *Space Engineering*. 2020.
- [88] VACCO Industries. (2004). *VACCO Space Products*. https://www.vacco.com/images/uploads/pdfs/cold_gas_thrusters.pdf
- [89] Spacetech. (2020). *CESS - COARSE EARTH SUN SENSOR*. <https://www.spacetech-i.com/products/electronics-sensors/coarse-earth-sun-sensor-cess>
- [90] NASA. (2020e). *JWST Mission Operations Concept Document*. https://spacese.spacegrant.org/JWST_Mission_Operations_Concept_Document.pdf
- [91] ESA. (2020g). *Satellite frequency bands*. https://www.esa.int/Applications/Telecommunications_Integrated_Applications/Satellite_frequency_bands
- [92] NASA. (2020f). *Mars Reconnaissance Orbiter*. <https://mars.nasa.gov/mro/mission/spacecraft/parts/telecommunications/>
- [93] NASA JPL. (2020). *Voyager High Gain Antenna*. <https://voyager.jpl.nasa.gov/mission/spacecraft/instruments/hga/>
- [94] Plato Mission. (2020). *Operations at the Lagrange point 2 (L2)*. <https://platomission.com/2018/05/19/operations-at-the-lagrange-point-2-12/>
- [95] NASA. (2020g). *James Webb Space Telescope (JWST) Project Overview*. <https://ntrs.nasa.gov/api/citations/20050244862/downloads/20050244862.pdf>

Appendices

Appendix 1: Soyuz ascent code

These MATLAB codes perform a study of the two first vertical ascent phases of the selected launch vehicle. A numerical integration is performed using a 4rd-order Runge-Kutta solver.

Phase 1

The following code analyses and outputs the resultant heights and altitudes for the first stage.

```

1 %% ROCKET LAUNCH WITH DRAG
2
3 clear all;
4 close all;
5 clc;
6
7 %% 1. Definition of Constants, Parameters and Variables
8
9 % 1.1. CONSTANTS
10
11 G = 6.67408e-11; % Gravitational Constant [m
12 ^3/(kg*s^2)]
13 R = 8.31432; % Universal Constant for Ideal Gases [J/
14 mole*K]
15
16 % 1.1.1. Earth
17 R_Earth = 6371.0e3; % Radius of Earth [m]
18 M_Earth = 5.9724e24; % Earth's Mass [kg]
19
20 g0_Earth = 9.80665; % Acceleration at Earth's surface [m/
21 s^2]
22 T0_Earth = 288.15; % US Standard Sea Level Temperature [K]
23 P0_Earth = 101325; % Pressure at Sea Level [Pa]
24
25 Mm_Earth = 28.9644*10^-3; % Molecular Mass [kg
26 *mole^-1]
27 gamma_gas_Earth = 1.4; % Earth's air specific heats relation [
28 adim]
29
30 % Earth's atmospheric layers altitude [m]
31 H_layer_Earth = 1e3*[0 11 20 32 47 52 61 69 79 90 100 110 117.776];
32 % Earth's atmospheric layers thermal gradient [K/m]
33 lambda_layer_Earth = 1e-3*[-6.5 0 1 2.8 0 -2 -4 -3 0 2 4.36 16.4596 0];
34
35 % 2.3. Compute base temperatures and pressures
36 [Tb, Pb] = getBaseTemperaturePressure(R, g0_Earth, T0_Earth, P0_Earth,
Mm_Earth, H_layer_Earth, lambda_layer_Earth);
37
38 %% 1.3. VARIABLES
39 syms V; % Vehicle velocity [m/
40 s]
41 syms gamma; % Vehicle flight path angle [
42 rad]
43 syms h; % Vehicle altitude [m]
44 syms r; % Vehicle flight range [m]
45 syms t; % Vehicle time of flight [s]
```

```

37 syms g; % Acceleration [m/
38 syms Q; % Dynamic pressure at h [Pa
39 ]
40 syms W; % Vehicle weight [N]
41 syms C_D; % Drag Coefficient [
42 adim]
43 syms A; % Vehicle reference area used in C_D [m
44 ^2]
45 %syms beta; % Ballistic coefficient [N/
46 m^2]
47 syms C_L; % Veicle lift coefficient [
48 adim]

49
50
51
52
53
54
55
56
57
58
59
60
61
62
63
64
65
66
67
68
69
70
71
72
73
74
75
76
77
78
79
80
81
82
83
84
85
86

```

```

syms g; % Acceleration [m/
syms Q; % Dynamic pressure at h [Pa
]
syms W; % Vehicle weight [N]
syms C_D; % Drag Coefficient [
syms A; % Vehicle reference area used in C_D [m
^2]
%syms beta; % Ballistic coefficient [N/
m^2]
syms C_L; % Veicle lift coefficient [
adim]

%% Input data and Previous calculation

S_ref = 83.32; % m^2
Pc = 245e5; % Pa
Tc = 3701; % K
gamma = 1.24;
m0 = 39160; % kg
mW = 21.9e-3; % g/mol
m_dot = 234.218; % kg/sec

Ae_At = 45;

R_comb = 8.31432/(mW);
c_car = sqrt(R_comb*Tc)/0.6581;
At = (m_dot*c_car)/Pc;
MPF_e(:,1) = 0.6581./Ae_At(:,1);

for i=1:length(MPF_e)
    syms M;
    M = vpasolve(MPF_e(i,1) == sqrt(gamma)* M / ((1 + (gamma-1)/2 *M^2)^((gamma+1)/(2*(gamma-1)))), M, [1,6]);
    Me(i,1) = M;
end

P_e = zeros(length(Ae_At),1);
for t=1:length(Ae_At)
    P_e(t,1) = Pc/(1+Me(t,1)^2*((gamma-1)/2))^((gamma/(gamma-1)));
end

%% Numerical integration

final_time = 118; % Final time for computations [s]
time_step = 0.5; % Step size [s]
time = 0:time_step:final_time; % Calculates upto final_time

h = zeros(length(Ae_At),length(time));
v = zeros(length(Ae_At),length(time));

h(:,1) = 0; % initial condition of altitude
v(:,1) = 0; % initial

```

```

    condition of velocity
87
88 % Altitude EDO
89
90 F_th = @(t,r,s) s;
91
92 % Velocity EDO
93
94 F_tv = @(t,r,s,p,q,c,m,ratio,coef) (Pc*At*((2/(gamma+1))^(gamma+1)/(2*(gamma-1)))*(gamma*m+(1/m))/(sqrt(1+(m^2*(gamma-1)/2)))-((p/Pc)*ratio))- (0.5*q*s^2*S_ref*coef)/(m0-m_dot*t) - 9.80665;
95 % Velocity EDO
96
97 for i=1:length(Ae_At)
98     for j=1:(length(time)-1)
99         calculation loop %
100
101     [T, P, rho, a] = computeAtmosphere(Tb, Pb, H_layer_Earth,
102                                         lambda_layer_Earth, R, g0_Earth, Mm_Earth, h(i,j));
103
104     Mach = v(i,j)/a;
105
106     if Mach <= 0.6
107         C_D = 0.15;
108
109     elseif Mach>0.6 && Mach <= 1.1
110         C_D = -4.32*Mach^3 + 11.016*Mach^2 - 8.5536*Mach + 2.24952;
111
112     elseif Mach>1.1 && Mach <= 1.3
113         C_D = -Mach^2 + 2.2*Mach - 0.79;
114
115     else
116
117         C_D = 0.16769 + 0.17636/sqrt(Mach^2-1);
118
119     end
120
121     if P_e(i,1) < (0.4*P)
122
123         Me_prima(i,1) = sqrt((2/(gamma-1)) * ((Pc/(0.4*P))^(gamma-1)/gamma));
124         Ae_At_prima(i,1) = 0.6581 / (sqrt(gamma)*Me_prima(i,1)/(1+((gamma-1)/2)*Me_prima(i,1)^2)^(gamma+1)/(2*(gamma-1)));
125
126         k_1h = F_th(time(j),h(i,j),v(i,j));
127         k_1v = F_tv(time(j),h(i,j),v(i,j),P,rho,a,Me_prima(i,1),Ae_At_prima(i,1),C_D);
128
129         k_2h = F_th(time(j)+0.5*time_step,h(i,j)+0.5*time_step*k_1h,v(i,j)+0.5*time_step*k_1v);
130         k_2v = F_tv(time(j)+0.5*time_step,h(i,j)+0.5*time_step*k_1h,v(i,j)+0.5*time_step*k_1v,P,rho,a,Me_prima(i,1),Ae_At_prima(i,1),C_D);
131
132
133

```

```

134 k_3h = F_th((time(j)+0.5*time_step),(h(i,j)+0.5*time_step*k_2h),(v(
135   i,j)+0.5*time_step*k_2v));
136 k_3v = F_tv((time(j)+0.5*time_step),(h(i,j)+0.5*time_step*k_2h),(v(
137   i,j)+0.5*time_step*k_2v),P,rho,a,Me_prima(i,1),Ae_At_prima(i,1),
138   C_D);
139
140
141   else
142
143     k_1h = F_th(time(j),h(i,j),v(i,j));
144     k_1v = F_tv(time(j),h(i,j),v(i,j),P,rho,a,Me(i,1),Ae_At(i,1),C_D);
145
146     k_2h = F_th(time(j)+0.5*time_step,h(i,j)+0.5*time_step*k_1h,v(i,j)
147       +0.5*time_step*k_1v);
148     k_2v = F_tv(time(j)+0.5*time_step,h(i,j)+0.5*time_step*k_1h,v(i,j)
149       +0.5*time_step*k_1v,P,rho,a,Me(i,1),Ae_At(i,1),C_D);
150
151     k_3h = F_th((time(j)+0.5*time_step),(h(i,j)+0.5*time_step*k_2h),(v(
152       i,j)+0.5*time_step*k_2v));
153     k_3v = F_tv((time(j)+0.5*time_step),(h(i,j)+0.5*time_step*k_2h),(v(
154       i,j)+0.5*time_step*k_2v),P,rho,a,Me(i,1),Ae_At(i,1),C_D);
155
156   end
157
158   h(i,j+1) = h(i,j) + (1/6)*(k_1h+2*k_2h+2*k_3h+k_4h)*time_step; %  

159   main altitude equation
160   v(i,j+1) = v(i,j) + (1/6)*(k_1v+2*k_2v+2*k_3v+k_4v)*time_step; %  

161   main altitude equation
162   q(i,j+1) = 0.5*rho*v(i,j+1)^2;
163
164 end
165 legend_str = cell(length(Ae_At), 1);
166 for i = 1:length(Ae_At)
167   legend_str(i,1) = {sprintf('$A_e/A_t = %d$', Ae_At(i))};
168 end
169
170 save('h_first_stage','h');
171 save('v_first_stage','v');
172 save('q_first_stage','q');
173 save('time_first_stage','time');
174
175
176
177 figure(1);
178 hold on;

```

```

179 set(groot, 'defaultAxesTickLabelInterpreter', 'latex');
180 set(groot, 'defaultTextInterpreter', 'latex');
181 set(groot, 'defaultLegendInterpreter', 'latex');
182 for i = 1:length(Ae_At)
183     plot(time, h(i,:)/1e3, 'b');
184 end
185 title('\textbf{Altitude vs. Time (With Drag)}');
186 xlabel('Time $\left[ \mathrm{s} \right]$');
187 ylabel('Altitude $\left[ \mathrm{km} \right]$');
188 set(gcf, 'units', 'centimeters', 'position', [1, 1, 18, 15]);
189 grid on;
190 grid minor;
191 box on;
192 legend(legend_str, 'Location', 'Northwest');
193 hold off;

195
196 figure(2);
197 hold on;
198 title('\textbf{Velocity vs. Time (With Drag)}')
199 set(groot, 'defaultAxesTickLabelInterpreter', 'latex');
200 set(groot, 'defaultTextInterpreter', 'latex');
201 set(groot, 'defaultLegendInterpreter', 'latex');
202 for i = 1:length(Ae_At)
203     plot(time, v(i,:), 'b');
204 end
205 xlabel('Time $\left[ \mathrm{s} \right]$');
206 ylabel('Velocity $\left[ \mathrm{m} / \mathrm{s} \right]$');
207 set(gcf, 'units', 'centimeters', 'position', [19, 1, 18, 15]);
208 grid on;
209 grid minor;
210 box on;
211 legend(legend_str, 'Location', 'Northwest');
212 hold off;

213
214 figure(3);
215 hold on;
216 title('\textbf{Dynamic Pressure vs. Time (With Drag)}')
217 set(groot, 'defaultAxesTickLabelInterpreter', 'latex');
218 set(groot, 'defaultTextInterpreter', 'latex');
219 for i = 1:length(Ae_At)
220     plot(time, q(i,:), 'b');
221 end
222 xlabel('Time $\left[ \mathrm{s} \right]$');
223 ylabel('Dynamic Pressure $\left[ \mathrm{Pa} \right]$');
224 set(gcf, 'units', 'centimeters', 'position', [19, 1, 18, 15]);
225 grid on;
226 grid minor;
227 box on;
228 hold off;

```

The next code allows to obtain the resultant forces (i.e. thrust, drag and weight).

```

1 %% ROCKET LAUNCH WITH DRAG
2
3 clear all;
4 close all;
5 clc;

```

```

6
7
8 %% 1. Definition of Constants, Parameters and Variables
9
10 % 1.1. CONSTANTS
11
12 G = 6.67408e-11; % Gravitational Constant [m
13 ^3/(kg*s^2)]
14 R = 8.31432; % Universal Constant for Ideal Gases [J/
15 mole*K]
16
17 % 1.1.1. Earth
18 R_Earth = 6371.0e3; % Radius of Earth [m]
19 M_Earth = 5.9724e24; % Earth's Mass [kg]
20 ]
21 g0_Earth = 9.80665; % Acceleration at Earth's surface [m/
22 s^2]
23 T0_Earth = 288.15; % US Standard Sea Level Temperature [K]
24 P0_Earth = 101325; % Pressure at Sea Level [Pa]
25 ]
26 Mm_Earth = 28.9644*10^-3; % Molecular Mass [kg
27 *mole^-1]
28 gamma_gas_Earth = 1.4; % Earth's air specific heats relation [
29 adim]
30
31 % Earth's atmospheric layers altitude [m]
32 H_layer_Earth = 1e3*[0 11 20 32 47 52 61 69 79 90 100 110 117.776];
33 % Earth's atmospheric layers thermal gradient [K/m]
34 lambda_layer_Earth = 1e-3*[-6.5 0 1 2.8 0 -2 -4 -3 0 2 4.36 16.4596 0];
35
36 % 2.3. Compute base temperatures and pressures
37 [Tb, Pb] = getBaseTemperaturePressure(R, g0_Earth, T0_Earth, P0_Earth,
38 Mm_Earth, H_layer_Earth, lambda_layer_Earth);
39
40 % 1.3. VARIABLES
41
42 syms V; % Vehicle velocity [m/
43 s]
44 syms gamma; % Vehicle flight path angle [
45 rad]
46 syms h; % Vehicle altitude [m]
47 syms r; % Vehicle flight range [m]
48 syms t; % Vehicle time of flight [s]
49 syms g; % Acceleration [m/
50 s^2]
51 syms Q; % Dynamic pressure at h [Pa]
52 ]
53 syms W; % Vehicle weight [N]
54 syms C_D; % Drag Coefficient [
55 adim]
56 syms A; % Vehicle reference area used in C_D [m
57 ^2]
58 %syms beta; % Ballistic coefficient [N/
59 m^2]
60 syms C_L; % Veicle lift coefficient [
61 adim]
62
63
64 %% Input data and Previous calculation

```

```

48
49 S_ref = 83.32; % m^2
50 Pc = 245e5; % Pa
51 Tc = 3701; % K
52 gamma = 1.24;
53 m0 = 39160; % kg
54 mW = 21.9e-3; % g/mol
55 m_dot = 234.218; % kg/sec
56
57 Ae_At = 45;
58
59 R_comb = 8.31432/(mW);
60 c_car = sqrt(R_comb*Tc)/0.6581;
61 At = (m_dot*c_car)/Pc;
62 MPF_e(:,1) = 0.6581./Ae_At(:,1);
63
64 for i=1:length(MPF_e)
65     syms M;
66     M = vpasolve(MPF_e(i,1) == sqrt(gamma)* M / ((1 + (gamma-1)/2 *M^2)^(((gamma+1)/(2*(gamma-1))))) , M, [1,6]);
67     Me(i,1) = M;
68 end
69
70 P_e = zeros(length(Ae_At),1);
71 for t=1:length(Ae_At)
72     P_e(t,1) = Pc/(1+Me(t,1)^2*((gamma-1)/2))^(gamma/(gamma-1));
73 end
74
75
76 %% Numerical integration
77
78 time_step=1; % step size
79 time = 0:time_step:122; %
80 % Calculates upto time(60)
81
82 h = zeros(length(Ae_At),length(time));
83 v = zeros(length(Ae_At),length(time));
84 thrust = zeros(length(Ae_At),length(time));
85 drag = zeros(length(Ae_At),length(time));
86 weight = zeros(length(Ae_At),length(time));
87
88 h(:,1) = 0; % initial
89 % condition of altitude
90 v(:,1) = 0; % initial
91 % condition of velocity
92
93 % Altitude EDO
94 F_th = @(t,r,s); %
95
96 F_tv = @(t,r,s,p,q,c,m,ratio,coef) (Pc*At*((2/(gamma+1))^(gamma+1)/(2*(gamma-1)))*(gamma*m+(1/m))/(sqrt(1+(m^2*(gamma-1)/2)) - ((p/Pc)*ratio)) - (0.5*q*s^2*S_ref*coef))/(m0-m_dot*t) - 9.80665; %
97 % Velocity EDO
98 for i=1:length(Ae_At)

```

```

99 % Calculation loop
100 for j=1:(length(time))-1)
101 [T, P, rho, a] = computeAtmosphere(Tb, Pb, H_layer_Earth,
102 lambda_layer_Earth, R, g0_Earth, Mm_Earth, h(i,j));
103
104 Mach = v(i,j)/a;
105 if Mach <= 0.6
106   C_D = 0.15;
107 elseif Mach>0.6 && Mach <= 1.1
108   C_D = -4.32*Mach^3 + 11.016*Mach^2 - 8.5536*Mach + 2.24952;
109 elseif Mach>1.1 && Mach <= 1.3
110   C_D = -Mach^2 + 2.2*Mach - 0.79;
111 else
112   C_D = 0.16769 + 0.17636/sqrt(Mach^2-1);
113 end
114
115 if P_e(i,1) < (0.4*P)
116   Me_prima(i,1) = sqrt((2/(gamma-1)) * ((Pc/(0.4*P))^((gamma-1)/gamma
117     )-1));
118   Ae_At_prima(i,1) = 0.6581 / (sqrt(gamma)*Me_prima(i,1)/(1+((gamma
119     -1)/2)*Me_prima(i,1)^2)^((gamma+1)/(2*(gamma-1))));
120
121 k_1h = F_th(time(j),h(i,j),v(i,j));
122 k_1v = F_tv(time(j),h(i,j),v(i,j),P,rho,a,Me_prima(i,1),Ae_At_prima
123   (i,1),C_D);
124
125 k_2h = F_th(time(j)+0.5*time_step,h(i,j)+0.5*time_step*k_1h,v(i,j)
126   +0.5*time_step*k_1v);
127 k_2v = F_tv(time(j)+0.5*time_step,h(i,j)+0.5*time_step*k_1h,v(i,j)
128   +0.5*time_step*k_1v,P,rho,a,Me_prima(i,1),Ae_At_prima(i,1),C_D);
129
130 k_3h = F_th((time(j)+0.5*time_step),(h(i,j)+0.5*time_step*k_2h),(v(
131   i,j)+0.5*time_step*k_2v));
132 k_3v = F_tv((time(j)+0.5*time_step),(h(i,j)+0.5*time_step*k_2h),(v(
133   i,j)+0.5*time_step*k_2v),P,rho,a,Me_prima(i,1),Ae_At_prima(i,1),
134   C_D);
135
136 k_4h = F_th((time(j)+time_step),(h(i,j)+k_3h*time_step),(v(i,j)+
137   k_3v*time_step));
138 k_4v = F_tv((time(j)+time_step),(h(i,j)+k_3h*time_step),(v(i,j)+
139   k_3v*time_step),P,rho,a,Me_prima(i,1),Ae_At_prima(i,1),C_D);
140
141 thrust(i,j) = (Pc*At*((2/(gamma+1))^((gamma+1)/(2*(gamma-1))))*
142   gamma*Me_prima(i,1)+(1/Me_prima(i,1)))/(sqrt(1+(Me_prima(i,1)
143   ^2*(gamma-1)/2)))-((P/Pc)*Ae_At_prima(i,1)));
144 else
145
146   k_1h = F_th(time(j),h(i,j),v(i,j));
147   k_1v = F_tv(time(j),h(i,j),v(i,j),P,rho,a,Me(i,1),Ae_At(i,1),C_D);
148
149   k_2h = F_th(time(j)+0.5*time_step,h(i,j)+0.5*time_step*k_1h,v(i,j)
150   +0.5*time_step*k_1v);
151   k_2v = F_tv(time(j)+0.5*time_step,h(i,j)+0.5*time_step*k_1h,v(i,j)
152   +0.5*time_step*k_1v,P,rho,a,Me(i,1),Ae_At(i,1),C_D);
153
154   k_3h = F_th((time(j)+0.5*time_step),(h(i,j)+0.5*time_step*k_2h),(v(
155   i,j)+0.5*time_step*k_2v));
156   k_3v = F_tv((time(j)+0.5*time_step),(h(i,j)+0.5*time_step*k_2h),(v(
157   i,j)+0.5*time_step*k_2v));

```

```

141   i , j ) + 0.5 * time_step * k_2v ) , P , rho , a , Me(i , 1) , Ae_At(i , 1) , C_D );
142   k_4h = F_th((time(j)+time_step),(h(i , j)+k_3h*time_step),(v(i , j)+
143   k_3v*time_step));
143   k_4v = F_tv((time(j)+time_step),(h(i , j)+k_3h*time_step),(v(i , j)+
143   k_3v*time_step),P,rho,a,Me(i , 1),Ae_At(i , 1),C_D);
144
145   thrust(i , j) = (Pc*At*((2/(gamma+1))^(((gamma+1)/(2*(gamma-1))))*(

145   gamma*Me(i , 1)+(1/Me(i , 1)))/(sqrt(1+(Me(i , 1)^2*(gamma-1)/2)))-((P
145   /Pc)*Ae_At(i , 1)));
146 end
147
148   h(i , j+1) = h(i , j) + (1/6)*(k_1h+2*k_2h+2*k_3h+k_4h)*time_step; %

148   main altitude equation
149   v(i , j+1) = v(i , j) + (1/6)*(k_1v+2*k_2v+2*k_3v+k_4v)*time_step; %

149   main altitude equation
150
151   drag (i , j) = 0.5*rho*v(i , j)^2*S_ref*C_D;
152   weight (i , j) = (m0-m_dot*time(j))*g0_Earth;
153 end
154
155 figure(1);
156 hold on;
157 title(' \textbf{First stage Forces vs. Time evolution} ');
158 set(groot,'defaultAxesTickLabelInterpreter','latex');
159 set(groot,'defaultTextInterpreter','latex');
160 set(groot,'defaultLegendInterpreter','latex');
161 plot(time, weight(1,:)/1e3, 'r');
162 plot(time, drag(1,:)/1e3, 'g');
163 plot(time, thrust(1,:)/1e3, 'b');
164 xlabel('Time $\left( \mathrm{s} \right)$');
165 ylabel('Force $\left( \mathrm{kN} \right)$');
166 xlim([0 120]);
167 set(gcf, 'units', 'centimeters', 'position', [0, 1, 18, 15]);
168 grid on;
169 grid minor;
170 box on;
171 legend('Weight', 'Drag', 'Thrust', 'Location', 'Northwest');
172 hold off;

```

Phase 2

This code computes and outputs the resultant height and altitudes for the second stage.

```

1 %% ROCKET LAUNCH WITH DRAG
2
3 clear all;
4 close all;
5 clc;
6
7 %% 1. Definition of Constants, Parameters and Variables
8
9 %% 1.1. CONSTANTS
10
11 G = 6.67408e-11; % Gravitational Constant [m
12   ^3/(kg*s^2)]

```

```

13 R = 8.31432; % Universal Constant for Ideal Gases [J/
14 mole*K]
15 % 1.1.1. Earth
16 R_Earth = 6371.0e3; % Radius of Earth [m]
17 M_Earth = 5.9724e24; % Earth's Mass [kg]
18 g0_Earth = 9.80665; % Acceleration at Earth's surface [m/
19 s^2]
20 T0_Earth = 288.15; % US Standard Sea Level Temperature [K]
21 P0_Earth = 101325; % Pressure at Sea Level [Pa]
22 Mm_Earth = 28.9644*10^-3; % Molecular Mass [kg
*mole^-1]
23 gamma_gas_Earth = 1.4; % Earth's air specific heats relation [
24 adim]
25 % Earth's atmospheric layers altitude [m]
26 H_layer_Earth = 1e3*[0 11 20 32 47 52 61 69 79 90 100 110 117.776];
27 % Earth's atmospheric layers thermal gradient [K/m]
28 lambda_layer_Earth = 1e-3*[-6.5 0 1 2.8 0 -2 -4 -3 0 2 4.36 16.4596 0];
29 % 2.3. Compute base temperatures and pressures
30 [Tb, Pb] = getBaseTemperaturePressure(R, g0_Earth, T0_Earth, P0_Earth,
31 Mm_Earth, H_layer_Earth, lambda_layer_Earth);
32 % 1.3. VARIABLES
33 syms V; % Vehicle velocity [m/
34 syms gamma; % Vehicle flight path angle [
35 syms h; % Vehicle altitude [m]
36 syms r; % Vehicle flight range [m]
37 syms t; % Vehicle time of flight [s]
38 syms g; % Acceleration [m/
39 syms Q; % Dynamic pressure at h [Pa]
40 syms W; % Vehicle weight [N]
41 syms C_D; % Drag Coefficient [
42 syms A; % Vehicle reference area used in C_D [m
43 %syms beta; % Ballistic coefficient [N/
44 syms C_L; % Veicle lift coefficient [
45 adim]
46
47 %% Input data and Previous calculation
48
49
50 S_ref = 83.32; % m^2
51 Pc = 51e5; % Pa
52 Tc = 3701; % K
53 gamma = 1.24; % kg
54 m0 = 90100; % g/mol
55 mw = 21.9e-3;

```

```

56 m_dot = 253.244;                                     % kg/sec
57
58 Ae_At = 60;
59
60 R_comb = 8.31432/(mW);
61 c_car = sqrt(R_comb*Tc)/0.6581;
62 At = (m_dot*c_car)/Pc;
63 MPF_e(:,1) = 0.6581./Ae_At(:,1);
64
65 for i=1:length(MPF_e)
66     syms M;
67     M = vpasolve(MPF_e(i,1) == sqrt(gamma)* M / ((1 + (gamma-1)/2 *M^2)^(((gamma+1)/(2*(gamma-1)))) , M, [1,6]);
68     Me(i,1) = M;
69 end
70
71 P_e = zeros(length(Ae_At),1);
72 for t=1:length(Ae_At)
73     P_e(t,1) = Pc/(1+Me(t,1)^2*((gamma-1)/2))^(gamma/(gamma-1));
74 end
75
76
77 %% Numerical integration
78
79 final_time = 282;                                     % Final time for computations [s]
80 time_step = 0.5;                                      % Step size [s]
81 time_2 = 118:time_step:final_time;                   % Calculates upto final_time
82
83 h_2 = zeros(length(Ae_At),length(time_2));
84 v_2 = zeros(length(Ae_At),length(time_2));
85
86 h_2(:,1) = 5.1002e4;                                 %
87     initial condition of altitude
88 v_2(:,1) = 1.6136e3;                                 %
89     initial condition of velocity
90
91 % Altitude EDO
92
93 F_th = @(t,r,s) s*0.2588;
94
95 % Velocity EDO
96
97 F_tv = @(t,r,s,p,q,c,m,ratio,coef) (Pc*At*((2/(gamma+1))^((gamma+1)/(2*(gamma-1)))*(gamma*m+(1/m))/(sqrt(1+(m^2*(gamma-1)/2))-((p/Pc)*ratio))-(0.5*q*s^2*S_ref*coef))/(m0-m_dot*t)-9.80665;
98     % Velocity EDO
99
100 for i=1:length(Ae_At)
101
102     for j=1:(length(time_2)-1)
103         % calculation loop
104
105         [T, P, rho, a] = computeAtmosphere(Tb, Pb, H_layer_Earth,
106                                         lambda_layer_Earth, R, g0_Earth, Mm_Earth, h_2(i,j));
107
108         Mach = v_2(i,j)/a;

```

```

106      if Mach <= 0.6
107          C_D = 0.15;
108
109      elseif Mach>0.6 && Mach <= 1.1
110          C_D = -4.32*Mach^3 + 11.016*Mach^2 - 8.5536*Mach + 2.24952;
111
112      elseif Mach>1.1 && Mach <= 1.3
113          C_D = -Mach^2 + 2.2*Mach - 0.79;
114
115      else
116          C_D = 0.16769 + 0.17636/sqrt(Mach^2-1);
117
118      end
119
120      if P_e(i,1) < (0.4*P)
121
122          Me_prima(i,1) = sqrt((2/(gamma-1)) * ((Pc/(0.4*P))^((gamma-1)/gamma
123              )-1));
124          Ae_At_prima(i,1) = 0.6581 / (sqrt(gamma)*Me_prima(i,1)/(1+((gamma
125              -1)/2)*Me_prima(i,1)^2)^((gamma+1)/(2*(gamma-1))));
126
127          k_1h = F_th(time_2(j),h_2(i,j),v_2(i,j));
128          k_1v = F_tv(time_2(j),h_2(i,j),v_2(i,j),P,rho,a,Me_prima(i,1),
129              Ae_At_prima(i,1),C_D);
130
131          k_2h = F_th(time_2(j)+0.5*time_step,h_2(i,j)+0.5*time_step*k_1h,v_2
132              (i,j)+0.5*time_step*k_1v);
133          k_2v = F_tv(time_2(j)+0.5*time_step,h_2(i,j)+0.5*time_step*k_1h,v_2
134              (i,j)+0.5*time_step*k_1v,P,rho,a,Me_prima(i,1),Ae_At_prima(i,1),
135              C_D);
136
137          k_3h = F_th((time_2(j)+0.5*time_step),(h_2(i,j)+0.5*time_step*k_2h)
138              ,(v_2(i,j)+0.5*time_step*k_2v));
139          k_3v = F_tv((time_2(j)+0.5*time_step),(h_2(i,j)+0.5*time_step*k_2h)
140              ,(v_2(i,j)+0.5*time_step*k_2v),P,rho,a,Me_prima(i,1),Ae_At_prima
141              (i,1),C_D);
142
143      else
144          k_1h = F_th(time_2(j),h_2(i,j),v_2(i,j));
145          k_1v = F_tv(time_2(j),h_2(i,j),v_2(i,j),P,rho,a,Me(i,1),Ae_At(i,1),
146              C_D);
147
148          k_2h = F_th(time_2(j)+0.5*time_step,h_2(i,j)+0.5*time_step*k_1h,v_2
149              (i,j)+0.5*time_step*k_1v);
149          k_2v = F_tv(time_2(j)+0.5*time_step,h_2(i,j)+0.5*time_step*k_1h,v_2
149              (i,j)+0.5*time_step*k_1v,P,rho,a,Me(i,1),Ae_At(i,1),C_D);

```

```

150 k_3h = F_th((time_2(j)+0.5*time_step),(h_2(i,j)+0.5*time_step*k_2h)
151 , (v_2(i,j)+0.5*time_step*k_2v));
152 k_3v = F_tv((time_2(j)+0.5*time_step),(h_2(i,j)+0.5*time_step*k_2h)
153 , (v_2(i,j)+0.5*time_step*k_2v),P,rho,a,Me(i,1),Ae_At(i,1),C_D);
154 k_4h = F_th((time_2(j)+time_step),(h_2(i,j)+k_3h*time_step),(v_2(i,
155 j)+k_3v*time_step));
156 k_4v = F_tv((time_2(j)+time_step),(h_2(i,j)+k_3h*time_step),(v_2(i,
157 j)+k_3v*time_step),P,rho,a,Me(i,1),Ae_At(i,1),C_D);
158 h_2(i,j+1) = h_2(i,j) + (1/6)*(k_1h+2*k_2h+2*k_3h+k_4h)*time_step;
159 % main altitude equation
160 v_2(i,j+1) = v_2(i,j) + (1/6)*(k_1v+2*k_2v+2*k_3v+k_4v)*time_step;
161 % main altitude equation
162 q_2(i,j+1) = 0.5*rho*v_2(i,j+1)^2;
163
164 end
165
166 legend_str = cell(length(Ae_At), 1);
167 for i = 1:length(Ae_At)
168 legend_str(i,1) = {sprintf('$A_e/A_t = %d$', Ae_At(i))};
169 end
170
171
172 save('h_second_stage','h_2');
173 save('v_second_stage','v_2');
174 save('q_second_stage','q_2');
175 save('time_second_stage','time_2');

```

Auxiliary codes

The code detailed hereunder loads the outputs of the aforementioned codes and plots the corresponding graphs for both stages.

```

1 %% SOYUZ ROCKET LAUNCH 1st and 2nd STAGES PROFILE
2
3 % Instructions: Run previously the executers launch_drag_phase_1.m and
4 %                 launch_drag_phase_2.m
5
6 clear all;
7 close all;
8 clc;
9
10 load('h_first_stage');
11 load('h_second_stage');
12 load('v_first_stage');
13 load('v_second_stage');
14 load('q_first_stage');
15 load('q_second_stage');
16 load('time_first_stage');
17 load('time_second_stage');
18

```

```

19 time_total = [time time_2];
20 h_total = [h h_2];
21 v_total = [v v_2];
22 q_total = [q q_2];
23
24 figure(1);
25 hold on;
26 title('Altitude vs. Time');
27 set(groot, 'defaultAxesTickLabelInterpreter', 'latex');
28 set(groot, 'defaultTextInterpreter', 'latex');
29 set(groot, 'defaultLegendInterpreter', 'latex');
30 plot (time_total(1:237), h_total(1:237)/1e3, 'b', time_total(238:566),
       h_total(238:566)/1e3, 'r');
31 xlabel('Time $\left[ \mathrm{s} \right]$');
32 ylabel('Altitude $\left[ \mathrm{km} \right]$');
33 set(gcf, 'units', 'centimeters', 'position', [1, 1, 18, 15]);
34 legend('First Stage', 'Second Stage')
35 grid on;
36 grid minor;
37 box on;
38 hold off;
39
40
41 figure(2);
42 hold on;
43 title('Velocity vs. Time');
44 set(groot, 'defaultAxesTickLabelInterpreter', 'latex');
45 set(groot, 'defaultTextInterpreter', 'latex');
46 set(groot, 'defaultLegendInterpreter', 'latex');
47 plot (time_total(1:237), v_total(1:237), 'b', time_total(238:566), v_total
       (238:566), 'r');
48 xlabel('Time $\left[ \mathrm{s} \right]$');
49 ylabel('Velocity $\left[ \mathrm{m} / \mathrm{s} \right]$');
50 set(gcf, 'units', 'centimeters', 'position', [19, 1, 18, 15]);
51 legend('First Stage', 'Second Stage')
52 grid on;
53 grid minor;
54 box on;
55 hold off;
56
57
58 figure(3);
59 hold on;
60 title('Dynamic Pressure vs. Time');
61 set(groot, 'defaultAxesTickLabelInterpreter', 'latex');
62 set(groot, 'defaultTextInterpreter', 'latex');
63 set(groot, 'defaultLegendInterpreter', 'latex');
64 plot (time_total(1:237), q_total(1:237), 'b', time_total(239:566), q_total
       (239:566), 'r');
65 xlabel('Time $\left[ \mathrm{s} \right]$');
66 ylabel('Dynamic Pressure $\left[ \mathrm{Pa} \right]$');
67 set(gcf, 'units', 'centimeters', 'position', [19, 1, 18, 15]);
68 legend('First Stage', 'Second Stage')
69 grid on;
70 grid minor;
71 box on;
72 hold off;

```

The next function computes the atmospherical properties for a given height. Inputs are the reference atmospheric data, such as the base temperature and pressure vectors.

```

1  function [T, P, rho, c] = computeAtmosphere(Tb, Pb, H_layer, lambda, R, g0,
2    Mm, H)
3  %
4  % Inputs:
5  % - Tb      Vector of base temperatures, 1 x length(H_layer)      [K]
6  % - Pb      Vector of base pressure, 1 x length(H_layer)          [Pa]
7  % - H_layer Atmospheric layers altitude                         [m]
8  % - lambda   Atmospheric layers thermal gradients                 [K/m]
9  % - gamma    Ratio of specific heats                            [adim]
10 % - R        Universal gas constant                          [J/(kg K)]
11 % - g0       Acceleration at planet's surface                [m/s^2]
12 % - Mm       Planet's air molar mass                         [kg/mol]
13 %
14 % - H        Altitude                                     [m]
15 %
16 % Outputs:
17 % - T        Temperature at altitude H                      [K]
18 % - P        Pressure at altitude H                        [Pa]
19 % - rho     Density at altitude H                         [kg/m^3]
20 %
21 % Initialize variables
22 T = 0;
23 P = 0;
24 rho = 0;
25 c = 0;
26
27 % Find atmospheric layer
28 found = 0;
29 layer = 1;
30 while (layer <= length(H_layer)-1) && (found == 0)
31   if (H_layer(layer) <= H) && (H < H_layer(layer+1))
32     found = 1;
33   else
34     layer = layer + 1;
35   end
36 end
37
38 % Compute properties
39 if found == 1
40   % Temperature
41   T = Tb(layer) + lambda(layer)*(H - H_layer(layer));
42   % Pressure
43   if lambda(layer) == 0
44     P = Pb(layer)*exp(-g0*Mm*(H-H_layer(layer))/(R*Tb(layer)));
45   else
46     P = Pb(layer)*((Tb(layer)/(Tb(layer) + lambda(layer)*(H-H_layer(
47       layer))))^(g0*Mm/(R*lambda(layer))));
48   end
49   % Density
50   rho = P/((R/Mm)*T);
51   % Specific heats and ratio of specific heats at constant pressure

```

```

51 cp = 1034.09 - 2.849e-1*T + 7.817e-4*T^2 - 4.971e-7*T^3 + 1.077e-10*T
52 ^4;
53 cv = cp - R/Mm;
54 gamma = cp/cv;
55 % Speed of sound
56 c = sqrt(gamma*(R/Mm)*T);
57 end
58 end

```

This function provides the base temperature and pressure vectors, required by the previous function.

```

1 function [Tb, Pb] = getBaseTemperaturePressure(R, g0, T0, P0, Mm, H_layer,
2 %
3 % Inputs:
4 % - R Universal Constant for Ideal Gases [J/mole*K]
5 % - g0 Acceleration at planet's surface [m/s^2]
6 % - T0 Standard Temperature at planet's surface [K]
7 % - P0 Standard Pressure at planet's surface [Pa]
8 % - Mm Atmospheric gas molecular mass [kg*mole^-1]
9 % - H_layer Atmospheric layers altitude [m]
10 % - lambda Atmospheric layers thermal gradients [K/m]
11 %
12 % Outputs:
13 % - Tb Vector of base temperatures, 1 x length(H_layer) [K]
14 % - Pb Vector of base pressures, 1 x length(H_layer) [Pa]
15 % Base (magnitude) refers to the value of (magnitude( at the beginning of
16 % an atmospheric layer
17 %
18 %
19 % Declare vectors of Base Temperature and Pressure
20 Tb = zeros(1, length(H_layer)); % Base Temperature [K]
21 Pb = zeros(1, length(H_layer)); % Base Pressure [Pa]
22 %
23 % Compute Base Temperatures and Pressures for each layer
24 Tb(1) = T0;
25 Pb(1) = P0;
26 for i = 2:length(H_layer)
27 % Compute Base Temperature at layer i
28 Tb(i) = Tb(i-1) + lambda(i-1)*(H_layer(i)-H_layer(i-1));
29 % Compute Base Pressure at layer i
30 if lambda(i-1) == 0 % Isothermal layer
31 Pb(i) = Pb(i-1)*exp(-g0*Mm*(H_layer(i)-H_layer(i-1))/(R*Tb(i-1)));
32 else % Non-isothermal layer
33 Pb(i) = Pb(i-1)*((Tb(i-1)/(Tb(i-1)+lambda(i-1)*(H_layer(i)-H_layer(
34 i-1))))^(g0*Mm/(R*lambda(i-1))));
35 end
36 end
37 % fprintf(end

```

Appendix 2: Orbital Mechanics code

Main program

Program that computes the Hohmann Transfer performance and studies the variation of fuel mass used with respect to the propellant loaded.

```

1 % Program that computes the Hohmann Transfer performance and studies the
2 % variation of fuel mass used with respect to the propellant loaded
3
4 % Preamble
5 clc;
6 clear;
7 close all;
8 set(groot, 'defaultAxesTickLabelInterpreter', 'latex');
9 set(groot, 'defaulttextinterpreter', 'latex');
10 set(groot, 'defaultLegendInterpreter', 'latex');
11
12 %% INPUT DATA
13
14 G=6.6740831e-11; % Universal gravitational constant [N*m^2/kg^2]
15 M_Sun=1.98855e30; % Sun's Mass [kg]
16 M_T=5.972e24; % Earth's Mass [kg]
17 mu = G*M_Sun; % Sun's gravitational parameter [N*m^2/kg]
18 mu_earth = G*M_T; % Earth's gravitational parameter [N*m^2/kg]
19
20 R_E=149598023e3; % Earth orbital radius [m]
21 I_sp = 332; % Specific Impulse [s]
22 g = 9.80665; % Earth acceleration gravity [m/s^2]
23 L2=(M_T/(3*M_Sun))^(1/3)*R_E; % Distance between Earth and Sun-Earth L2 [m]
24 Orbital_radius = [R_E+L2]; % Semi-major axis of the L2 orbit around the Sun
25 [m]
26
27 r_LEO=1000e3; % Chosen LEO height [m]
28 r_LEO_min=160e3; % Minimum LEO height [m]
29 r_LEO_max=1000e3; % Maximum LEO height [m]
30 r_LEO_vec=linspace(r_LEO_min,r_LEO_max,1000); % Vector of LEO heights [m]
31
32 %% HOHMANN TRANSFER PERFORMANCE COMPUTATION
33
34 % Calculation of the HT performance for the chosen LEO height:
35 [Delta_V_Hohmann, delta_t_trans, mass_ratio, r_0, alpha, a_trans, e_trans]=
36 Hohmann_performance(R_E, r_LEO, Orbital_radius, mu, mu_earth, I_sp, g);
37 % Calculation of the HT performance for the entire LEO height vector:
38 [Delta_V_Hohmann_vec, delta_t_trans_vec, mass_ratio_vec, r_0_vec, alpha_vec,
39 a_trans_vec, e_trans_vec]=Hohmann_performance(R_E, r_LEO_vec,
40 Orbital_radius, mu, mu_earth, I_sp, g);
41
42 T=sqrt(4*pi^2/mu*Orbital_radius^3); % L2 transfer time [days]
43 V_earth = sqrt(mu./R_E); % Earth orbital velocity [m/s]
44 omega_Earth=V_earth/R_E; % Earth angular velocity [rad/s]
45 omega_L2=omega_Earth; % L2 angular velocity [rad/s]
46 theta_L2=rad2deg(omega_L2*delta_t_trans*3600*24); %
47 lead_angle=-theta_L2+180; % Lead angle from the L2 target to the SC
48
49 %% FUEL BUDGET COMPUTATION
50
51 % velocity budget
52 m_L2=2165; % Soyuz's maximum payload capability to L2

```

```

49 m_sc=400; % Mass of the Exohalo L2 spacecraft
50 m_main=1250; % Estimated maximum mass of the main passanger
51 m ASAP=425; % Mass of the payload adapter
52 m_p_max=6638; % Maximum mass of fuel that can be loaded into Fregat upper
53   stage
54 m_dry=902; % Fregat's dry mass
55 m_pl=m_sc+m ASAP+m_main; % Payload mass
56
57 % Minimum mass budget required to perform the Hohmann transfer
58 delta_m_min=(m_pl+m_dry)*mass_ratio/(1-1.22*mass_ratio);
59
60 m_p=1.22*delta_m_min; % Initial propellant mass chosen
61
62 % Propellant mass loaded vector
63 m_p_vec=linspace(1.22*delta_m_min,m_p_max,100);
64
65 % Calculation , for the chosen propellant mass, of the fuel for the transfer
66   (m_fuel) and the total fuel of the 3 orbital actions (m_total):
67 [m_fuel,m_total]=fuel_mass_computation(m_p,m_dry,m_pl,mass_ratio);
68
69 % Calculation , for the vector of propellant mass, of the fuel for the
70   transfer (m_fuel) and the total fuel of the 3 orbital actions (m_total):
71 [m_fuel_vec,m_total_vec]=fuel_mass_computation(m_p_vec,m_dry,m_pl,
72   mass_ratio);

73 %% PLOTS
74
75 figure
76 plot(r_LEO_vec/1000,Delta_V_Hohmann_vec)
77 xlabel('LEO parking orbit height $h_{LEO}';\left(\mathrm{km}\right)$');
78 ylabel('Impulse $\Delta V_{HT}';\left(\mathrm{m}/\mathrm{s}\right)$')
79 % xline(m_p_max,'--');
80 grid on
81 grid minor
82 box on

83 figure
84 plot(r_LEO_vec/1000,mass_ratio_vec)
85 xlabel('LEO parking orbit height $h_{LEO}';\left(\mathrm{km}\right)$');
86 ylabel('Mass ratio $\Delta m/m_0$')
87 % xline(m_p_max,'--');
88 grid on
89 grid minor
90 box on

91 figure
92 plot(r_LEO_vec/1000,delta_t_trans_vec)
93 xlabel('LEO parking orbit height $h_{LEO}';\left(\mathrm{km}\right)$');
94 ylabel('Transfer time $\Delta t';\left(\mathrm{days}\right)$')
95 % xline(m_p_max,'--');
96 grid on
97 grid minor
98 box on

99 figure
100 plot(m_p_vec,m_fuel_vec)
101 xlabel('Propellant mass loaded $m_p';\left(\mathrm{kg}\right)$'); ylabel('
102   Hohmann transfer fuel budget $\Delta m_{HT}';\left(\mathrm{kg}\right)$')

```

```

98 xline(m_p_max, '|');
99 text(m_p_max,450,'$m_{p,;max}$','HorizontalAlignment','right','FontSize'
100 ,12)
100 xlabel('m_p_max');
101 xline(1.22*delta_m_min, '|');
101 text(1.22*delta_m_min,450,'$m_{p,;min}$','FontSize',12)
102 grid on
103 grid minor
104 box on

```

Hohmann Transfer performance function

The following function computes Hohmann Transfer performance for a chosen LEO height.

```

1 function [Delta_V_Hohmann,delta_t_trans,mass_ratio,r_0,alpha,a_trans,
2 e_trans]=Hohmann_performance(R_E,r_LEO,Orbital_radius,mu,mu_earth,I_sp,g
3 )
4 % Function that computes the HT performance for a chosen LEO height
5
6 r_0 = R_E+r_LEO; % Radius of the parking orbit [m]
7 alpha = Orbital_radius./r_0; % Radii ratio
8
9 % Semiaxis major transfer orbit [m]
10 a_trans = (Orbital_radius + r_0)./2;
11
12 % Excentricity transfer orbit [m]
13 e_trans = abs((r_0-Orbital_radius)./(r_0+Orbital_radius));
14
15 % Velocities [m/s]
16 V_LEO = sqrt(mu_earth./r_LEO);
17 V_earth = sqrt(mu./R_E);
18 V_0=V_earth+V_LEO;
19
20 % Total HT impulse required [m/s]
21 Delta_V_Hohmann = V_0.* ( abs(sqrt(2.*alpha./(alpha+1))-1) + ...
22 abs(sqrt(1./alpha)-sqrt(2./alpha-2./(1+alpha)))); 
23
24 % Transfer time [days]
25 delta_t_trans = pi * sqrt(a_trans.^3./mu)/3600/24;
26
27 % Mass variation ratio
28 mass_ratio = 1 - exp(-(Delta_V_Hohmann)./(I_sp * g));
29 end

```

Fuel mass computation function

Function that determines, for a chosen propellant mass, the fuel required for the HT (m_{fuel}) and the corresponding total fuel budget (m_{total}).

```

1 function [m_fuel,m_total]=fuel_mass_computation(m_p,m_dry,m_pl,mass_ratio)
2 % Function that computes, for the chosen propellant mass, the fuel required
3 % for the HT (m_fuel) and the total fuel (m_total) of the 3 orbital
4 % actions of transfer, attitude control and reserve fuel tasks
5
6 m_fregat=m_p+m_dry; % Mass of the Fregat upper stage
7 m_0=m_fregat+m_pl; % Initial mass at the HT's periapsis
8 m_fuel=mass_ratio.*m_0; % Fuel mass for the HT

```

```
7 m_att=0.07*m_fuel; % Mass of fuel required to perform attitude control  
8    maneuvers  
9 m_margin=0.15*m_fuel; % Mass of fuel for margin purposes  
10 m_total=m_fuel+m_att+m_margin; % Total fuel mass  
11 end
```

Appendix 3: Lagrange points

The following MATLAB code represents the equipotential surfaces of Sun-Earth two body problem.

```

1 %% Equipotential surfaces and Langrange points plot
2
3 % Clear Command Window, clear workspace variables and close any MATLAB
4 % windows
5 clc;
6 clear;
7 close all;
8
9 % Reference frame parameters
10 mu = 0.1; % Ratio between Earth's mass and total mass (set 0.1 to zoom out)
11 xi = linspace(-1.5,1.5,100); % Adimentional 'x' variable
12 eta = linspace(-2,2,100); % Adimentional 'y' variable
13 [xi ,ETA] = meshgrid(xi ,eta); % Create 2D mesh
14
15 % Adimentional gravitational potential energy
16 f=@(xi ,eta) -(1-mu)./(sqrt((xi+mu).^2+eta.^2)) - (mu)./(sqrt((xi-(1-mu)
17 .^2)+eta.^2) ...
18 - 0.5*(xi.^2+eta.^2));
19 Z=f(xi ,ETA);
20
21 % Plot gravitational equipotential energy
22 set(groot , 'defaultAxesTickLabelInterpreter','latex');
23 set(groot , 'defaultTextInterpreter','latex');
24 set(groot , 'defaultLegendInterpreter','latex');
25
26 % 2D plot
27 figure(1);
28 hold on;
29 box on;
30 colormap(jet);
31 contour(xi ,ETA,Z,700);
32 colorbar;
33 title(cbar,{ '$u$' },'interpreter','latex');
34 title(' \textbf{Gravitational equipotential surfaces} ');
35 xlabel(' $\\xi $ ');
36 ylabel(' $\\eta $ ');
37 scatter(0,0,'filled','MarkerFaceColor',[0 1 0]);
38 scatter(0.9,0,50,'filled','MarkerFaceColor',[0 1 1]);
39 txt1 = {'L1'};
40 scatter(-0.1,0,200,'filled','MarkerFaceColor',[1 1 0]);
41 txt2 = {'L2'};
42 scatter(1.22,-0.02,txt2);
43 scatter(0,0,'filled','MarkerFaceColor',[1 1 0]);
44 txt1 = {'L3'};
45 scatter(-1.22,-0.02,txt1);
46 scatter(0,0,'filled','MarkerFaceColor',[0 1 0]);
47 txt4 = {'L4'};
48 scatter(0.4,0.9,txt4);
49 scatter(0,0,'filled','MarkerFaceColor',[0 1 0]);
50 txt4 = {'L5'};
51 scatter(0.4,-0.9,txt4);
52 scatter(0,0,'filled','MarkerFaceColor',[0 1 0]);
53 hold off;

```

```
54
55 % 3D plot
56 figure(2)
57 box on;
58 contour3(xi,ETA,Z,700);
59 colormap(jet);
60 colorbar;
61 cbar=colorbar;
62 title(cbar,{ '$u$' },'interpreter','latex');
63 title(' \textbf{3D plot of gravitational potential} ');
64 xlabel('$\xi$');
65 ylabel('$\eta$');
66 zlabel('$u$');
67 hold off;
```